Sorption Studies of Synthetically Modified Carbon Nanomaterials

A Thesis Submitted to the College of
Graduate Studies and Research
In Partial Fulfillment of the Requirements
For the Degree of Doctor of Philosophy
In the Department of Chemistry
University of Saskatchewan
Saskatoon

By

Jae Hyuck Kwon

PERMISSION TO USE

In presenting this thesis in partial fulfilment of the requirements for a Postgraduate degree from the University of Saskatchewan, I agree that the Libraries of this University may make it freely available for inspection. I further agree that permission for copying of this thesis in any manner, in whole or in part, for scholarly purposes may be granted by the professor or professors who supervised my thesis work or, in their absence, by the Head of the Department or the Dean of the College in which my thesis work was done. It is understood that any copying or publication or use of this thesis or parts thereof for financial gain shall not be allowed without my written permission. It is also understood that due recognition shall be given to me and to the University of Saskatchewan in any scholarly use which may be made of any material in my thesis.

Requests for permission to copy or to make other use of material in this thesis in whole or part should be addressed to:

Head of the Department of Chemistry
University of Saskatchewan
Saskatoon, Saskatchewan, S7N 5C9

DEDICATION

I would like to dedicate this dissertation and its all related honour to my wife, Gloria. Without her patience and perseverance, I cannot achieve this goal.

ABSTRACT

The major contributions from this research were 1) the finding of the multi-purpose adsorbent (goethite/activated carbon composite) for removing of inorganic oxyanions and organic aryl arsenical species in aqueous solution, 2) the development of an *in-situ* filtration device, and 3) attenuation of Fe leaching by using composite materials below ambient room temperature.

The theme of this research was focused on developing insoluble adsorptive materials for the phase removal of inorganic selenium and organic arsenic species in aqueous solutions. Many technical methods have been reported to manage toxic chemical species including reverse-osmosis, ion exchange, zero-valent iron reduction, and microbial treatment have been utilized in water treatment processes. However, these methods are less attractive than adsorption-based methods that employ iron oxide as an adsorbent in terms of the versatile nature and suitable physicochemical properties of such materials.

To achieve the effective sorptive removal of selenite and aryl arsenic species in aqueous solution, magnetite composites with activated carbon were prepared as described in Chapter 2. The porosity and the oleophilicity of activated carbon contribute to the unique structural features and the chemical affinity of magnetite toward oxyanion and cation species which may cooperatively enhance their adsorption properties. Magnetite and its composites were prepared using a Fe^{2+}/Fe^{3+} co-precipitation method at 60 °C under anaerobic conditions. As a comparative mineral oxide adsorbent material, iron oxyhydroxide (goethite, α-FeOOH) was synthesized at high molar ratios of OH^{-}/Fe^{3+} (5/1). The magnetite composites and goethite were prepared in good yield (97-98%) and characterized by various materials characterization methods; powder X-ray Diffraction (PXRD), Raman spectroscopy, and Diffuse Reflectance Infrared Fourier Transform Spectroscopy (DRIFTS). Thermogravimetric analysis (TGA), Scanning Electron Microscopy (SEM), Transmission Electron Microscopy (TEM), and N_2 adsorption-desorption were used to further characterize the structure and physicochemical properties.

Chapter 3 details an investigation of the adsorptive properties of magnetite composites, activated carbon, and respective mineral oxides with a selenite anion species (Se(IV)) in aqueous solution. Sorption kinetics and isotherms for the uptake of inorganic selenium was determined with Hydride Generation Atomic Absorption Spectroscopy (HGAAS, detection limit

0.2 ppb for absorbance units and 0.03 ppb for absorbance peak intensity) with various adsorbent materials (i.e. synthetic magnetite (Mag-P), commercial magnetite (Mag-C), synthetic magnetite/ activated carbon composite with 19% magnetite (CM-19), and goethite were measured at pH 5.26 in aqueous phthalate buffer solution at various temperatures. The sorptive uptake at equilibrium and at various kinetic conditions for the various sorbent materials showed the following uptake in descending order: goethite (138 μg/g) > Mag-P (55.5 μg/g) > Mag-C (48.3 μg/g) > CM-19(19.2 μg/g) > NORIT ROX 0.8 (activated carbon (AC); 11.9 μg/g). Mag-P showed an "apparent" negative E_a (~-6.96 to -7.16 kJ/mol) and $\Delta H^{\ddagger}$ (-9.47 kJ/mol) kinetic parameters. In contrast, Mag-C, CM-19, and goethite showed a positive E_a and $\Delta H^{\ddagger}$ kinetic parameters. The entropy change of activation ($\Delta S^{\ddagger}$) for NORIT ROX 0.8 was positive value and suggested that bond breakage occurred during the transition state of unbound adsorbate to bound adsorbate species. Because the design of the magnetite composite was based on an iron oxide nanomaterial, the occurrence of Fe leaching was studied. In the case of composite materials, Fe leaching was attenuated relative to iron oxide materials because of the presence of magnetite particles within the pores and on the surface of the activated carbon, was observed at conditions below room temperature.

In Chapter 4, the adsorptive properties of magnetite composites were studied with an organic form of arsenic (i.e. roxarsone; 4-hydroxy-3-nitrobenzenearsonic acid) in aqueous solutions at pH 7.00 in aqueous phosphate buffer at 21 °C using UV-vis spectrophotometry (detection limit of roxarsone: 3.66×10^{-6} M). The sorption kinetics and equilibrium uptake properties of the composite materials and their respective components were evaluated for the uptake of arsenic (V) species of roxarsone. The following sorbent materials were evaluated with Mag-P, Mag-C, CM-10, CM-19, CM-32, and goethite. NORIT ROX 0.8 showed the highest removal uptake for roxarsone at equilibrium. The relative uptake of roxarsone for each sorbent material was listed in descending order: granular activated carbon (GAC: 471 mg/g) > goethite (418 mg/g) > CM-19 (254 mg/g) > CM-32 (227 mg/g) > Mag-P (132 mg/g) > Mag-C (29.5 mg/g). Based on thermodynamic and kinetic sorption parameters, roxarsone species were adsorbed on the surface of the iron oxide/oxyhydrate as inner-sphere surface complexes of monodentate-mononuclear, bidentate-mononuclear, and bidentate-binuclear depending on the type of ionic speciation of roxarsone. However, the dominant uptake of roxarsone in the case of GAC and its composites likely occurs via the phenyl ring on the graphene surface of the sorbent materials; whereas secondary binding occurs via the arsenate anion with the exception of goethite.

Based on the results presented, magnetite composites and goethite may be used as potential sorbent materials for the removal of organic and inorganic species because of their variable sorption affinity and capacity. Composite materials as described herein are anticipated to display dual sorption behavior because of tunable Lewis acid (such as iron species) - base (such as heteroatoms (O) of various functional groups and the lipophilic contributions from AC) sites, which offering tunable surface chemistry for selected adsorbates.

ACKNOWLEDGMENTS

Glory to Jesus!

Upon completing my program, I thank first Professor Dr. Lee. D. Wilson. He is my supervisor and friend. His attitude looking life and managing problems both in academic world and in the real world always encourages and inspires me. I thank Dr. R. Sammynaiken who is the managing director of Saskatchewan Structural Science Centre. He was also my co-supervisor during the initial stages of this study. His idea to re-start my project was very timely and he helped me characterize the prepared materials. I thank my Advisory Committee members, Dr. Matthew Paige, Dr. Stephen Foley, and Dr. Catherine H. Niu. Their kind and deep knowledge on my research projects made me strong and persevering for finishing this study.

I have enjoyed my life in research with my colleagues. The great team of Professor Dr. Wilson has taken burdens together, has coached mutually, and has condoled ourselves whenever we have faced difficulties arising from our lives and research.

I thank the Department of Chemistry for funding my research.

Finally yet importantly, I thank my family for their sincere prayer and support for my study.

Thank Jesus! You made me achieve this wonderful work.

TABLE OF CONTENTS

LIST OF TABLES

LIST OF FIGURES

LIST OF SCHEMES

LIST OF ABBREVIATIONS

A (Absorbance)

Activated carbon (AC)

American Society for Testing and Materials (ASTM)

Body-centered-cubic (*bcc*)

Brunauer-Emmett-Teller (BET)

Charge Distribution (CD)

Chemical Abstract Service (CAS)

Commercial magnetite (Mag-C)

Constant capacitance model (CCM)

Crystal field stabilization energy (CFSE)

Cubic close packed (*ccp*)

Degree of freedom (DoF)

Diffuse double-layer model (DLM)

Diffuse Reflectance Infrared Fourier Transform Spectroscopy (DRIFTS)

Drinking water quality guideline (DWQG)

Face-centered cubic (*fcc*)

Granular Activated Carbon (GAC)

Hexagonal close packed (*hcp*)

High-spin (HS)

Higher relative standard deviation (HRSD)

Highest Occupied Molecular Orbital (HOMO)

Hybrid fractional error function (HYBRID)

Iron-oxide-coated sand (IGCS)

Inner Helmholtz plane (IHP)

Layered Double Hydroxides (LDH)

Linear free energy relationship (LFER)

Low-spin (LS)

Lower relative standard deviation (LRSD)

Lowest Unoccupied Molecular Orbital (LUMO)

Marquardt's percent standard deviation (MPSD)

Melting point (m.p.)
Metal Mining Effluent Regulations (MMER)
Methylene blue (MB)
MUlti SIte Complexation (MUSIC)
o-phenanthroline (OP)
Oct (Octahedral)
One-dimension (1D)
Outer Helmholtz plane (OHP)
p-nitrophenol (PNP)
Pore width (pw)
Powder X-ray Diffraction (PXRD)
Pseudo-First Order (PFO)
Pseudo-Second Order (PSO)
PZC (Point of zero charge)
Recommended dietary allowance (RDA)
Relative standard deviation (RSD)
Root mean square error (RMSE)
Scanning Electron Microscopy (SEM)
Squares of the errors (ERRSQ)
Standard deviation (SD)
Sum squares of errors (SEE)
Surface complexation model (SCM)
Synthetic magnetite (Mag-P)
Synthetic magnetite/activated carbon composite (CM)
Tetr (Tetrahedral)
Thermogravimetric analysis (TGA)
Three-dimensional (3D)
Transmission Electron Microscopy (TEM)
Triple-layer model (TLM)
Two-dimensional (2D)
Union of Pure and Applied Chemistry (IUPAC)

Upper intake levels (ULs)

World Health Organization (WHO)

CHAPTER 1 INTRODUCTION

1.1 Background of research and research objectives

The level of risk originating from toxic metals in the environment and ecological systems is continuously escalating as our imprudent development of food, forests, soil, air and water resources. Selenium is usually known as the "double-edged sword element" for its dual toxicity (>400 µg / day) and its valuable nature as a micronutrient (<40 µg / day).[1] In aquatic environments, selenium species accumulate in the tissue of organisms and can cause birth defects in fish and aquatic birds.[2] Also, it can cause selenosis (the “blind staggers”) in animals and other mammals that consume high levels of selenium in their forage.[2] Adverse effects of selenium in the environment and human health have been reported. For example, high Se levels were reported in a lead mine operated by Teck in the Elk Valley region of BC, Canada[3] and in various coal mines in Kentucky and in West Virginia, USA.[4] Se drinking water quality guidelines (DWQG) have been established at levels below 10 ppb in Canada and below 50 ppb in the USA, respectively.[5] Therefore, there is need to remove selenium in wastewaters and in drinking water supplies depending on the nature of the source water quality or the type of industrial activity.

Arsenic, like selenium, has a negative effect on human health which is referred to as "arsenicosis" as it accumulates in the body through dietary pathways. With regard to adults, the acute minimal lethal dose of arsenic is about 1 mg/kg per day.[6] Arsenic contamination in drinking water has been highlighted because of its toxicity.[7] Many countries such as Bangladesh, New Zealand, United States, Italy, and Malaysia are facing issues related to elevated levels of arsenic in drinking water.[8] Therefore, an international drinking water quality guideline (DWQG) was established for As at 200 parts per billion (ppb, µg/L). The DWQG has since been changed to 50 ppb, and more recently, the DWQG was reduced to 10 ppb after consideration of the harmful health risks associated with arsenic exposure.[8]

Roxarsone (4-hydroxy-3-nitrobenzenearsonic acid) and arsanilic acid (4-aminophenylarsonic acid) are arylarsenicals which are used as food additives to promote the weight gain of swine and poultry and to control diseases. Roxarsone can contaminate the soil and water through the use of poultry litter as a source of fertilizer[9] which may be subsequently washed into ground water supplies.[10] Thereafter, this compound can be subsequently degraded and converted into more toxic inorganic forms of arsenic (arsenite and arsenate) in the environment.[11-14] Therefore, there is a need to address the minimize the occurrence and potential risk of roxarsone-contaminated wastewater and soils through the development of suitable adsorbent materials.

Since the Metal Mining Effluent Regulations (MMER)[15] came into force in 2002 and have been implemented with about 100 facilities across Canada by 2010, all mining industries are required to meet release limits on releases of arsenic, copper, cyanide, lead, nickel, zinc, radium-226, and total suspended solids. As an example, metals such as As, Mo, Ni and Se are reported to be present in the aqueous and solid phases of uranium mine tailings in northern Saskatchewan.[16]

Arsenic and selenium species were of significant interest in my research because they represent a group of major harmful elements/chemicals in the environment that might exist in various oxidation states and protolytic forms. As well, roxarsone and selenite are representative model compounds and their deleterious health effects toward humans, fish, and aquatic birds were well documented.[2,7]

The removal of selenium from aqueous environments are categorized into three groups: physical (e.g., reverse osmosis, nanofiltration, ion exchange, and evaporation), chemical (e.g., iron reduction and precipitation, ferric coagulation and filtration, cementation, electrocoagulation, and photoreduction), and biological (volatilization, active microbial reduction, passive microbial reduction, *in-situ* microbial reduction, and wetlands bioremediation) processes.[17] Arsenic removal was evaluated by various technologies: sedimentation, precipitation/co-precipitation, adsorption, ion exchange, membrane separation (microfiltration, reverse osmosis, electrodialysis, ultrafiltration, and nanofiltration), and biological methods.[8] Among the various methods, adsorption is considered to be more suitable in terms of its operating cost, safety, and versatility compared with either chemical or biological methods because of their greater technological complexity.[8]

For removal of metal cations and oxyanions from wastewater, iron oxides (e.g., magnetite, Fe_3O_4; maghemite, γ-Fe_2O_3; hematite, α-Fe_2O_3), iron oxyhydroxides (e.g., goethite, α-FeOOH), aluminum oxides (e.g., activated alumina, γ-Al_2O_3), and aluminum oxyhydroxides (e.g., gibbsite, $Al(OH)_3$) have been applied for decades. This is attributed to the high affinity of such metal oxides for selenite species because of the presence of Lewis acid or Lewis base sites that contribute to formation of stable surface complexes.[18]

1.2 Research hypothesis

The development of surface modified carbon nano-materials with tunable properties was motivated by considering how toxic metal species such as selenium and arsenic can be effectively removed from aquatic environments such as mineral tailing ponds at mine sites. The following hypothesis is related to adsorptive properties of synthetic materials and the molecular level details of aspects of the adsorptive processes are presented below.

Oxyanion (adsorbate) can be a Lewis base and magnetite (adsorbent) can be a Lewis acid to form a surface complex on the surface of magnetite. There will be additional chemical interactions between adsorbent metals and adsorbate ligand such as π-π interaction and H-bonding.

1.3 Literature Review

1.3.1 Selenium Chemistry

$^{80}_{34}$Se (melting point (m.p.): 271 °C, boiling point: 685 °C, and density near room temperature: 4.26 - 4.79 g/cm^3) is found in the group VIA (O, S, Se, Te, Po) of the periodic table. As one of the non-metals (C, P, S, Se, O, N, halogen and noble gases), selenium (Se) was discovered by Swedish chemists J. J. Berzelius and J. G. Gahn.[19,20] Its name originated from the Greek word *selene***,** for moon, since its chemical similarity resembles that of tellurium.[20] The morphology of selenium has different allotropic forms such as amorphous, crystalline, and metallic.[20] The amorphous form is colored in a dark-red to black powder, where it becomes softer at 50-60 °C, and turns into an elastic form at 70 °C.[20] The crystalline and dark-red transparent form shows a sharp melting point (m.p. 144 °C), while the red crystals are unstable and will be transformed to the more stable gray form as heat is applied.[20] Selenium in the gray metallic form becomes visible as gray to black lustrous hexagonal crystals which melt at 217 °C and conducts electricity up to one thousand times more when it is exposed to light.[20] Thus, there are many industrial uses of metallic selenium which are attributed to its unique electronic and photoelectric properties. Therefore, Se is considered a metalloid due to its dual properties of metal (e.g., semi-conductor) and nonmetal (e.g., dull and gray elemental Se).

None of the naturally existing isotopes of selenium (^{80}Se (49.8 %), ^{78}Se (23.5 %), ^{76}Se (9.02 %), ^{82}Se (9.19 %), ^{77}Se (7.58 %), and ^{74}Se (0.87 %)) are not radioactive.[20] However, a by-product of the nuclear reactor and neutron activation technology, ^{75}selenium, is one of the more useful radionuclides for broad using as a biological tracer experiments and diagnostic procedures because it has a convenient gamma-ray emission for counting and its half-lives (120 days) is sufficient enough to permit complete chemical separation from other chemical activities.[20]Selenium has several oxidation states: selenide (Se^{2-}), selenium (Se^0), Se^{2+} (not yet found in nature), selenite (Se^{4+}), and selenate (Se^{6+}). Selenides (Se^{2-}) are present as hydrogen selenide (H_2Se: aqueous and gaseous states), metal selenides (Na_2Se, CdSe, In_2Se_3, GaSe, HgSe, etc), and a number of organic selenides (carbon diselenide: CSe_2, diphenylselenide: $C_{12}H_{10}Se$, dimethyl selenide: $(CH_3)_2Se$, etc). Elemental selenium (Se^0) is insoluble and stable against oxidation-reduction (redox) reaction and therefore considered relatively non-toxic in aqueous environments. With air oxidation, Se^0 is oxidized to selenium dioxide (SeO_2), which sublimes readily. In addition, the weak selenous acid (H_2SeO_3) is formed by its reaction with water. Selenite (Se^{4+}) is highly toxic in solution and more reactive than selenates (Se^{6+}) due to its polarity and basicity and less soluble than selenates. Under acidic conditions, selenites are often reduced to elemental selenium (Se^0) by a mild reducing agent such as ascorbic acid or SO_2. The molecular structures of selenous and selenic acids are shown in Fig. 1.1.

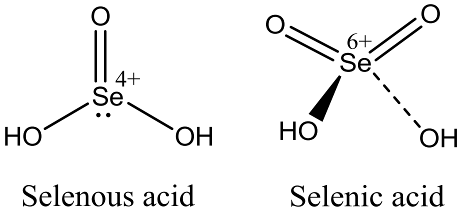

Figure 1.1 The molecular structures of selenous and selenic acid. The dashed line represents a bond that extends away from the viewer and the wedge-shaped line represents a bond oriented toward the viewer.

Selenites have a known high affinity for iron and aluminum sesquioxides (Fe_2O_3 and Al_2O_3), whereas selenates do not form stable sesquioxides. Thus, selenates found in soils are simply taken apart and are readily bioavailable to plants. Basic and oxidative conditions favor the formation and stability of selenates (Se^{6+}). Most selenates are very soluble and selenic acid (H_2SeO_4) is a strong acid ($K_a = 1000$). The acid-base equilibrium constants for selenium at 25 °C and 1 bar pressure are listed in Table 1.1.[21] Selenate is also apt to be reduced to selenite under acidic conditions; about 60 % of selenate was converted to selenite during a 7 day storage period in 4 M HCl solution.[22]

Table 1.1 Acid-base equilibrium constants for selenium at 25 °C and 1 bar pressure in water

Species	pK_a
$H_2SeO_3 \rightleftharpoons HSeO_3^- + H^+$	2.63
$HSeO_3^- \rightleftharpoons SeO_3^{2-} + H^+$	8.40
$H_2SeO_4 \rightleftharpoons HSeO_4^- + H^+$	-3.00
$HSeO_4^- \rightleftharpoons SeO_4^{2-} + H^+$	1.70

The speciation and fraction of selenium by pH in aqueous solution is shown in Fig. 1.2.[21]

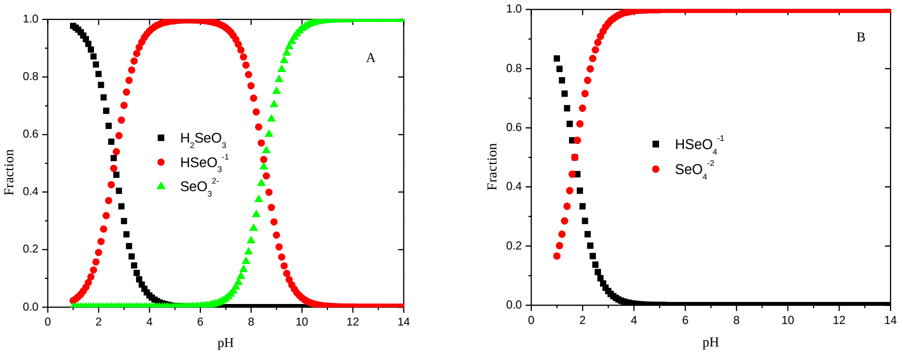

Figure 1.2 Selenium speciation and mole fraction versus pH in the solution for selenous acid (A) and selenic acid (B)

1.3.2 Arsenic Chemistry

Arsenic occurs naturally in surface water such as rivers, lakes, reservoirs, and ponds by the natural processes of soil erosion, mineral leaching, volcanic deposits, and weathering[23] and anthropogenic atmospheric inputs such as smelting operations, fossil-fuel combustion, and human activities largely contribute to the overall arsenic cycle.[24] Arsenic has four different oxidation states (3-, 0, 3+, and 5+) in the environment; however the distribution of arsenic species in natural waters depends on the redox potential and pH conditions.[25] The dominant forms of arsenic are the oxyanions of arsenite (As^{3+}) or arsenate (As^{5+}).[25] In surface waters, the more oxidized form of arsenate is the most thermodynamically stable, whereas the reduced form of arsenic (As(III)) prevails in mildly reducing conditions such as in closed ground waters is favoured thermodynamically.[25] In most natural waters, arsenic (III) is present in its non-ionized form of arsenous acid (H_3AsO_3, pK_a = 9.22) and may react in a limited fashion with most mineral surfaces.[26] Therefore it is more challenging to isolate arsenic(III) by the traditional treatment methods such as adsorption, precipitation, etc.[26] Roxarsone (4-hydroxy-3-nitrobenzenearsonic acid) and arsanilic acid (4-aminophenylarsonic acid) are shown in Fig. 1.3. These types of arylarsenicals are used as feed additives to promote the weight gain of swine and poultry, and to control microbial-based diseases. Roxarsone may contaminate soil and water sources using poultry litter as fertilizer[27] which can subsequently leach into ground and subsurface water supplies.[28] Thereafter, this compound may undergo subsequent degradation and be converted into more toxic inorganic forms of arsenic (arsenite and arsenate) in the environment.[29-32]

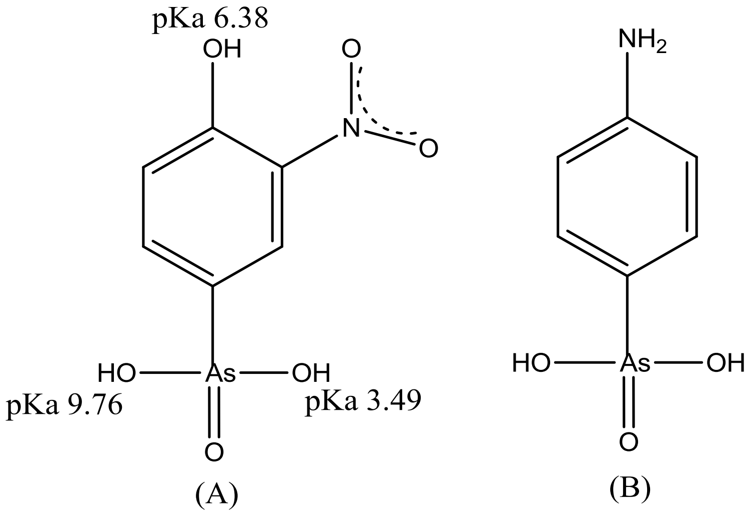

Figure 1.3 Molecular structures of roxarsone (A) with its pK_a values and arsanilic acid (B)

The protolytic speciation of arsenite and of arsenate species and equilibrium constants are shown in Table 1.2.[33] This data is of interest to understand the form of species under consideration for the studies described herein (*vide infra*) and in various literature reports.

Table 1.2 Acid-base equilibrium constants for arsenite and for arsenate in water

Arsenite	pK_a	**Arsenate**	pK_a
$H_3AsO_3 \rightleftharpoons H_2AsO_3^- + H^+$	9.23	$H_3AsO_4 \rightleftharpoons H_2AsO_4^- + H^+$	2.22
$H_2AsO_3^- \rightleftharpoons HAsO_3^{2-} + H^+$	12.1	$H_2AsO_4^- \rightleftharpoons HAsO_4^{2-} + H^+$	6.98
$HAsO_3^{2-} \rightleftharpoons AsO_3^{3-} + H^+$	12.7	$HAsO_4^{2-} \rightleftharpoons AsO_4^{3-} + H^+$	11.53

The speciation and fraction of arsenite and of arsenate forms against pH vary in aqueous solution as shown in Fig. 1.4. The molecular structures of arsenous and arsenic acids are illustrated in Fig. 1.5.

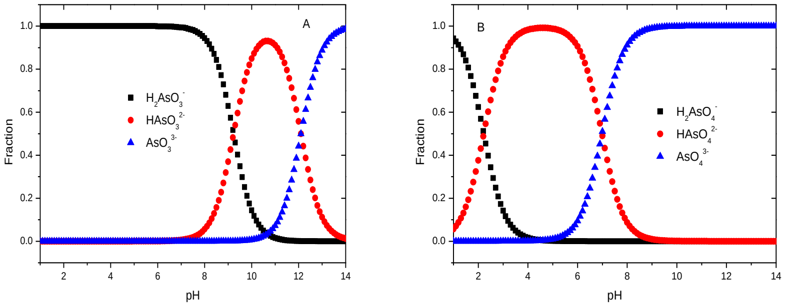

Figure 1.4 Arsenic speciation and mole fraction versus pH in the solution for arsenous acid (A) and arsenic acid (B)

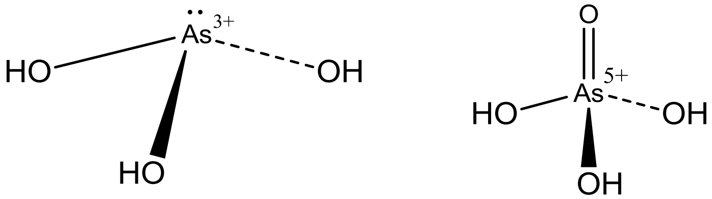

Arsenous acid

Arsenic acid

Figure 1.5 The molecular structures of arsenous and arsenic acid

1.3.3 Iron Chemistry

1.3.3.1 Introduction

Iron ($^{56}_{26}$Fe) is the sixth most abundant element on the earth. Pure elemental iron (electronic configuration: [Ar]$3d^6 4s^2$, melting point: 1808 K, boiling point: 3023 K) is a silvery-white, soft metal that rusts rapidly in humid oxygenated air. Since the pure elemental form of iron is of little use, it is sometimes fortified by the addition of small amounts of carbon and other transition metals to improve its physical and chemical properties. The most common usage of elemental iron include the fabrication of steel and its alloys such as alloy steels and carbon steels containing 0.1 - 0.5% carbon content. The latter contains other metals along with carbon for different applications: vanadium for springiness, chromium for improving hardness and corrosion properties, manganese for resistance to wear, nickel for improving toughness in armor plating, molybdenum and tungsten for heat resistance, and stainless steels for corrosion containing ~18 % chromium and ~8 % nickel.[34]

Rusting of iron is caused by the formation of a hydrated oxide $Fe(OH)_3$ or FeO(OH), resulting from an electrochemical reaction of iron with water, oxygen, and an accompanying electrolyte. Without one of these necessities, rust formation cannot occur.

Iron may be pyrophobic when it is reduced to a very fine metal powder. The well-known property of elemental iron is its magnetic susceptibility. Soft iron and carbon steels are easily magnetized, however this magnetism is also easily altered or inverted to a property which makes it important as a core material in electric transformers and motors.[35] Other materials such as cobalt steels are difficult to magnetize, however; such materials retain their magnetic properties which make them valuable materials as permanent magnets.

Iron consists of two different unit cells and types of magnetism are shown in Scheme 1.1. Fe is ferromagnetic up to its Curie temperature of 1041 K, where it becomes merely paramagnetic. The body-centered-cubic (*bcc*) lattice of iron is changed to a cubic close packed (*ccp*) at 1183 K and then returns to the bcc above 1663 K.[36]

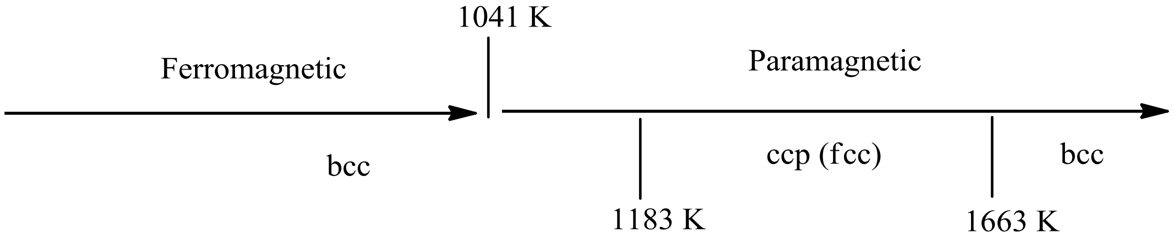

Scheme 1.1 Magnetism and unit cell characteristics of iron at various temperatures

The outer electronic configuration of iron with the zero valent state is $4s^2 3d^6$. Depending on the oxidation state and the nature of the surrounding ligands, iron can have various unpaired electrons from 0 to 5. The oxidation state identified for iron compounds array from -II (d^{10}) to +VIII (d^0) with examples shown in Table 1.3.[37] Among them, Fe (II, d^6), Fe (III, d^5), and Fe (IV, d^4) compounds have more than one coordination number: Fe (II, d^6) for 5, 6, and 8, Fe (III, d^5) for 4, 5, 6, 7, and 8, and Fe (IV, d^4) for 6.[38]

Table 1.3 Oxidation states and coordination chemistry of iron compounds

Oxidation state	Coordination number	Geometry	Example	Literature Reference
Fe (-II), d^{10}	4	Tetrahedral	$[Fe(CO)_4]^{2-}$	39
Fe (-I), d^9	-	5-coordinate (including Fe-Fe bond)	$[Fe_2(CO)_8{}^{2-}]$	40
Fe (0), d^8	5	Trigonal bipyramidal	$[Fe(CO)_5]$	41
Fe (I), d^7	6	Octahedral	$[Fe(H_2O)_5NO]^{2+}$	42
Fe (II), d^6	4	Tetrahedral	$[FeCl_4]^{2-}$	43
Fe (III), d^5	3	Trigonal	$[Fe(N(SiMe_3)_2)_3]$	44
Fe (IV), d^4	4	Tetrahedral	$[Fe(I\text{-}norbornyl)_4]$	45
Fe (V), d^3	4	Tetrahedral	$FeO_4{}^{3-}$ (only in solid oxide materials)	46
Fe (VI), d^2	4	Tetrahedral	$FeO_4{}^{2-}$	47
Fe (VIII), d^0	-	Not established	Fe at high pH or alkaline media	48

1.3.3.2 Iron Oxide

Iron oxides including oxide-hydroxides and hydroxides composed of Fe and O and/or OH are referred to as iron oxides. Sixteen different iron oxides are shown in Table 1.4[49]. But most compounds, iron are present as trivalent Fe(III) species, but FeO, $Fe(OH)_2$, and Fe_3O_4 contain Fe(II) species. The crystal structure of iron oxide is packed with the closed arrays of anions usually in hexagonal close packed (*hcp*) or cubic close packed (*ccp*), where the interstices are partially filled with Fe(II) or Fe(III) predominantly in octahedral (VI) - $Fe(O)_6$, or $FeO_3(OH)_3$ - but may possess tetrahedral (IV) - $Fe(O)_4$ – coordination in some cases.[50] Since the anions are much bigger than the cations (the ionic radii of O^{2-}, Fe(III), and Fe(II) are 0.14, 0.065, and 0.082

nm, respectively), the array of the anions modify the crystal structure and the ease of topological interconversion between different iron oxides.[51]

Table 1.4 The various forms of iron oxide materials

Oxides	**Oxide-hydroxides**	**Hydroxides**
Alpha phase, hematite (α-Fe_2O_3)	Goethite (α-FeOOH)	Iron(II) hydroxide ($Fe(OH)_2$)
Beta phase, (β-Fe_2O_3)	Akaganeite (β-FeOOH)	Iron(III) hydroxide ($Fe(OH)_3$, bernalite
Gamma phase, Maghemite (γ-Fe_2O_3)	Lepidocrocite (γ-FeOOH)	
Epsilon phase, (ε-Fe_2O_3)	Feroxyhyte (δ'-FeOOH)	
Iron(II,III) oxide, Magnetite (Fe_3O_4)	Ferrihydrite ($Fe_5HO_8 \cdot 4H_2O$)	
Iron(II) oxide, wüstite (FeO)	High-pressure FeOOH	
	Schwertmannite $Fe_{16}O_{16}(OH)_y(SO_4)_z \cdot nH_2O$ δ-FeOOH Green rusts $(Fe(III)_xFe(II)_y(OH)_{3x+2y-z}(A^-)_z$; $A^- = Cl^-$; 1/2 SO_4^{2-}	

Note: x, y, z and n are integer values

Most iron oxides are crystalline besides ferrihydrite and Schwertmannite, which are poorly crystalline and certain iron oxides are isomorphous with other metal oxides. For example, goethite (α-FeOOH) is isomorphous with diaspore (α-AlO(OH)) structured by hexagonal close packing (*hcp*) of anions. The structure of goethite consists of an *hcp* array of anions (O^{2-} and OH^-) stacked along the [010] direction with Fe^{3+} ions that occupy half the octahedral interstices within a layer possessing the building unit of an $FeO_3(OH)_3$ octahedron as the other iron oxide-hydroxide (α-, β-, γ-, δ-, and high pressure) forms may contain.

Magnetite and jacobsite (Fe(III)Mn(II)Fe(III)O_4) are isomorphous with an inverse spinel structure type.[52] Iron oxides are characterized by the crystallographic system and structural type as shown in Table 1.5. Their structural order and crystal size are different and depend entirely on their formation conditions. There are two essential ways to describe the structure of iron oxides: either by anion packing or by linkage of octahedral and/or tetrahedral units from a central atom and its nearest anion neighbors (ligand).

Table 1.5 Crystallographic system and structural type of iron oxides[52,53]

Iron oxides	**Crystallographic system**	**Structural type**
Goethite	Orthorhombic	Diaspore
Lepidocrocite	Orthorhombic	Boehmite
Akaganeite	Monoclinic	Hollandite
Schwertmannite	Tetragonal	Hollandite
Feroxyhyte	Hexagonal	-
δ-FeOOH	Hexagonal	-
High-pressure FeOOH	Orthorhombic	InOOH
Ferrihydrite	Hexagonal	-
Hematite	Hexagonal (Rhombohedral)	Corundum
Magnetite	Cubic	Inverse Spinel
Maghemite	Cubic or Tetragonal	Defect Spinel
Wüstite	Cubic	Defect NaCl
ε-Fe_2O_3	Orthorhombic	Defect NaCl
$Fe(OH)_2$	Hexagonal	Brucite
Bernalite	Orthorhombic	Corundum

The most typical arrangement of the sheets of anion arrays in the three dimension in iron oxides is an hexagonal close packing (*hcp*) of stacked sheets ABABAB..., and cubic close packing (*ccp*), where the ABCABCABC... stacking of the sheets occurs. The one exception of this structural arrangement is akaganeite (β-FeOOH), which has a body-centered cubic (*bcc*) anion arrangement.

There are twice as many interstices between the sheets of anions since the anions are in a layer.[52] The cations fit into the octahedral or in the smaller tetrahedral interstitial sites. For iron oxides containing Fe(III) ions, the charge balance effects ensure that only a section of interstitial sites can be filled, and open up the possibility of several different arrangements of cations between anion sheets. Therefore, structural differences between different iron oxide structures are possible as the consequence of variation in the arrangement of cations in the interstices, and to a lesser extent, the differences in the stacking of the sheets of anions. The anion sheets are bound by the cations and/or by hydrogen bonds in the case of hydroxides.

Fe(III) in iron oxides favors the high spin (unpaired *d*-electrons) state at all times. Since Fe(III) has no crystal field stabilization energy (CFSE), there is little preference for one or the other type of site, despite whether it is octahedral or tetrahedral coordinated. However, Fe(II) has higher CFSE for octahedral than for tetrahedral, it prefers to coordinate to the octahedral site.[53] The electronic configuration of Fe^{3+} species is [Ar]$3d^5$ and for the Fe^{2+} species is [Ar]$3d^6$. In the case of iron oxides, the cations are octahedral and/or tetrahedral coordinated toward negatively charged O^{2-}/OH^- ions and in the electrostatic field created from the proximity of these ligands, whereas; the Fe *d*-orbitals are not degenerate. Those *d*-electrons in orbitals directed along coordinate axes experience greater repulsions from the negative ligands than do those whose maximum density is concentrated between the axes. As a result of this, the five *d*-orbitals are split into two sets of different energies (t_{2g}: d_{xy}, d_{yz}, d_{zx}, and e_g: d_{z^2}, $d_{x^2-y^2}$). The t_{2g} set has a lower energy on an octahedral site, whereas for the tetrahedral site, the *e* set is the lower energy. The ways of *d*-electron filling into *d* orbitals are high-spin (HS) state and the low-spin (LS) state, as shown in Fig. 1.6.

Figure 1.6 The *d* orbital filling patterns for d^5 electron system

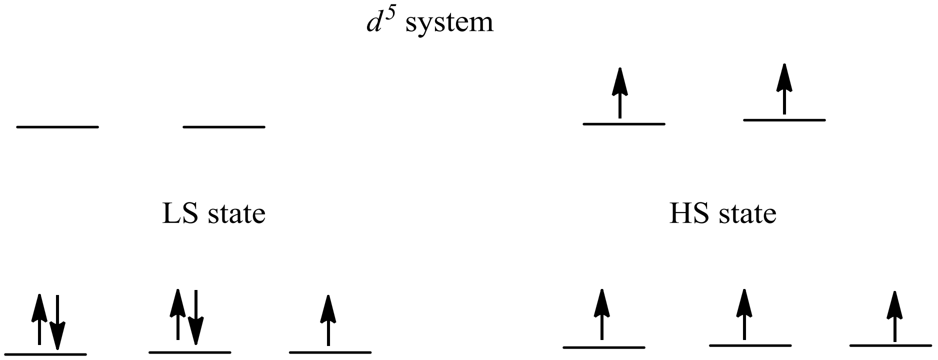

The HS state is achieved by an electron which occupies all *d*-orbitals first according to Hund's rule (one each in the orbital). However, the LS state is formed by entering two electrons being forced into a lower orbital to give a spin-paired state since the energy needed to place electrons in the higher set of orbitals is greater than the electronic repulsion energy which arises when electrons are paired (i.e. electrons first fill the lower energy level states). In crystal field theory, the point charge ligand affects the splitting pattern of the orbital energy as shown in Fig. 1.7.

Figure 1.7 The splitting of *d* orbitals which is octahedral coordinated by ligands

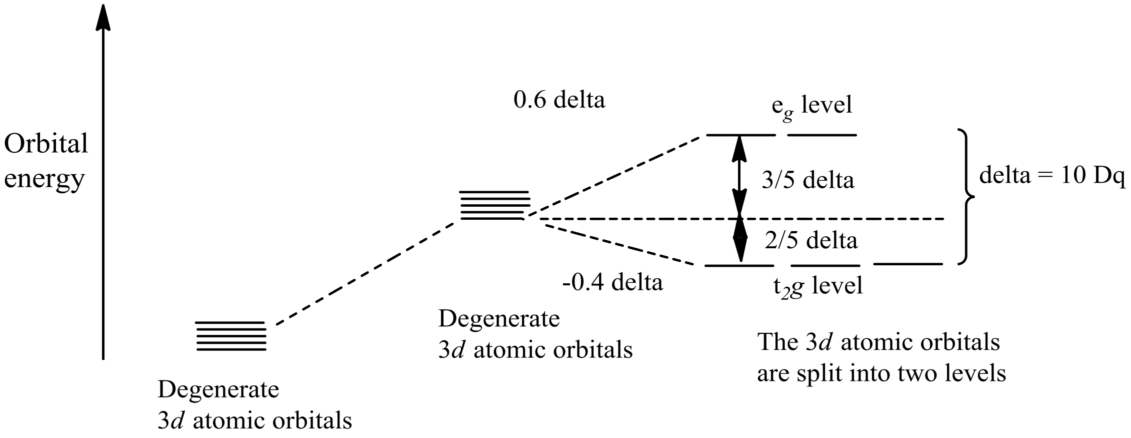

When a metal ion is coordinated by ligands, the spherical electrostatic field is created by the point charge ligands, and if the electrostatic field is octahedral, the energy of the electrons in the *d*-orbitals that point directly at the ligands are raised with respect to a spherical field. In contrast, the energy of the electrons in the orbitals that point between the ligands is lowered with respect to the spherical field.[54] In iron oxides, Fe^{3+} species exist in a high-spin state in both octahedral (O_h) and tetrahedral (T_d) coordination. The ground state configuration for O_h coordination is $(t_{2g})^3(e_g)^2$, the first three electrons enter the t_{2g} levels and the remaining electrons enter the e_g level. The ground state configuration of Fe^{3+} species for T_d coordination is $(e)^2$ $(t_2)^3$. The CFSE for O_h site is calculated using the following equation (1-1), *n* is the number of electrons in the individual *d*-orbital set.

$$CFSE = \Delta(-0.4\, n\,(t_{2g}) + 0.6\, n\,(e_g)) \qquad (1\text{-}1)$$

The absolute total net difference of CFSE between octahedral (O_h) and tetrahedral (T_d) coordination for Fe^{3+} is zero, but that of Fe^{2+} is higher in the O_h site (0.4 Δ) than that for the T_d site (~0.2 Δ) due to Δ for $\frac{4}{9}O_h \cong T_d$. Therefore, the Fe^{2+} ion preferentially occupies the O_h site and Fe^{3+} ion does not prefer either type of coordination geometry.

Magnetite has a face-centered cubic (*fcc*) unit cell based on 32 O^{2-} ion which are repeatedly cubic closed packed along the [111] edge. The length of unit cell edge is a = 0.839 nm[55] where the unit cell is made up of eight cubic units with a lattice d spacing of 0.839 nm. It contains 56 atoms, including 32 oxygen atoms, 16 Fe^{3+} and 8 Fe^{2+} and may be denoted as $(Fe^{3+})^{tetr}_8\ [Fe^{3+}Fe^{2+}]^{oct}_8\ O_{32}$. The oxygen anions form a close-packed *fcc* lattice. In the unit cell, additionally, 32 octahedral and 64 tetrahedral sites are present. The Fe^{2+} species reside in 1/4 of the octahedral interstitial sites (i.e. 8 Fe^{2+}) and Fe^{3+} species evenly reside in 1/4 of the octahedral (i.e. 8 Fe^{3+}) and 1/8 of the tetrahedral (i.e. 8 Fe^{3+}) sites, forming an inverse spinel as the structural type.[56] The unique structural property of magnetite is that there are both Fe(II) and Fe(III) ions in the structure (Fe(II)/Fe(III) = 0.5), where it consists of octahedral and mixed octahedral/tetrahedral layers stacked along [111].

The crystal shape of magnetite nanoparticles are classified into four groups: one-dimensional (1-D), two-dimensional (2-D), three-dimensional (3-D), and hybrid nanostructures.[57] 1-D nanoparticles such as nanorods, nanowires, and nanotubes have specific properties, for example, unique electron-transport behaviours caused by shape anisotropy.[58] Nucleation and anisotropic growth processes are essential in the preparation of this category of nanoparticles. 2-D nanoparticles include nanorings, nanoprisms, and nanoplates. Hybrid nanostructures such as FeO/Fe_3O_4 consists of two or more different functional units and provide new and enriched properties for magnetic, optical, catalytic, and biomedical applications.[57] 3-D nanoparticles include spherical, octahedral, and cubic shape materials.[57] Based on the ratio (R) of growth rate in the <100> to that in the <111>, the crystal shape of magnetite is defined. Faster growth along the <100> can form octahedral nanoparticles, whereas faster growth along the <111> can lead to cubic nanoparticles.[59] Spherical nanoparticles were synthesized by using oleic acid and oleylamine as surfactants, with phenyl ether as a solvent, and $Fe(acac)_3$ and 1,2-hexadecanediol as the reactant producing a nanoparticle (4 nm) at high temperature (320 °C) with a liquid phase method producing variable size (5-22 nm) nanoparticles with iron(III) oleates as the precursor.[57] Hydrophilic head groups of the surfactant encompass the hydrophilic nanoparticles and can form micelles that can facilitates very fine spherical nanoparticles due to lowering surface tension of the particle.

Regarding environmental significance of using iron oxide, it has been used over the last decade for removal of heavy metals and other toxic elements, euthrophication compounds, and organic xenobiotics. Iron oxide obliquely affects the environment by influencing the fate (mobility, decomposition) of the substances possessing Lewis base character because of their favourable binding high affinity towards such compounds through surface adsorption or incorporation.[60] Metal anions (arsenate, chromate, phosphate, selenite, etc), acid mine drainage containing high acidity and toxic elements (Pb, Zn, Cu, Cd, As, Ni, Co etc), detoxification of pollutants by reducing a toxic element (e.g., Cr^{6+} to Cr^{3+} using magnetite)[61], and iron oxide-rich waste products (Red mud from the aluminum industries containing about 0.4% Fe and Red gypsum from titanium industries containing about 35% Fe oxide consisting of goethite and hematite) are examples for removal of pollutants by iron oxide in water purification and in natural systems. Nano sized materials, as compared to their bulk counterparts, provide novel distinctive optical, electrical and magnetic properties due to the enhanced surface-to-volume ratio and quantum confinement effects emerge in the nanometre size range. Thus, magnetic nanoparticles are excellent candidates for numerous applications such as multi-terabit per square inch magnetic storage devices, magnetic refrigeration system, ferrofluids (in rotary shaft sealing, dynamic loudspeakers, and computer hard drives), and catalysts. Intended for biomedical purposes, for example, contrast enhancement agents in magnetic resonance imaging (MRI), site-specific drug delivery, hyperthermia agents, and magnetite nanoparticles should be biocompatible, superparamagnetic, and versatile targeting agents.[62] Owing to their non-toxicity and strong magnetic susceptibility, magnetite and maghemite nanoparticles were previously studied for biomedical applications. Below a certain size (<15 nm for magnetite), magnetite nanoparticles display superparamagnetic behavior with zero remanence and zero coercivity.[62]

Frequently, magnetite is non-stoichiometric due to the deficiency of the Fe(III) sub-lattice. Fe(II) may also be partly or fully replaced by the other divalent cations (Mn(II) or Zn(II)). This cation substitution is facilitated by the flexibility of the oxygen framework which can expand or contract to accommodate cations which differ in size from Fe(II) and may be accomplished by changing the unit cell edge length.[55]

On the other hand, maghemite has an analogous crystallographic structure with a cubic unit cell (a = 0.834 nm) to that of magnetite, but differs from magnetite because all or most of the cations are the Fe^{3+}.[55] In each cell of maghemite, 32 O^{2-} ion, $21\frac{1}{3}$ Fe ions, and $2\frac{2}{3}$ vacancies are in place. Eight cations occupy the tetrahedral sites and the remaining cations are arbitrarily spread over the octahedral sites.[55] Vacancies are restricted to the octahedral sites.[55] Slow spontaneous oxidation of magnetite to maghemite near room temperature is a significant environmental process thermodynamically.[63] As indicated above, the variation of structure and physical properties of iron oxide materials may vary according to the synthetic conditions, particularly through the use of templates such as surfactants. Herein we employ a similar strategy by using a preformed carbonaceous substrate such as activated carbon (*vide infra*).

1.3.4 Activated carbon

An activated carbon (AC) [Chemical Abstract Service (CAS) registry number: 7440-44-0 and atomic weight: 12.00 g][64,65] is a carbon-based nano-material which has a high surface-to-volume ratio with a fairly high porosity, and its schematic structure[66] is shown in Fig. 1.8. AC consists primarily of sp^2 graphite crystallites that encompass 3 to 4 parallel hexagonal carbon ring layers, which are alternated by 3.44 - 3.65 Å interlayer spacing. This interlayer spacing is approximately 10 nm in length and is somewhat larger (3.35 Å) than that of graphite.[67] The main recurring structure of AC consists of amorphous graphitic-like sheets, called "*basal planes*", which are arbitrarily cross-linked, irregularly stacked, and enclosed by numerous unpaired electrons.[67]

The exterior of AC is primarily apolar in nature while a minor changes in polarity may occur due to surface oxidation. These specific structural features result in AC with a variable porosity that is valuable for applications in catalysis and adsorption for a broad range of chemical species. Besides, AC contains various atomic groups such as oxygen, hydrogen, nitrogen, phosphorous, and sulfur. The covalently bound atoms are the key heteroatoms that can significantly modify the chemical properties of AC.

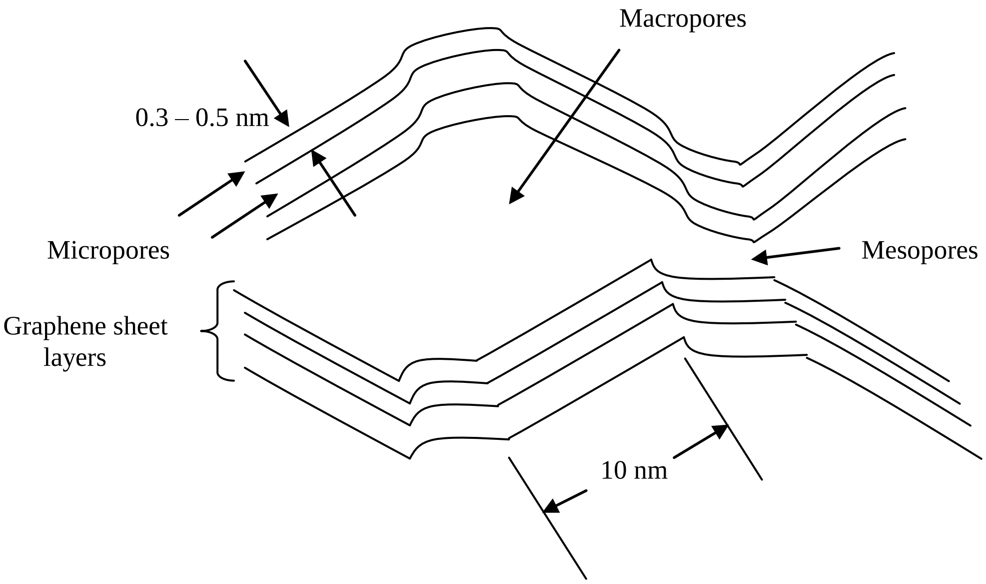

Figure 1.8 Schematic illustration of the layered structure of activated carbon (AC). Straight-line sections denote graphene sheets. Adapted from Ref (66)

According to the classification of International Union of Pure and Applied Chemistry (IUPAC), the array of pore sizes of the porous materials are grouped in Table 1.6.[68]

Table 1.6 IUPAC categorizations of pore sizes

Pores	Pore width (pw)
Ultramicropores	pw < 0.7 nm
Supermicropores	0.7 nm < pw < 2.0 nm
Mesopores	2.0 nm < pw < 50.0 nm
Macropores	50.0 nm < pw

The extremely porous AC framework structure can interact with suitably sized adsorbates within the pore structure or onto the surface of AC. Thus, the micropores of AC can adsorb small molecules (< 2 nm). Macroporous AC can adsorb a large molecule (e.g., γ-cyclodextrin, approximate van der Waals diameter ~ 1.75 nm); however, microporous AC can bind differently sized molecules (e.g., α-cyclodextrin, approximate van der Waals diameter ~ 1.46 nm) based on size exclusion by selectively adsorbing within the micropore sites.[69] To estimate the porosity of AC for industrial applications, molecular iodine is typically used for measuring internal microporosity by measuring the adsorbed amount from a standard solution of iodine (0.02 M) treated for a standard AC sample by the American Society for Testing and Materials (ASTM) D 4607-94 (2006) method. For determining the mesoporosity, methylene blue is suitable for measuring the absorbance of a decolorized standard solution (1 ppm) of methylene blue with a UV spectrophotometer at 668 nm after treating methylene blue for 48 h with a standard AC sample.[70] On the other hand, molasses is applied to determine macroporosity content by measuring the ratio of optical density of the filtrate of molasses solution which adsorbed by a standard AC sample and the unknown sample.[70] The values of iodine (mg/g), methylene blue (mg/g), and molasses adsorbed are approximately equivalent to the specific surface area (m^2/g) of the adsorbent material.

The universal surface functional groups[71] easily found on the surface of AC from typical nitric acid oxidation are shown in Fig. 1.9.

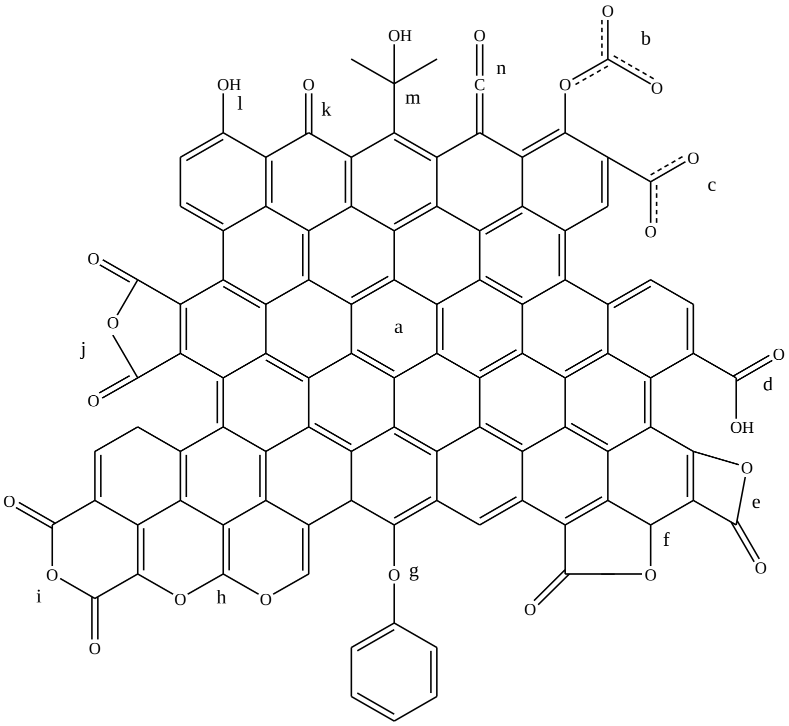

Figure 1.9 Typical surface functional groups on the surface of the oxidized AC illustrating aromatic (a), carboxyl-carbonates (b and c), carboxylic acid (d), 4-membered ring lactone (e), 5-membered ring lactone (f), ether bridge (g), cyclic ethers (h), 6-membered ring cyclic anhydride (i), 5-membered ring cyclic anhydride (j), quinone (k), phenol (l), alcohol (m), and ketene (n). Adapted from Ref. (67). Note that the surface charges and H atoms are not shown in all cases.

The two important surface properties of activated carbon are its hydrophobicity and organophilicity, which are suitable for adsorbing organics for the decolorization of sugar, water purification, and solvent recovery methods, along with the adsorption of petrol vapors in vehicles, multipurpose adsorption in range hoods and other air purification systems. For the application of adsorption from the liquid phase, it is generally advisable to have greater pore diameters than those used for adsorption from the gas phase in order to reduce the mass transfer resistance.[72]

1.3.5 Sorption

1.3.5.1 Introduction

The term sorption generally refers to both absorption and adsorption processes. In addition, adsorption may involve either physisorption or chemisorption, depending on the nature of the process. Absorption is often an entirely reversible process described by partitioning of chemical species within the phase interior of a separate phase (e.g., absorbing water by a sponge).

Chemisorption involves the formation of a covalent bond between an adsorbate and an adsorbent to alter the energy states of the bonding electrons. Physisorption involves noncovalent van der Waals interactions (dispersion and dipolar interactions) between the adsorbate and the adsorbent at lower temperatures. For example, N_2 adsorption on an iron metal surface is a reversible interaction that affords sorption with ~ 40 kJ/mol (ΔH_{ads}) on the substrate. However, chemisorption involves chemical bond (usually covalent or dative bond) formation between the adsorbate and the adsorbent at higher temperature. For example, N_2 adsorption on an iron surface at 800 K to form iron nitride is an irreversible process that affords monolayer sorption with ~ 400 kJ/mol (ΔH_{ad}) on the substrate. The characteristic properties of these two types of adsorption are described in Table 1.7.[73]

Table 1.7 Comparison of physisorption and chemisorption

	Physisorption	**Chemisorption**
Heat of Adsorption	Low (<2 or 3 times latent heat of evaporation)	High (>2 or 3 times latent heat of evaporation)
Selectivity	Non specific	Highly Specific
Adsorption layer	Mono or Multi	Mono
Absorbate dissociation	No dissociation	May involve
Temperature	Only important at quite low temperatures	Occurs over a broad range of temperatures
Adsorption reaction	Rapid, non-activated, reversible, weak and long-range bonding	Activated, may be slow and irreversible, strong and short-range bonding
Electron transfer	No electron transfer in adsorbate polarization	Electron transfer forming a bond between adsorbate and surface of adsorbent

Physisorption processes involved van der Waals (dispersion-repulsion) and electrostatic interactions including polarization, dipole, and quadrupole (e.g., benzene, due to its D_{6h} symmetry) interactions. van der Waals contributions are always present, but the electrostatic contributions are noteworthy in the case of adsorbent such as zeolites which have cation exchange sites.[74]

Adsorption in solution leads to an overall lowering of the Gibbs energy of a system (Gibbs free energy, ΔG). The entropy of the adsorption (ΔS) for the system may decrease or increase with the level of adsorption depending on the role of solvent. Therefore, Gibbs free energy change is negative as the enthalpy (the heat of adsorption, ΔH) is usually negative (i.e. exothermic).

Sorption processes in aqueous solution are often unique compared to gas media in that there is a charge-balance interaction to maintain equilibrium between sorption of ions from the adsorbate and desorption of soluble ions from the adsorbent simultaneously. Additionally, all reaction sites on the surface are non-equivalent as compared to gas sorption due to surface heterogeneity by the occurrence of solvent effects. For that reason, the distribution of heterogeneous sorption sites are based on the surface reactivity of the adsorbent.

It is believed that there are three different surface heterogeneities on the surface: physical, chemical, and induced heterogeneity.[75,76] Physical heterogeneities are caused by geometrical diversities in size and shape (e.g., porosity, crevices, edges, corners, and step positions) on the surface. Chemical heterogeneity arises from different surface functional groups including contaminants on the surface. Induced heterogeneity results from the binding energy of the first layer of adsorbates to the surface, which can influence the binding energy of the following layer of bound adsorbates. However, regardless of surface heterogeneity and interaction energy[75] between adsorbent and adsorbate, there is usually a decrease in surface coverage with increasing chemisorption. Nonetheless, physisorption occurs between adsorbed molecules on a homogeneous surface, resulting in multi-layers; which may increase as the degree of surface coverage increases.

Since adsorption occurs on the surface, some definitions are illustrated as shown in Fig. 1.10 and 1.11 for the adsorbent, adsorbate, adsorptive, and the surface. Adsorbate refers to its bound state (solid sphere) on the solid surface and adsorptive is in its unbound state (open sphere) in bulk solution.

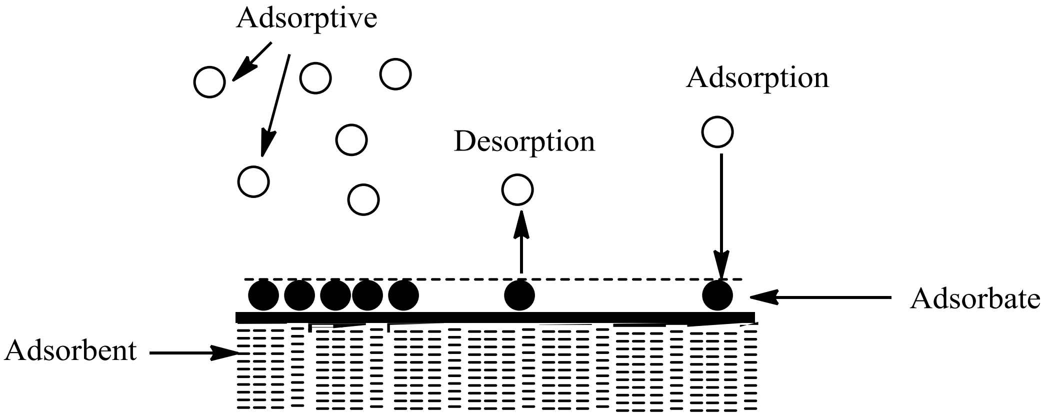

Figure 1.10 Schematic illustration of the adsorbent, adsorbate, and adsorptive

Many definitions exist that describe surfaces including some rigorous definitions are as follows: 1) a surface represents the outer or the uppermost boundary of a solid or liquid object, where the bulk properties are no longer sufficient to describe the properties of the system, and 2) a surface always determines a thermodynamic phase boundary, where the physical and chemical properties of the adjacent phases change abruptly.[77] Therefore, in the surface region, the interaction forces responsible for the bulk properties change and they become asymmetric since the outermost bonds are unsaturated, resulting in a peculiar chemical reactivity of the surface. As shown in Fig. 1.11, the most important consequence is that the surface becomes capable of adsorbing foreign atoms or molecules.[77]

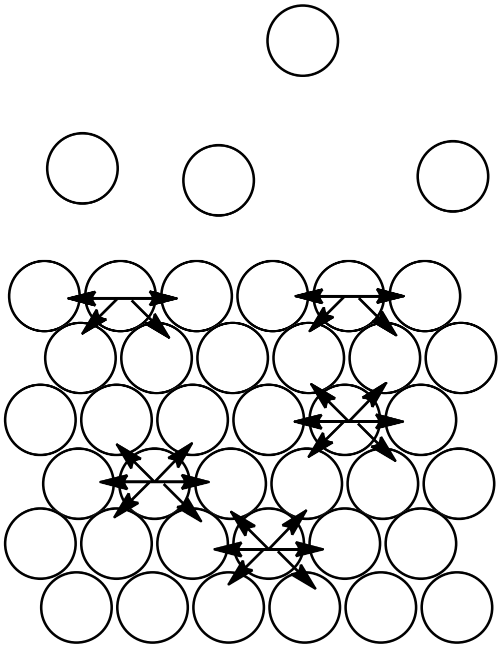

Figure 1.11 Diagram of surface structure and surface interactions

The surfaces of single crystals are well-defined geometrically and electronically. They are rarely used in heterogeneous catalysis except using in photochemical processes and have the benefit to offer access to the physics and chemistry of the basic steps of a catalytic reaction ("model systems"). The adsorption onto single crystal surfaces can often be described by a basic adsorption isotherm models.[77] Polycrystalline and heterogeneous surfaces are very important in heterogeneous catalysis since they have a great surface area-to-volume ratio due to the presence of micro-, meso- or macropores. Active carbon charcoals, carbon nanotubes, zeolites, alumina, and silica are examples of such porous materials. Adsorptive processes on these porous surfaces are frequently well described by the BET and Sips adsorption isotherms. As well, the existence of mesopores can modify the thermodynamic phase equilibria owing to a vapour pressure depression predicted by the Kelvin equation (curvature effect).[77]

1.3.5.2 Sorption isotherm models

An adsorption isotherm is a measurement or at least a plot showing the results of a measurement in the gas or solution phase at a constant temperature. At equilibrium, the adsorbed amount of an adsorbate on a surface of an adsorbent (Q_e) is given in equation (1-2).

$$Q_e = \frac{(C_o - C_e) \times V}{m} \tag{1-2}$$

C_e is a concentration at equilibrium (mol/L), C_o is the initial concentration of the adsorbate (mol/L), V is a volume of the adsorbate in solution (L), and m is a mass of the adsorbent (g).

Adsorbate in solution (L), and m is a mass of the adsorbent (g). Nonlinear adsorption isotherm models can be expressed as linear forms when plotted in reciprocal coordinates. Various adsorption isotherm models include two-parameter isotherms [Langmuir, Freundlich, BET (Brunauer-Emmett-Teller), Temkin, Dubinin-Radushkevich] and three-parameter isotherms (Redlich-Peterson, Khan, Toth, and Sips), and are shown in Table 1.8.

Table 1.8 Typical adsorption isotherm models

Isotherm	Non-linear	Linear	Plot
Two-parameter models			
Freundlich[78]	$Q_e = K_F C_e^{1/n}$	$log(Q_e) = log(K_F) + \frac{1}{n} log(C_e)$	$log(Q_e)\ vs\ log(C_e)$
Langmuir[79]	$Q_e = \frac{K_L C_e Q_m}{(1 + K_L C_e)}$	$\frac{C_e}{Q_e} = \frac{1}{K_L Q_m} + \frac{1}{Q_m} C_e$	$\frac{C_e}{Q_e}\ vs\ C_e$
		$\frac{1}{Q_e} = \frac{1}{Q_m} + \frac{1}{K_L Q_m C_e}$	$\frac{1}{Q_e}\ vs\ \frac{1}{C_e}$
		$Q_e = Q_m - \frac{Q_e}{K_L C_e}$	$Q_e\ vs\ \frac{Q_e}{K_L C_e}$
		$\frac{Q_e}{C_e} = K_L Q_m - K_L Q_e$	$\frac{Q_e}{C_e}\ vs\ Q_e$
BET[80]	$Q_e = \frac{Q_m C_e K_{BET}}{\{(1 - C_e)[1 + (K_{BET} - 1)C_e]\}}$	$\frac{C_e}{[(C_s - C_e)q_e]} = \frac{1}{Q_m K_{BET}} + [\frac{(K_{BET} - 1)}{Q_m K_{BET}}] \frac{C_e}{C_s}$	$\frac{C_e}{[(C_s - C_e)q_e]}\ vs\ \frac{C_e}{C_s}$
Temkin[81]	$Q_e = \frac{RT}{b_T} lnA_T C_e$	$Q_e = \frac{RT}{b_T} lnA_T + (\frac{RT}{b_T}) ln(C_e)$	$Q_e\ vs\ ln(C_e)$
Dubinin-Radushkevich[82]	$Q_e = (Q_D) exp(-B_D \varepsilon^2)$	$ln(Q_e) = ln(Q_D) - B_D \varepsilon^2$	$ln(Q_e)\ vs\ \varepsilon^2$
Three-parameter models			
Sips[83]	$Q_e = \frac{Q_m K_S C_e^n}{1 + K_S C_e^n}$	-	-

Toth[84]	$Q_e = \frac{K_T C_e}{(a_T + C_e^t)^{1/t}}$	$ln(\frac{Q_e}{K_T}) = ln(C_e) - \frac{1}{t} ln(a_T + C_e)$	$ln(\frac{Q_e}{K_T})\ vs\ ln(C_e)$
Khan[85]	$Q_e = \frac{Q_m b_K C_e}{(1 + b_K C_e)^{a_K}}$	-	-
Redlich-Peterson[86]	$Q_e = \frac{K_R C_e}{1 + a_R C_e^g}$	$ln(K_R \frac{C_e}{Q_e} - 1) = g\ ln(C_e) + ln(a_R)$	$ln(K_R \frac{C_e}{Q_e} - 1)\ vs\ ln(C_e)$

Note: 1. The maximum adsorption at monolayer surface coverage at equilibrium: Q_m (mol/g)

2. Equilibrium constants: Freundlich (K_F, L/g), Langmuir (K_L, g/mol), BET (K_{BET} L/g), Sips (K_S, L/g), Redlich-Peterson (K_R, L/g), and Temkin (A_T, L/g)

3. C_s is a saturated concentration of a solute (mol/L) for BET isotherm

4. q_e is the amount of the adsorbate loaded per unit adsorbent at equilibrium

5. Model parameter constant: Redlich-Peterson ($a_{R,}$ L/mg), Khan (b_K), Temkin (b_T, J/mol), Dubinin-Radushkevich (Q_D, mg/g; B_D, mol^2/kJ^2), Toth (a_T)

6. Model exponent: Freundlich (n), Redlich-Peterson (g), Khan (a_K), Toth (t), Sips (n)

7. Polanyi potential: ε (J/mol)

The Langmuir adsorption isotherm defines the equilibrium parameters after considering the following assumptions: 1) monolayer adsorption (the adsorbed layer is one molecule thick), 2) adsorption takes place at specific homogeneous sites within the adsorbent, 3) once an adsorptive occupies a site, no further adsorption can take place at that site, 4) adsorption energy is constant and does not depend on the degree of occupation of the active center of the adsorbent, 5) the strength of the intermolecular attractive forces tend to fall off rapidly with distance, 6) the adsorbent has a finite capacity for the adsorbate (at equilibrium, a saturation point is reached where no further adsorption can occur, 7) all sites are identical and energetically equivalent, 8) the adsorbent is structurally homogeneous, 9) there is no interaction between molecules adsorbed on neighboring sites.[87]

At dilute adsorbate conditions, the Langmuir isotherm may adopt a linear profile. Since K_L denotes the affinity between adsorbent and adsorbate, as the K_L value increases, the monolayer adsorption capacity increases as well with a well-defined plateau as the surface becomes saturated. The dimensionless constant separation factor or equilibrium parameter (R) of Langmuir isotherm model are expressed by equation (1-3), where K_L is the Langmuir constant and C_o is the initial concentration of adsorbate.[88]

$$R = \frac{1}{(1+K_L C_o)} \tag{1-3}$$

The R-value is interpreted according to the type of sorption isotherm shown in Table 1.9.

Table 1.9 The range of R-values which vary by the types of isotherms

***R* Value**	**Type of equilibrium (Langmuir -type)**
$R > 1$	Unfavorable
$R = 1$	Linear
$0 < R < 1$	Favorable
$R = 0$	Irreversible

The Freundlich adsorption isotherm represents an empirical relationship which assumes an exponential decay of the distribution of the adsorption site energy that may be applicable to non-ideal sorption processes on heterogeneous surfaces and includes multi-site sorption. This approach assumes that the stronger binding sites are occupied preferentially and then the binding strength decrease as the surface coverage increases. The method is criticized for missing a fundamental thermodynamic basis since it does not reduce to the linear relationship at low concentration.

The BET (Brunauer-Emmett-Teller) adsorption isotherm is a theoretical equation as an extended form of the Langmuir isotherm by accounting for multilayer surface coverage that is widely applied in a gas-solid system. This model has several assumptions: 1) multi-layer adsorption is achievable. However, owing to the influence of the adsorbent, the van der Waals interactions on the surface of the adsorbent will be more favourable among molecules in the gas phase. Intermolecular forces involved in adsorption processes are greater for the first layer and secondary for the subsequent layers. This implies that the heat of adsorption of the 1st layer is greater than that of the 2nd and subsequent layers. 2) There are no lateral molecular interactions between the adsorbed molecules as in the case of Langmuir. 3) The surface is uniform and consistent. The disadvantages of this adsorption model are as follows: 1) surface is assumed to be homogenous which is not always obeyed. 2) Lateral molecular interactions between the adsorbed molecules are neglected. 3) The heat of adsorption from 2nd layer is assumed to be equal to subsequent layers which are generally not obeyed.

The Temkin adsorption isotherm contains a factor (b_T, J/mol) that explicitly takes into the account the adsorbent–adsorbate interactions. By disregarding the extremely low and large value of the concentration scale, this model hypothesizes that the heat of adsorption (function of temperature) of all molecules in the layer would decrease linearly rather than logarithmically with coverage.[89]As seen from Table 1.8, this model is derived for describing a uniform distribution of binding energies. The Temkin equation is exceptional for predicting the parameters related to gas phase equilibrium adsorptive processes.

The Dubinin-Radushkevich isotherm has spoken that the sorption characteristic is associated with the porous structure of the adsorbent. The Dubinin-Radushkevich constant (B_D) obtained by the equation (1-4) below is related to the mean free energy of adsorption per mole of the adsorbate (E, kJ/mol) as it is transferred to the surface of the solid from infinite distance in the solution.[90]

$$E = \frac{1}{\sqrt{2B_D}} \tag{1-4}$$

The Polanyi parameter (ε ; J/mol) is shown by equation (1-5) and other parameters are defined as follows: R, T, and C_e are the gas constant (8.314 J/mol K), absolute temperature (K), and the adsorbate equilibrium concentration (mol/L), respectively. One major contribution of this isotherm model shows that it is temperature-dependent. When adsorption data at different temperatures is plotted as a function of the logarithm of amount absorbed *vs*. the square of potential energy, all appropriate data will lie along the same curve, referred to as the characteristic curve.

$$\varepsilon = RT\ ln(1 + \frac{1}{C_e}) \qquad (1\text{-}5)$$

The Redlich-Peterson isotherm was the first modified three-parameter sorption isotherm used to modify the Langmuir and Freundlich equations. There are two limiting behaviors: the Langmuir form (g =1), and the linear form (g = 0). At low adsorbate concentration, it approximates the linear relationship and at high adsorbate concentration, resembling the Freundlich isotherm.

The Khan isotherm is a generalized model which represents a wide range of multi-components and adsorbate systems which display low solubility in aqueous solution.

The Toth isotherm is another empirical equation developed to improve the Langmuir isotherm that was verified to be practical for describing adsorption in heterogeneous systems.

The Sips or composite Langmuir-Freundlich isotherms are useful for predicting the heterogeneous adsorption behavior and represent limiting behavior of the equation depending on the *n* value. If *n* value is very low, Freundlich isotherm behaviour occurs which may not comply with the linear relationship. As the *n* value increases, mono or multi-site sorption behavior is predicted.

Giles has previously shown a generalized graphical modeling of sorption behaviour, as shown in Fig. 1.12.[91]

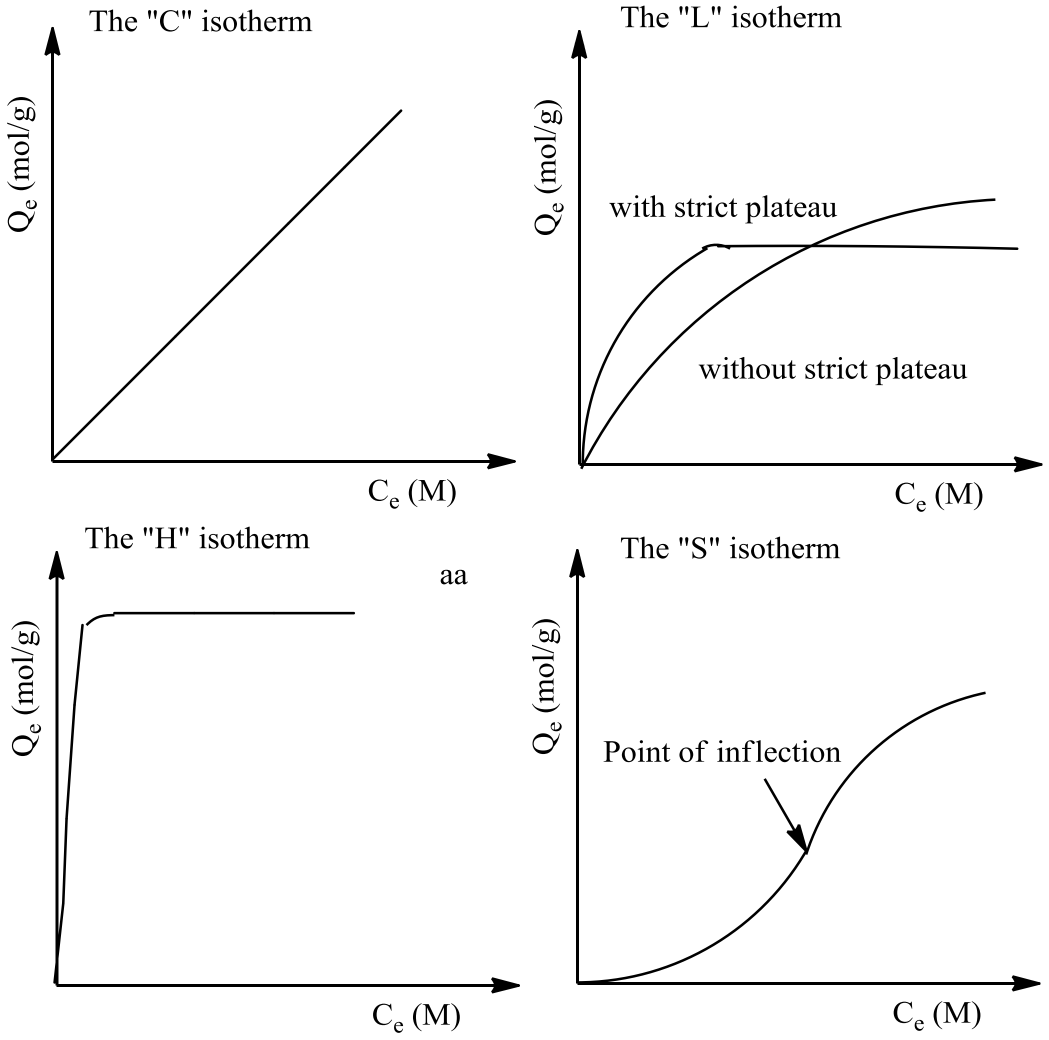

Figure 1.12 The four main types of adsorption isotherms (adapted from Ref. 91)

According to Limousin *et al.*,[92] the type ''C'' isotherm goes through the origin and is linear in nature which means that the ratio between the equilibrium concentration in solution (C_e) and adsorbed concentration on the solid (Q_e) are the same at any concentration. The type ''C'' isotherm is often used for a narrow range of concentration or at very low concentrations rather than an accurate description as linear adsorption behavior. For an ''L'' type isotherm, the ratio between the equilibrium concentration in solution (C_e) and the adsorbed concentration in the sorbent phase (Q_e) decreases as the solute concentration (C_e) increases. The concave concentration dependence suggests a continuous saturation of the solid. For an ''H'' type isotherm, the initial slope is very high because the adsorbate exhibits an occasional high affinity for the adsorbent.[93] For an ‘‘S’’ type isotherm, the curve is (Langmuir) sigmoidal and thus has a point of inflection. This type of isotherm always brings with cooperative interaction between adsorbates, in which the adsorbate can interact with the neighboring adsorbate. This lateral interaction results in a two-dimensional condensation take places over the inflection point where the total surface coverage abruptly increases leading to the flat region. This type of adsorption isotherm is observed for an adsorbent with a flat and homogenous surface.

Another categorization for the types of gas adsorption isotherms has been introduced by Brunauer, Deming, and Teller (BDT) and their six characteristic solid-gas isotherms (Type I, II, III, IV, V, and VI) are shown in Fig. 1.13.[94]

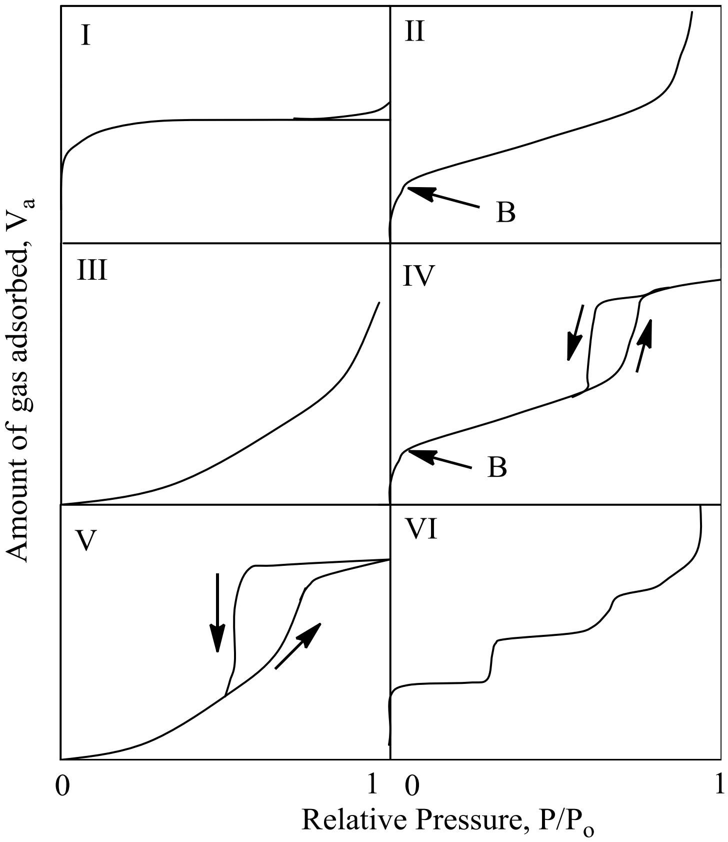

Figure 1.13 Various types of solid-gas adsorption isotherms, where P = equilibrium pressure and P_o = saturation vapor pressure

The Type I adsorption isotherm symbolizes the adsorption resulting from uptake by a microporous structure because most micropore fillings occur at relatively low pressure (< 0.1) and the adsorption process is typically completed at about halfway to saturation ($P/P_o \approx 0.5$) of the saturated vapor pressure (P_o). Representative adsorption profiles of this group include the adsorption of nitrogen onto AC at 77 K and ammonia onto AC at 273 K.

Type II adsorption isotherms involve physical adsorption of gases by non-porous solids. Point B is the end of monolayer surface coverage and multilayer coverage starts right after the point B. ACs with mixed micro- and meso-porosity show Type II isotherms.

Type III adsorption isotherms are characteristic of weak interactions between adsorbate-adsorbent systems such as non-porous and microporous adsorbents. As adsorption occurs, the interaction between adsorbate and the adsorbed layer is more pronounced than the interactions between adsorbate and adsorbent. The weak adsorbate/adsorbent interactions give rise to low loadings at low relative pressures. However, beyond the first adsorption point, much greater adsorption may occur resulting in maximum loadings at higher P/P_o values. The adsorption of water onto AC where the primary adsorption sites are oxygen falls into this category.

Type IV adsorption isotherms demonstrate a hysteresis loop attributed to capillary condensation, which is commonly observed for mesoporous materials. Point B is the end of monolayer surface coverage and multilayer coverage starts right after point B. These adsorption isotherms show a restricted loading at high relative pressures.

Adsorption isotherms Type V attain microporous or mesoporous adsorbents and are convex at the high relative pressure. The motivating force of uptake is the same as Type III adsorption isotherms. Water adsorption on AC at 100 °C is an example of this type of adsorption isotherm.[95]

Type VI adsorption isotherms are congruent with extremely homogeneous, non-porous surfaces. The complete development of a monolayer that connects to the step height is fulfilled before evolution to a subsequent layer. Interestingly, a porous metal-organic framework showed the three-step adsorption isotherms of N_2 and O_2 gas at 77 K and 87 K and a two-step adsorption isotherm for CO_2 gas at 195 K.[96]

Type II, IV, and VI adsorption isotherms represent stronger interaction of adsorbate/adsorbent than the interaction of adsorbate-adsorbate as measured by BET method. Type III and V adsorption isotherms represent weak interaction between gas phase adsorbates and an adsorbent.

The hysteresis loop for the Type IV and V adsorption isotherms along with the Type II and III adsorption isotherms arises from the capillary condensation of vapor due to several possible effects. At any known value for amounts of gas adsorbed (V_a), a hysteresis loop may be observed when P/P_o for in desorption branch is lower than that for adsorption profile. Such hysteresis loops occur due to dissimilarities in the shape of the meniscus of cylindrical pores with both ends open and the presence of ink-bottle type pores, i.e., narrow neck and wide body. Hysteresis loops are empirically classified using the IUPAC system, as shown in Fig. 1.14.

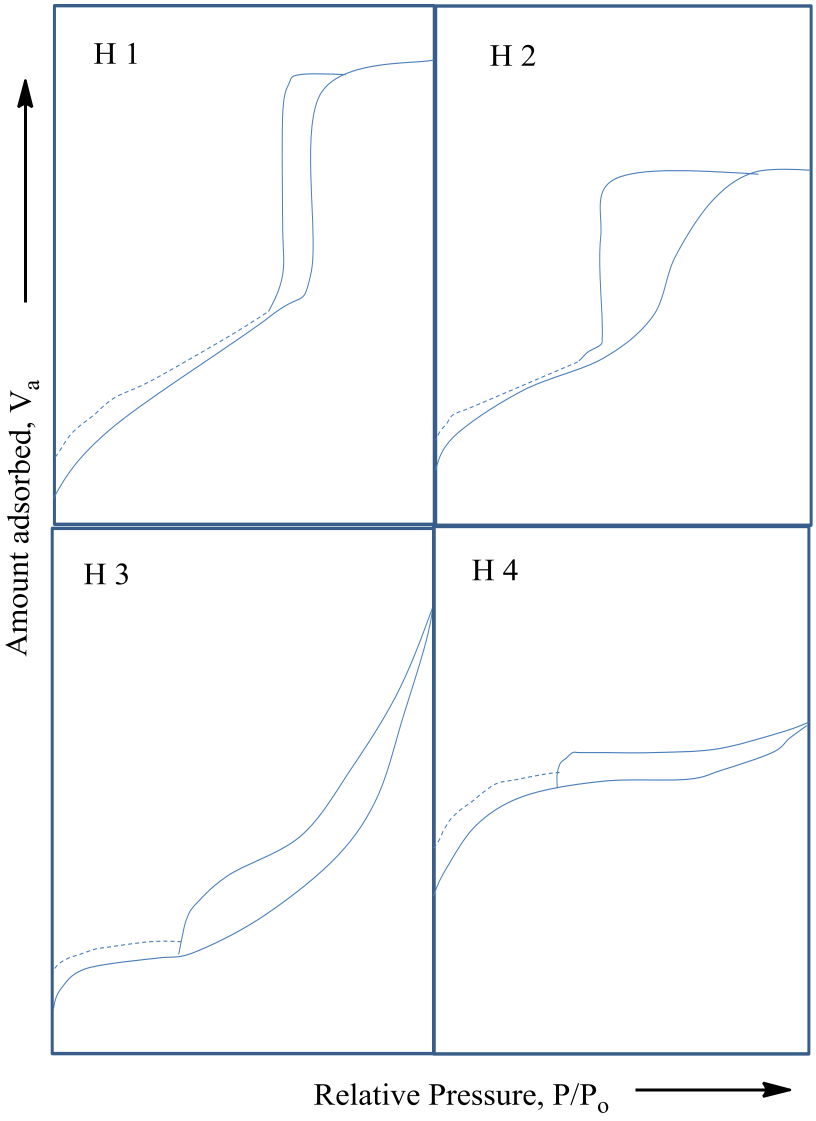

Figure 1.14 IUPAC classification of hysteresis loops for various types of isotherms

In accordance with this arrangement, Type H1 is often connected to porous materials displaying a narrow distribution of fairly uniform (cylindrical-like) pores. Materials that yield Type H2 hysteresis have a more complex pore structure in which network properties such as pore blocking or percolation are significant. Type H3 hysteresis do not show any restrictive adsorption at high relative pressure (P/P_o). This pattern can be attributed to the presence of non-rigid aggregates of plate-like particles or groups of slit-shaped pores. Theoretically, this pattern does not offer a reliable assessment of the pore size distribution or the total pore volume. Type H4 hysteresis loops are usually popular with complex materials containing both micropores and mesopores. All Types H3 and H4 hysteresis loops contain a typical *step-down* profile in the desorption branch linked to the hysteresis loop closure.[97]

Hysteresis loops that result from a vapour pressure depression in a capillary tube can be explained by the Kelvin equation, which represents pore condensation in a capillary. This can occur when a certain relationship existed between vapor pressures and a capillary radius as shown in equation (1-6), where P is the equilibrium pressure in pores with a (Kelvin) radius r, P_o is the saturation vapor pressure of the pore on planar surface, γ is pore surface tension, V_m is molar volume (molar mass/σ (density)), R is the universal gas constant, T is the temperature in Kelvin, r is the radius of the pore. A molecule on the surface of a highly curved meniscus tends to re-condense rather than evaporate from the surface unlike one on the planar surface is apt to evaporate readily. Therefore, a capillary pore fills spontaneously with condensed liquid depending on the contact angle θ (complete wetting at $\theta = 0^o$, incomplete wetting at $\theta = 20^o$).

$$ln(\frac{P}{P_o}) = -\frac{2\gamma V_m}{RTr} cos\theta \qquad (1\text{-}6)$$

Adsorption isotherms can provide helpful information on the physicochemical properties of the adsorbent such as specific surface areas and adsorption capacity. Specific surface area can be determined from equation (1-7),[98] where Q_m is the maximum adsorption at monolayer coverage at equilibrium (mol/g), N is the Avogadro's number (6.02×10^{23} mol^{-1}), A is the cross-sectional molecular area of the adsorbate (m^2), and X is the surface coverage factor (X = 1 for PNP, X = 2 for methylene blue). The surface coverage factor (X) is the number of dye ions in a micelle or the aggregation number of dye ions because monoionic dyes (e.g., PNP) can form monolayer of ionic micelle when they are adsorbed at the surface of the adsorbent.[98,99]

$$Surface\ area\ (\frac{m^2}{g}) = (\frac{Q_m\ N\ A}{X}) \qquad (1\text{-}7)$$

The cross-sectional molecular area of adsorbates are summarized in Table 1.10.[100,101]

Table 1.10 The cross-sectional area (nm^2) occupied by the adsorbates

Adsorbate	**Liquid**	**Solid**
N_2	0.162	0.138
Ar	0.138	0.128
Kr	0.150	0.143
O_2	0.136	0.121
CO_2	0.195	
CO	0.163	
C_4H_{10}	0.469	
***p*-nitrophenol (PNP)**	0.525 (flat)	
	0.250 (vertical)	
Methylene blue (MB)	1.20 (flat-dimer)	
	0.600 (vertical-monomer)	
***o*-phenanthroline (OP)**	0.600	

The enthalpy at a fixed surface coverage (θ) is called the isosteric enthalpy (ΔH_θ) as defined by equation (1-8) which is formulated based on the van't Hoff equation when the adsorption isotherms are obtained at three or more different temperatures; where T is the temperature in Kelvin, R is the gas constant, K_{eq} is the equilibrium constant. The slope and the *y*-intercept are the same as $-\frac{\Delta H^\circ}{R}$ and $\frac{\Delta S^\circ}{R}$, respectively, because lnK_{eq} is plotted versus $1/T$. The standard Gibbs energy change (ΔG°) is calculated using equation (1-9).

$$lnK_{eq} = -\frac{\Delta H_\theta^\circ}{RT} + \frac{\Delta S^\circ}{R} \quad (1\text{-}8)$$

$$\Delta G^\circ = \Delta H^\circ - T\Delta S^\circ \quad (1\text{-}9)$$

One may envisage the relationship between K_{eq} and T for expecting isosteric enthalpy values because they are inversely proportional to each other. In the case where K_{eq} decreases as T increases for an exothermic reaction, K_{eq} increases as T increases in an endothermic reaction because ΔS depends on the equilibrium condition of adsorption [$\Delta G = \Delta H - T\Delta S$ and $\Delta S = (\Delta H +$

ΔG) / T]. ΔS will be less favorable as T increases in an exothermic reaction, while ΔS will be more favorable as T increases in an endothermic reaction. As a result, K_{eq} will increase, as ΔS are favored.

1.3.5.3 Sorption kinetic models

To understand the details involved for an adsorption and desorption process, we must characterize the parameters related to the equilibrium and kinetics of the process. In connection with adsorption/desorption processes, thermodynamic data merely present information of the final state of a system, but kinetics deals with changes in chemical potential according to time and is concerned especially with rates of change for a given process.[102] Kinetics is a basic expression referring to time-dependent phenomena. Chemical kinetics can be defined as the "study of the rate of chemical reactions (chemical kinetics or, reaction-controlled kinetics) and of the molecular processes by which reactions occur where transport is limiting (transport-controlled kinetics)".[103] Most adsorption in solution and in soil are a combination of these two kinetic processes because of heterogeneity and multi-site sorption by the adsorbents. There are two key reasons for studying kinetics of the adsorption process: 1) to predict how quickly reactions approach equilibrium or quasi-state equilibrium, and 2) to investigate reaction mechanisms (elementary steps). Kinetic parameters including rate constants, activation energy, enthalpy change, entropy change, and free energy are obtained by manipulating kinetic data using relevant kinetic equations such as the Arrhenius and Eyring equations.

Models for adsorption kinetics differ from those of regular chemical kinetics such as "First" and "Second" order reactions because it is often incorrect to apply these simple kinetic models to a system where sorption occurs with solid surfaces. These processes are hardly ever homogeneous in nature since the effects of transport phenomena and chemical reactions are often experimentally non-divisible.[104] As an alternative, adsorption in solution that takes place with excess adsorbent, Pseudo-First Order (PFO) and Pseudo-Second Order (PSO) reaction equations have been employed. To determine the apparent overall rate constant (k), the (PFO) model (equation 6) proposed by Lagergren[105] and the (PSO) model (equation 7) proposed by Blanchard,[106] developed by Ho,[107] and derived theoretically by Azizian[102] are available as shown in Table 1.11.[108] The terms q_t (mg/g) is the uptake level of the adsorbate by an adsorbent at time t, q_e (mg/g) is the adsorbed amount of adsorbate uptake at equilibrium conditions, C_o and C_t (mg/L) are the adsorbate concentrations at $t = 0$ and $t = t$, respectively, and m_s (g/L) is the amount of adsorbent in the solution, where k_1 and k_2 are the overall PFO rate constant (min^{-1}) and the overall PSO rate constant (g mg^{-1} min^{-1}). Integration of the equations (1-10) and (1-11) at the boundary conditions q_t = 0 at t = 0 and q_t = q_t at t = t with rearrangement affords the equations listed in Table 1.11.

$$\frac{\mathrm{d}q_t}{\mathrm{d}t} = k_1(q_e - q_t) \tag{1-10}$$

$$\frac{\mathrm{d}q_t}{\mathrm{d}t} = k_2(q_e - q_t)^2 \tag{1-11}$$

Table 1.11 Kinetic models for describing heterogeneous adsorptive processes

Kinetic model	**Equation**	**Plot**
non-linear PFO	$q_t = q_e(1 - e^{-k_1 t})$	q_t vs. t
	$\frac{C_t}{C_o} = 1 - \frac{m_s q_e}{C_o}(1 - e^{-k_1 t})$	$\frac{C_t}{C_o}$ vs. t
linear PFO	$ln(q_e - q_t) = ln(q_e) - k_1 t$	$ln(q_e - q_t)$ vs. t
	$log(q_e - q_t) = log(q_e) - \frac{k_1}{2.303}t$	$log(q_e - q_t)$ vs. t
non-linear PSO	$q_t = \frac{k_2 q_e^2 t}{1 + k_2 q_e t}$	q_t vs. t
	$\frac{C_t}{C_o} = 1 - \frac{m_s q_e}{C_o}\frac{q_e k_2 t}{1 + q_e k_2 t}$	$\frac{C_t}{C_o}$ vs. t
linear PSO	$\frac{1}{q_e - q_t} = \frac{1}{q_e} + k_2 t$	$\frac{1}{q_e - q_t}$ vs. t
	$\frac{t}{q_t} = \frac{1}{k_2 q_e^2} + \frac{1}{q_e}t$	$\frac{t}{q_t}$ vs. t
	$\frac{1}{q_t} = \frac{1}{q_e} + \frac{1}{k_2 q_e^2}\frac{1}{t}$	$\frac{1}{q_t}$ vs. $\frac{1}{t}$
	$q_t = q_e - \frac{1}{k_2 q_e}\frac{q_t}{t}$	q_t vs. $\frac{q_t}{t}$
	$\frac{q_t}{t} = k_2 q_e^2 - k_2 q_e q_t$	$\frac{q_t}{t}$ vs. q_t

Note; $q_t = \frac{C_o - C_t}{m_s}$

Considering the reaction of adsorption (forward step) and desorption (reverse step) of an adsorbate A with adsorbent S in solution in equation (1-12), the apparent rate constant k_1 is a combination of the adsorption (k_a) and the desorption (k_d) rate constant as shown in the equation (1-13),where C_o is the initial concentration the adsorbate A.

$$\mathrm{A + S} \underset{k_d}{\overset{k_a}{\rightleftharpoons}} \mathrm{SA} \tag{1-12}$$

$$k_1 = k_a C_o + k_d \tag{1-13}$$

Thus, equation (1-13) shows that the observed rate constant (k_1) is a linear function of the initial concentration of the adsorbate A and a plot of k_1 vs. C_o gives a straight line with k_a and k_d as the slope and intercept, respectively. Evaluating k_1 at various initial concentrations enables calculation of k_a, k_d, and the equilibrium constant $K_{eq} = \frac{k_a}{k_d}$.[102] Therefore, k_1 is not merely the intrinsic adsorption rate constant. If the initial concentration of the adsorbate is very high compared to the maximum amount of the adsorbed species onto the surface of the adsorbent (i.e., adsorbent with low surface area or few surface reaction sites), then the observed rate constant favors the PFO reaction model. In contrast, if C_o is not too high, the overall rate constant obeys the PSO reaction model. [102]

The PFO reaction model is criticized for several reasons: 1) the linearized equation does not give theoretical q_e values that agree with the experimental q_e values and 2) the plots are only linear over approximately the first 30 minutes. Beyond this initial 30 minute period, the experimental data and theoretical results do not correlate well,[109] 3) the parameter $k(q_e-q_t)$ does not represent the number of available sites, and 4) the parameter log(q_e) is an adjustable parameter, often it is found not equal to the intercept of a plot of log(q_e-q_t) against t, whereas in a true first order process, log(q_e) should be equal to the intercept of a plot of log(q_e-q_t) against t.[104] Fitting experimental data using the PFO equation, the equilibrium sorption capacity, q_e, must be identified. One has to find a suitable method of extrapolating the experimental data to $t = \infty$, or treat q_e as an adjustable parameter to be determined by trial and error. For this reason, it is necessary to use a trial and error based method to obtain the equilibrium sorption capacity, q_e as shown in the equation (1-14), where the value of t_o is the adjustable parameter that makes the equilibrium sorption capacity, q_e, suitable for use in the following kinetic expression.

$$log(q_e - q_t) = log(q_e) - \frac{k_1}{2.303}(t + t_o) \tag{1-14}$$

However, despite this limitation, this model has been widely used to describe the sorption of metal ions onto sorbents.

In adsorption based kinetic diffusion models, it is generally known that a typical liquid/solid adsorption processes involves a series of steps: 1) transport of the adsorbate from the solution (boundary layer) to the external surface of the adsorbent (film or inter-phase diffusion), 2) diffusion of the adsorbate from the pore mouth through the adsorbent pores to the immediate area of the internal surface of the adsorbent, where the chemical reaction take places (pore or intra-particle diffusion), 3) binding of the adsorbates on the adsorbent surface, and 4) reaction at specific active sites on the adsorbent surface (mass-action law). The final process for physical adsorption is a very rapid step and may be negligible. Thus, the kinetic process of adsorption is always controlled by liquid film diffusion or intra-particle diffusion, or a combination of these diffusion processes.

Weber-Morris found that in many adsorption processes, adsorbate uptake changes approximately proportionally with $\sqrt{t}$ rather than with the contact time t,$q_t = k_{int}\sqrt{t}$, where k_{int} is the intra-particle diffusion rate constant.[110] A plot of q_t vs. $\sqrt{t}$ should be a straight line with a slope k_{int} when the intra-particle diffusion is a rate-controlling step. For the Weber-Morris model, it is necessary for the q_t vs. $\sqrt{t}$ plot to go through the origin if the intra-particle diffusion is the sole rate-controlling step. However, it is not always the case and adsorption kinetics described by multi-linear lines may be controlled by two or more steps of film diffusion and intra-particle diffusion. Thus, the adsorption-based diffusion kinetics is controlled by intra-particle diffusion as described by the straight line through the origin and by film diffusion along with intra-particle diffusion described by multiple straight lines.

Temperature effects on the rate of a reaction are well described by Arrhenius and Eyring equations. In a chemical process, the macroscopic rate conbstant (k_{obs}) in the Arrhenius equation (1-15) and the microscopic single-step reaction rate constant (k_{obs}) in the Eyring equation (1-16) are related to temperature, T, as described by equation (1-15) and (1-16).

$$ln(k_{obs}) = -(\frac{\mathrm{E_a}}{\mathrm{R}})\frac{1}{\mathrm{T}} + \ln(\mathrm{A}) \qquad (1\text{-}15)$$

$$ln\,(\frac{k}{T}) = ln(\frac{k_B}{h}) + \frac{\Delta S^{\ddagger}}{R} - \frac{\Delta H^{\ddagger}}{RT} \qquad (1\text{-}16)$$

In the Arrhenius equation, the activation E_a is a parameter revealing the temperature dependence of the rate constant and the Arrhenius pre-exponential term, A, would be the rate constant either at infinite temprature or in the abscence of an activation energy, when E_a = 0. Also, a relationship between temperature and the equilibrium constant (K_{eq}) and the standard enthalpy change (ΔH°) can be derived, given the following reversible reaction and the van't Hoff equation

$$\mathrm{A} \underset{k_d}{\overset{k_a}{\rightleftharpoons}} \mathrm{P}$$

$$d(ln\,K_{eq})/dT = \Delta H^{\circ}/RT^2$$

where $K_{eq} = (P)/(A) = k_a/k_d$ and the parentheses indicate activity. The van't Hoff equation can be rewritten as

$$\frac{d(ln\,k_a)}{dT} - \frac{d(ln\,k_d)}{dT} = \frac{\Delta H^{\circ}}{RT^2}$$

where

$$\frac{d(ln\,k_a)}{dT} = \frac{E_a}{RT^2} \quad \text{and} \quad \frac{d(ln\,k_d)}{dT} = \frac{E_d}{RT^2}$$

where k_a and k_d are the rate constants of adsorption and desorption, respectively and E_a and E_d are the activation energies for adsorption and desorption steps, respectively.[111] Therefore, the standard enthalpy change (ΔH°) can be drived as $\Delta H^{\circ} = E_a - E_d$. Actually, because the differential form of the Arrhenius equation is $\frac{d(ln\,k)}{dT} = \frac{E_a}{RT^2}$, the rate constant ($k$) is the result of adsorption and desorption at equilibirum, as indicated by Azizian when he derived the PFO reaction equation.[102]

The relationship of the rate constant with thermodynamic activation parameters (Gibbs energy, entropy, and enthalpy of activation) can be described by the Eyring equation which utilizes transition state theory (TST) or activated complex theory (ACT). This equation assumes the following: 1) the reactants and activated complex are in a rapid pre-equilibrium (equation 1-17) at the top of the energy barrier and 2) the rate of the product formation is directly proportional to the concentration of the activated complex and the intrinsic rate constnat ($k^{\ddagger}$) for its decomposition to the final product (equation 1-19).[112]

$$A + B \rightleftharpoons C^{\ddagger} \rightarrow P \qquad (1\text{-}17)$$

$$\frac{d[P]}{dt} = k[A][B] \qquad (1\text{-}18)$$

$$\frac{d[P]}{dt} = k^{\ddagger}[C^{\ddagger}] \qquad (1\text{-}19)$$

In a pre-equilibrium condition, the equilibrium constant of the activated complex

$$K^{\ddagger} = \frac{[C^{\ddagger}]}{[A][B]} \tag{1-20}$$

$$[C^{\ddagger}] = K^{\ddagger}[A][B] \tag{1-21}$$

and combining equations (1-18 to 1-20) yields equation (1-22)

$$k = k^{\ddagger}K^{\ddagger} \tag{1-22}$$

The intrinsic rate constant ($k^{\ddagger}$) for conversion of the activated complex to the product (*cf.* eqn 1-17) is associated with a vibration in the activated complex that makes it more like the products, thus driving it along the reaction coordinate toward the product channel. Therefore, the pathway of the activated complex over the transition state can be recognized by a vibrational mode because the activated complex has a duration no longer than that of a vibration. Conversely, not every oscillation assoicated with the frequency of vibration (v) will change the activated complex to product. This is why other atoms in the molecule may not be correctly arranged for a transition to the product, or becasue the rotational state of the molecule intervenes the conversion pathway to the product. TST holds this factor as the transmission coefficient (κ). It may be assumed that the rate of the route of the activated complex over the transition state to the product is proportional to the vibrational frequency of relevance (v) and the transmission coefficient (κ), which in most cases is near unity.[112]

$$k^{\ddagger} = \kappa v \tag{1-23}$$

Becasue the lifetime of the activated complex is relatively short, a Boltzmann distribution of states may not be defined, the equilibrium constant of the activation complex ($K^{\ddagger}$) is then derived using statistical mechnics, as described by equation (1-24),

$$K^{\ddagger} = (\frac{k_B T}{hv})K^{\ddagger'} \tag{1-24}$$

$K^{\ddagger'}$, k_B, h, v, and T are the new equilibrium constant of the activation complex which is equal to $exp(-\Delta G^{\ddagger}/RT)$, Boltzmann constant ($k_B$=1.38066 × 10^{-23} JK^{-1}), Plank's constant (h =6.62608 × 10^{-34} Js), vibrational frequency (v), and absolute temperature (T).[112] Substituting equations (1-23) and (1-24) into equation (1-22) yields the Eyring equation (1-25), which consists of the term $\kappa(\frac{k_B T}{h})$, which is near 10^{12} vibrations per second, and is similar to magnitude to the frequency of many bond vibrations, as well as the $K^{\ddagger'}$ term.

$$k = \kappa(\frac{k_B T}{h})K^{\ddagger'} \tag{1-25}$$

When considering the following thermodynamic terms of the activated complex at equilibrium,

$$\Delta G^{\ddagger} = -RTlnK^{\ddagger'} \text{ and } \Delta G^{\ddagger} = \Delta H^{\ddagger} - T\Delta S^{\ddagger}$$

the $K^{\ddagger'}$ is equal to $exp[(-\Delta H^{\ddagger}/RT) + (\Delta S^{\ddagger}/R)]$ and by assuming $\kappa = 1$, Eq. (1-25) gives equation (1-26), which is similar to equation (1-16) after dividing by T and taking natural logarithm both sides.

$$k = (\frac{k_B T}{h})e^{(\Delta S^{\ddagger}/R)}e^{(-\Delta H^{\ddagger}/RT)} \qquad (1\text{-}26)$$

Strictly speaking, the Arrhenius equation is applied to gas phase reactions becasue it orginates from collision theory of gas phase reactions, where entropy is not really involved in the equation. The Eyring equation can be applied to both gas and of condensed phase reactions. In the Eyring equation, the rate constant k is related to $\Delta G^{\ddagger}$ (free energy of activation) that consists of a $\Delta H^{\ddagger}$ (enthalpy term) and a $\Delta S^{\ddagger}$ (entropy term). Therefore, the Eyring equation relates the rate constant for a reaction and the entropy and enthalpy of activation, according to transition-state theory. Comparing equations (1-15) and (1-16), E_a is related to $\Delta H^{\ddagger}$ and the pre-exponential factor ($ln\ (A)$ to $\Delta S^{\ddagger}$). In a gaseous or condensed phase reaction, $E_a = \Delta H^{\ddagger} + RT$ and for a bimolecular reaction, $E_a = \Delta H^{\ddagger} + 2RT$. As a rule of thumb, lower values of E_a and $\Delta H^{\ddagger}$ result in a faster reaction rate, and vice versa.

The study of the temperature dependence of the rate constant provides information about the degree of "*structural order*" in the transition state.[113,114] Large negative values of $\Delta S^{\ddagger}$ does not favour reaction rates because the low values of $ln(A)$. In other words, the structure of the activated complex in the transition state is more ordered or rigid than that of the reactants in the ground state. This is normally true if the degrees of freedom (e.g., translation, rotation, and vibration) become frozen between the initial to the transition state. The reaction rate is correspondingly slow. However, positive values (or less negative values) of $\Delta S^{\ddagger}$ which means the favorable reaction parallels the high values of $ln(A)$. In this condition, the structure of the transition state is highly disordered compared to the ground state. All degrees of freedom (translational, rotational and vibrational) are involved for the conversion from the ground state to the transition state. Thus, the reaction proceeds fast.[115]

The Eyring equation is valid only if a single-step (unimolecular or bimolecular) reaction is operational; therefore multi-step adsorption processes may not be appropriate for defining the activation parameters ($E_a = \Delta H^{\ddagger} + RT$) and is valid for solution-based adsorption processes.

Activation parameters are used to account for experimental reaction rates, particularly for organic reactions in solution. They are encountered when relationships between equilibrium constants and rates of reaction are explored using correlation analysis. For example, $ln\ K$ (which is equal to$-\Delta G°/RT$) is plotted against $ln\ k$ (which is equal to$-\Delta G^{‡}/RT$)[116] and this correlation is linear in many cases and suggests that the rate constant increases as the reaction becomes thermodynamically more favorable. The linear correlation is referred to as a linear free energy relation (LFER) and confers the linear relationship between the activation free energy or reaction free energy change induced by a substituent and a parameter that describes the electron donating or electron withdrawing characteristics of the substituent.[117]

1.3.5.4 Surface complexation model (SCM)

Adsorption at the surface of crystalline solids such as magnetite and goethite are complicated because there are several types of functional groups with different tendencies to protonate and deprotonate.[118] Model which describe an iron oxide surface that assumes to have only a single type of amphoteric functional group, whereas; the type Fe-OH, surface can avoid this dilemma.

All SCMs share at least four basic assumptions.[119] Firstly, it is assumed that mineral surfaces can consider flat planes of surface hydroxyl sites and that equations can be written to describe reactions at these specific sites. For example, a surface (S) which involves protonation and deprotonation may be described by equation (1-27) and (1-28). The subscript s in H_s^+denotes the concentration of aqueous H^+ at the mineral-water interface, which is generally not equivalent to the bulk concentration of H^+ due to electric field effects at the surface.

$$SOH_{(s)} + H^+_{s(aq)} \rightleftharpoons SOH^+_{2(s)} \tag{1-27}$$

$$SOH_{(s)} \rightleftharpoons SO^-_{(s)} + H^+_{s(aq)} \tag{1-28}$$

Secondly, reactions at mineral surfaces may be described using the mass-balance equations at equilibrium and at fixed temperature. In other words, these reactions are assumed to be in a state of local equilibrium and the related mass-balance of the reaction in equation (1-27) is described by eqn (1-29).

$$K_{int} = \frac{\{SOH^+_{2(s)}\}}{\{SOH_{(s)}\}\{H^+_{s(aq)}\}} \tag{1-29}$$

The brackets ({ }) refers to the activity of the species and related examples of such mass-balance associated with protonation, deprotonation, and metal and ligand complexation reactions are shown in Table 1.12.[119]

Table 1.12 Examples of adsorption reactions at the mineral-water interface with accompanying mass-law expressions[119]

Surface reaction	Mass-balance equation	Equilibrium expression
Protonation	$SOH + H_s^+ \rightleftharpoons SOH_2^+$	$K_{int}^+ = \frac{\{SOH_2^+\}}{\{SOH\}\{H_s^+\}}$
Deprotonation	$SOH \rightleftharpoons SO^- + H_s^+$	$K_{int}^- = \frac{\{SO^-\}\{H_s^+\}}{\{SOH\}}$
Monodentate metal adsorption	$SOH + M_s^+ \rightleftharpoons SOM + H_s^+$	$K_{int}^{M,m} = \frac{\{SOM\}\{H_s^+\}}{\{SOH\}\{M_s^+\}}$
Bidentate metal adsorption	$2SOH + M_s^+ \rightleftharpoons (SO)_2M^- + 2H_s^+$	$K_{int}^{M,b} = \frac{\{(SO)_2M^-\}\{H_s^+\}^2}{\{SOH\}^2\{M_s^+\}}$
Monodentate ligand adsorption	$SOH + L_s^- \rightleftharpoons SOL^{-2} + H_s^+$	$K_{int}^{L,m} = \frac{\{SOL^{-2}\}\{H_s^+\}}{\{SOH\}\{L_s^-\}}$
Bidentate ligand adsorption	$2SOH + L_s^- \rightleftharpoons (SO)_2L^{-3} + 2H_s^+$	$K_{int}^{L,b} = \frac{\{(SO)_2L^{-3}\}\{H_s^+\}^2}{\{SOH\}^2\{L_s^-\}}$

Notes: (1) The subscript 's'denotes the concentration of aqueous H^+ at the mineral-water interface. (2) Brackets, { }, indicate the activity of the species. Because activity coefficients are typically assumed to equal the unity for surface bound species, mass-balance expressions are occasionally written in terms of the concentrations of surface species, rather than in terms of their activities. (3) +, -, *M*, *m*, *M*, *b*, *L*, *m*, and *L*, *b* denote protonation, deprotonation, monodentate-metal adsorption, bidenate-metal adsorption, monodentate-ligand adsorption, and bidentate-ligand adsorption respectively.

Thirdly, a variable charge at the mineral surface may result in chemical reactions at the surface. It was observed that minerals have zero surface charge at a particular pH, termed the pH_{PZC} (pH at the point of zero charge) or pH_{PPZC} (pH at the pristine point of zero charge) in which the electrolyte binding at the surface is negligible. The variable mineral surface charge due to reactions is commonly described by SCMs using an electric double layer model. Another charge called a ‘permanent’ charge may also be present at the surface, which arises from lattice imperfections as a result of isomorphous replacements within the lattice.[120] However, this charge will remain constant, unaffected by surface complexation reactions. In the electric double layer model, the charge at the surface is balanced by a ‘diffuse layer’ of counter ions in solution, near the charged mineral surface. The separation of charge between the surface layer and the ‘diffuse layer’ gives rise to an electric potential, P, which is a function of the distance, r, from the surface. In this description, adsorbed ions are assigned to the surface layer and electrolyte binding to the metal oxide surface are considered negligible. If the electrolyte (e.g., $NaClO_4$) binding is insignificant (or accurately symmetrical), protonated and deprotonated surface sites SOH_2^+ and SO^- are in balance at the pH_{pzc} which are then referred to as the pristine point of zero charge, pH_{ppzc}. However, when electrolyte binding is important and likely not symmetrical near the pH_{pzc}., zero net charge at the pH_{pzc} reflects charge balance for protonated and deprotonated surface sites by taking into account the formation of surface complexes (e.g., $SOH_2^+ - ClO_4^-$ and $SO^- - Na^+$).[118] The general relationship between the electric potential (P) and the distance (r) at the surface is generally developed as the constant capacitance model (CCM), the diffuse double layer model (DLM), and the triple layer model (TLM). Among these models, the CCM and the DLM are illustrated in Fig. 1.15.

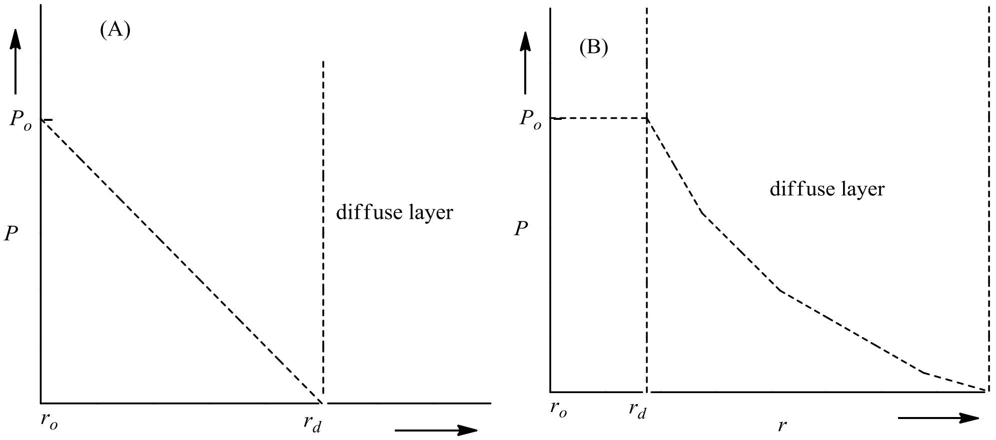

Figure 1.15 General form of the electric potential (P) versus distance (r) from the surface for the constant capacitance model (A) and the diffuse double layer model (B)

In case of the CCM, a specifically adsorbed plane of ions at the surface (r_o) forms a charge at the surface that is counter balanced by a single plane of counter ions at a distance r_d from the surface.

However, in the DLM, specific adsorption at the mineral surface plane is counterbalanced by a diffuse ion "swarm", rather than simply by a plane of counterions.[119]

Finally, the effect of surface charge on measured equilibrium constants K_{app} (or 'apparent' equilibrium constants) can be calculated considering an 'electrostatic' or 'Coulombic' correction factor of the form in eqn (1-30)

$$\exp\left(\frac{-zFP(r)}{RT}\right) \tag{1-30}$$

The intrinsic equilibrium constants (K_{int}) may then be extracted from experimental measurements using the form

$$K_{\mathrm{int}} = K_{\mathrm{app}} \exp\left(\frac{-zFP(r)}{\mathrm{R}T}\right) \tag{1-31}$$

where z is charge, F is the Faraday constant, $P(r)$ the electric potential as a function of the distance r from the surface, R the universal gas constant, and T the temperature (Kelvin).

Generally, the electrical double layer may comprise a layer of adsorbed ions and a diffuse double layer consisting of an ionic environment in which ions of one sign are in excess of their normal concentrations, whereas; those of the opposite charge are deficient.[121] This nonideal concentration of ions falls off rapidly as one recedes from the surface, the half-thickness of the charge density being seldom over 100 Å and usually much less.[121] In addition, there may exist a thin (often monomolecular) layer of neutral molecules at the interface, where the thermodynamic properties are affected by the presence of them regardless of their orientation.[121] The loci of the electronic centers of a layer of adsorbed ions, whether adsorbed by covalent bonds or van der Waals interactions, or both, are called the *inner* Helmholtz plane (IHP). The loci of the electronic centers of hydrated or solvated ions in contact with the mineral surface is called the *outer* Helmholtz plane (OHP).[121]

The diffuse double-layer model (DLM) and the triple-layer model (TLM) were used for describing the surface sorption processes. The TLM model may provide a better description of the surface complexation reaction and an understanding of the inner and outer surface complexation that occurs at the alpha (α; equivalent to the *inner* Helmholtz) and beta (β; equivalent to the *outer* Helmholtz) plane, respectively. The Stern-Grahame model of this electrical double layer with the surface potential is shown in Fig. 1.16,[119,122] where the adsorption of unhydrated ions at the IHP and hydrated ions occur at the OHP, together with the diffuse layer that extends into the bulk solution.[122]

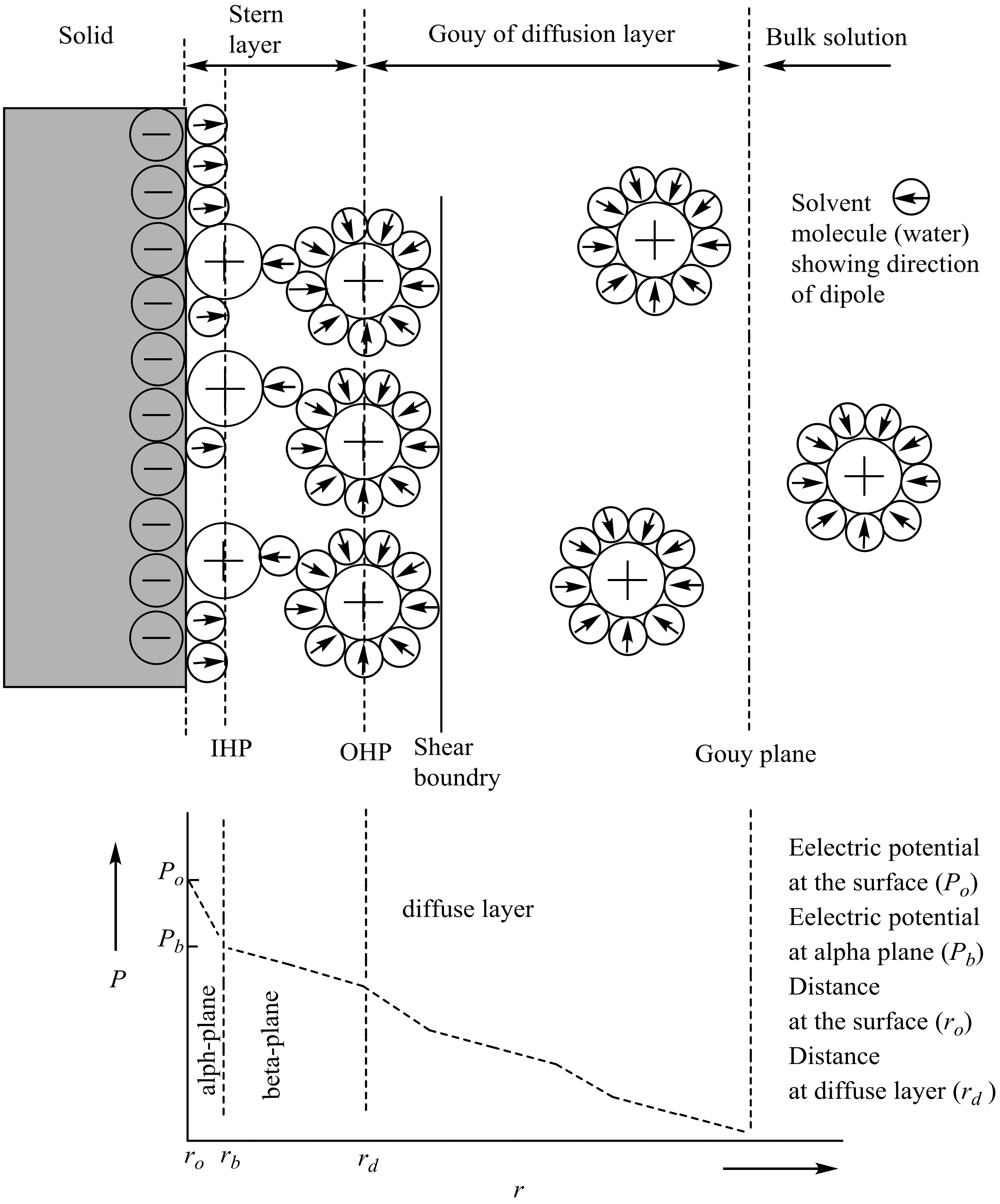

Figure 1.16 The Stern-Grahame model of the electrical triple layer with the surface potential. Adapted from References (119,122).

Aqueous solutions represent a chemical system consisting of a polar, high relative permittivity solvent (water), and chemical components that are dissolved in that solvent.[119] Dissolved elements in natural waters, called chemical species, may be present in many different forms such as cations, anions, or complexes. Ions in aqueous solution are solvated by a hydration shell of water molecules held by ion-dipole interactions with hydrated ions. Ions and other molecules may also coordinate (i.e. bond to each other) to form ion-pairs or aqueous complexes because a central metal atom is surrounded by anions or molecules called ligands.[119] The terms 'ion-pair' or 'outer-sphere complex' are used to explain bonding between ions that result from electrostatic interactions. This type of bonding involves the hydration shells of the cation, anion, or both are retained. Stronger associations called 'aqueous-complexes' or 'inner-sphere complexes' occur due to dative covalent interaction between a metal (a Lewis acid) and a ligand, and involves acceptance of electron pairs from a ligand (the Lewis base) to the *d*-orbital of the metal atom; where each ligand replaces one of the hydration shell water molecules.[119]

The structures of minerals are described by periodic three-dimensional (3D) crystal lattices. However, at the surface of a mineral, this periodic array is terminated and the presence of coordinatively unsaturated surface atoms project toward the solid-air or solid-water interface, leaving a surface with properties that may be quite different from those of the bulk 3-D structure. The surface atoms are coordinatively unsaturated and may have high surface energy compared to those in the bulk of the mineral structure because they are bonded to fewer atoms than they would be within the lattice framework. Surface cations are left with an excess of positive charge because bonds to anions have been disconnected in forming the surface, while coordinatively unsaturated anions are left with an excess of negative charge. Thus, coordinatively unsaturated cations and anions may undergo hydroxylation or protonation to form surface hydroxyl groups at the mineral interface.[119] The surface hydroxyl groups are amphoteric and may further react creating surface charges, depending on the pH of the solution. Therefore, isotherms or ion exchange model approaches are limited because they do not provide development of an electrical charge on mineral surfaces during the adsorption process. As well, structural information of the adsorbed product, may be overcome by unambiguously representing the chemical structure of the mineral-water interface according to SCMs. In addition, all cation-anion bond lengths in most minerals are not equal and of the variation in chemical structure is likely to lead to the presence of defects and changes in reactivity. [119]

Reactions at mineral surfaces are quantified by identifying both the types of surface sites present and the number of these sites per unit surface area (the site density).[119] Since surface sites may not be identical on different planes of a mineral, the overall type of site and their density depend on the crystal structure and morphology, including steric inhibition. Crystallographic studies of surface functional groups indicate that the mineral is reduced to form a smooth surface exactly parallel to cleavage or growth directions, and then the number and type of each surface site is accounted for and characterized.[119] To find the "ideal" truncations of various crystals, Koretsky *et al*. used calculated bond strengths and charges rather than considering arbitrary slices through the unit cell, and then used these ideal surfaces to estimate site types and densities.[123] In other words, by estimating the number of broken bonds at the surface that are equal to the number of reactive surface sites or by considering partial charges of coordinatively unsaturated atoms at the surface. This approach gave excellent agreement with available experimental results, as determined from site densities of tritium exchange experiments.[119] It is implicitly assumed that mineral surfaces are 'flat', in other words, that cleavage or growth planes are exactly parallel to a given direction. However, real mineral surfaces are not flat, as evidenced by statistical mechanic calculations where Burton *et al*. reported that stable mineral surfaces have complex topographies with spirals, steps and kinks.[124]

Chemical reactions at the mineral-water interface involves the uptake of species from aqueous solution, referred to as adsorption and absorption. Absorption is characterized by a chemical species that penetrates the crystal lattice. Adsorption is characterized by species that are taken up chemically and/or physically bound at the surface as a mono- or multi-layer at the mineral-water interface. In other words, adsorbates (or adsorbed chemical species) remain near the 2-D mineral-water interface for adsorption, as opposed to becoming dissolved within the 3-D solid lattice for absorption. Adsorbates may form various types of bonds with the mineral surface in the case of chemisorption. Physical adsorption (physisorption) of an adsorbate bound at the surface by noncovalent interactions. Electrostatic adsorption may also occur due to the attraction of opposite charges by the Coulomb's law ($F = (k \times q_1 \times q_2) / r^2$), where the attractive force (F) falls off with the square of the distance (r^2) between the two charged particles (q_1 and q_2). In chemical adsorption (chemisorption), much stronger dative or covalent ("chemical") bonds are created between the adsorbate and the surface sites. The term "non-specific" adsorption is often applied to physical or electrostatic adsorption, whereas the chemisorption is referred to as a "specific" type of adsorption.

It has been generally suggested that non-specifically bound species form "outer-sphere" complexes at the surface, where the hydration sphere is retained during adsorption. In contrast, specifically bound species form "inner-sphere" complexes at the surface, losing part or the entire hydration sphere in the adsorption process. Differentiation between inner- *vs*. outer-sphere complexes makes use of X-ray absorption spectroscopy.[125-127] The issue of whether a particular species is specifically adsorbed as an inner-sphere complex or non-specifically adsorbed as an outer-sphere complex is critical in terms of the structure and reactivity of the adsorbed species. For example, outer-sphere complexation has a negligible effect on the electron density distribution of the adsorbed species, as compared to the aqueous complex. Therefore, the reactivity of such bound species is apt to be comparable to the unbound aqueous species. On the other hand, inner-sphere complexation leads to considerable alterations in the electron density distribution in structure, which may lead to significant variation in reactivity.

SCMs are better than empirical models of adsorption since it introduces the 'intrinsic' equilibrium constants (K_{int}), which are more system-independent than those derived from empirical models.[119] Values of K_{int} rely on the characteristics of the adsorbent and the adsorbate (some models depend on ionic strength), but do not change by with pH, concentration of adsorbate or the solution composition.[119]

Most applications of SCMs are based on the assumption that surface hydroxyl groups for a given mineral are completely homogeneous using a single-site model. However, even for relatively simple oxide minerals, many types of surface hydroxyl groups may be present on a single plane of the mineral and their reactivities are likely to differ. In single-site surface complexation models, differences in surface hydroxyl site reactivities are averaged into the equilibrium constants. This treatment limits the applicability of such constants to minerals having similar morphology and surface composition.[120]

At present, a number of empirical models of surface adsorption such as distribution coefficient, ion exchange, Langmuir, Freundlich, and Sips isotherm models, including various SCMs are widely used. The use of empirical models to field-scale systems requires verification in the laboratory prior to being applied to a system of interest. They cannot be directly extrapolated beyond experimental conditions employed such as temperature, pressure, pH, ionic strength, oxidation-reduction state, and electrolyte composition. SCMs represent an advantage over empirical models since the calculations are applicable over a wide range of solution composition. This is valid because SCMs account for changes in surface electrical properties and the structure of the adsorbed species.

1.3.5.5 Error functions

To evaluate the goodness of fit of a kinetic model to experimental data, the linearization method has been primarily used because of its simplicity and usefulness. The linearization of nonlinear experimental data introduces problems with data fitting because data are improperly weighted. The fitting results from the same kinetic model are distorted relative to the use of nonlinear least squares fitting methods which provide better weighting at low and high concentrations. Moreover, a different axis label setting for the same model (e.g., the different linear plot types described in Table 1.11 for the PSO reaction) alters the regression outputs for the sorption parameters, thus influencing the accuracy, consistency, and validity of the kinetic models. Additionally, linearization methods assume that the given data set is linear and renders a straight-line relationship, illustrating the goodness of fit. Moreover, it is based on the assumption that the dispersed vertical points near the fitted line follow a Gaussian error distribution for every coordinate along the x-axis. This is hardly ever true or practical with kinetic studies as most of the kinetic models are non-linear due to their mechanistic nature, especially at dilute concentrations that approach sensitivity limitations of the measured experimental variable. The linear method considers error distribution only along the y-axis despite the corresponding x-axis obtained using the different parameters for the different plot types of linearized kinetic model for the same experimental data. Therefore, the linear method is not suitable for predicting the best-fit kinetic parameters for a particular experimental data set and unsuitable for providing a relevant understanding of the kinetics of the adsorption process. Nevertheless, employing the non-linear method reduces the disadvantages of linearization of experimental data. This is because the non-linear method accounts for the experimental equilibrium data and the isotherms on an appropriate scale which gives rise to better weighting of the error distribution.[128]

Several mathematically rigorous error functions for non-linear regression method are introduced in Table 1.13.[129]

Table 1.13 Error functions for non-linear regression treatment of the experimental adsorption data

Error function	**Abbreviation**	**Equation**
The sum of the squares of the errors or Sum square error	**ERRSQ or SEE**	$\sum_{i=1}^{n}(q_{e,meas}-q_{e,cal})_i^2$
Hybrid fractional error function	**HYBRID**	$\frac{100}{n-p}\sum_{i=1}^{n}\left[\frac{(q_{e,meas}-q_{e,cal})^2}{q_{e,meas}}\right]_i$
Coefficient of determination	$\mathbf{R^2}$	$1-\frac{\sum(q_{e,meas}-q_{e,cal})^2}{\sum(q_{e,meas}-q_{e,avg})^2}$
Marquardt's percent standard deviation	**MPSD**	$100\sqrt{\frac{1}{n-p}\sum_{i=1}^{n}(\frac{q_{e,meas}-q_{e,cal}}{q_{e,meas}})_i^2}$
Nonlinear chi-square test	χ^2	$\sum_{i=1}^{n}\frac{(q_{e,meas}-q_{e,cal})^2}{q_{e,cal}}$
Reduced chi-square	χ^2/**DoF**	$\sum_{i=1}^{n}\frac{(q_{e,meas}-q_{e,cal})^2}{n-p}$

Note: $q_{e,cal}$ (theoretically adsorbed amount); $q_{e,meas}$ (experimentally determined amount); p (number of parameters); n (number of data points); DoF (degree of freedom = n - p); $q_{e,avg}$ (experimentally determined mean amount)

The sum of the squares of the errors (ERRSQ) or sum square error (SEE) is the most commonly used error function. However, its major flaw is that at the higher range of adsorbate concentration, the magnitude and squares of the errors tend to increase, describing a better fit for the isotherm parameters.

Hybrid fractional error function (HYBRID) was developed to improve ERRSQ fit at low concentrations. Each ERRSQ value is divided by the experimental solid-phase concentration with a divisor included in the system as a term for the number of degrees of freedom (the number of data points minus the number of parameters within the isotherm equation).[130]

The coefficient of determination (R^2) represents the percentage of variability in the dependent variable (the variance about the mean) is employed to analyze the fitting degree of isotherm and kinetic models with the experimental data. The value may vary from 0 to 1, where a favourable R^2 value is closed to unity.

Marquardt's percent standard deviation (MPSD) is similar in some respects to a geometric mean error distribution modified according to the number of degrees of freedom of the system.[131]

The nonlinear chi-square test (χ^2) is a statistical tool required for the best fit of an adsorption system, obtained by judging the sum squares differences between the experimental and the calculated data, with each squared difference is divided by its corresponding value (calculated from the models). Small χ^2 value indicates its similarities while a larger number represents the variation of the experimental data.

Reduced chi-square (χ^2/DoF) is the χ^2divided by DoF where the degrees of freedom are (N-P). N and P denote number of data points and number of parameters in the fitting function that is being used. Small χ^2/DoF value indicates its similarities while a larger number represents the variation of the experimental data.[132]

The error involved in this research were measurement of instrumental error with Atomic Absorption Spectrophotometry (AAS) and UV-Vis spectrophotometry and fitting errors using Origin 7.5 SR4 software. The measurement errors were calculated using relative standard deviation (RSD, equation (1-32)) for AAS measurements and total error contribution (equations (1-34 to 1-36)) of measurements regarding the amount of an adsorbent and absorbance of an adsorbate concentration by differentiating the amount of adsorbate onto the adsorbent surface (equation (1-33)) for UV-vis measurements, respectively:

$$\%\mathrm{RSD} = \frac{\sigma}{\bar{x}} \times 100 \tag{1-32}$$

$$Q_e = \frac{(C_o - C_e) \times V}{m} \tag{1-33}$$

$$\Delta Q_e = 2\left|\frac{(C_o - C_e) \times V}{m^2} \times \Delta m\right| \tag{1-34}$$

$$\Delta Q_e = 2\left|\frac{V}{m} \times \Delta C_o\right| \tag{1-35}$$

$$\Delta Q_e = 2\left|\frac{V}{m} \times \Delta C_e\right| \tag{1-36}$$

σ is the standard deviation of the measured values, $\bar{x}$ is the mean values of the measured values, C_o is the initial concentration, C_e is the equilibrium concentration, Δm, ΔC_o, and ΔC_e are the standard errors associated with each measurement. The total error contribution (ΔQ_e) is the sum of the individual quantites in equations (1-34 ~ 1-36). Because there are positive and negative error contributions for each experimental data, the inclusion of the factor of two was taken before the absolute value of each quantity in equations (1-34 ~ 1-36). The uncertainties in absorbance for C_e and C_o were obtained from standard errors from the Beer's Law coefficients. The uncertainty in mass results from uncertainties in consecutive weighing on the electronic balance. If there are three steps to obtain an overall sample mass, the standard error is estimated as 3×10^{-4} g (assuming the use of a balance with a sensitivity of ±0.1 mg balance or 3×10^{-5} g for a balance with a sensitivity of ±0.01 mg).

The goodness of fit of an individual non-linear regression was obtained using the reduced chi-square (χ^2/DoF) as shown in Table 1.13. If χ^2/DoF goes to unity, the goodness-of-fit is considered ideal. The criterion of the "best-fit" for the pseudo-first and pseudo-second order reaction for sorption kinetic results was determined by the Root Mean Square Error (square root of the average sum of squares: RMSE) as shown in equation (1-37), where N is the number of experimental data points, $Q_{e,i}$ is the experimental value, and $Q_{c,i}$ is the calculated value by the respective sorption kinetic model. The model which gives the lower value of RMSE provides a better goodness-of-fit.

$$\text{RMSE} = \sqrt{\frac{1}{N}\sum_{i=1}^{N}(Q_{e,i} - Q_{c,i})^2} \qquad (1\text{-}37)$$

1.4 Organization and scope

This Ph.D. dissertation consists of several parts: 1) Literature review including the related chemistry of iron, selenium, arsenic, adsorption, and error function analysis, and 2) verbatim manuscripts that are either published or being considered for publication. To maintain the theme of this research, the adsorptive uptake of various selenium and arsenic species in solution was performed using iron oxide-activated carbon composites, and the respective single phase components (i.e. iron oxide and activated carbon).

This dissertation is composed of five chapters: Chapter 1 is the introductory and background material, Chapters 2-4 are the verbatim manuscripts, and Chapter 5 is the conclusion and suggestions for future work. The appendices contain raw data relevant to selected experimental studies that do not appear in the original manuscripts. A description of authorship and the title of manuscripts are described below.

Manuscript 1: Kwon, J. H.; Wilson, L. D.*; Sammynaiken, R.* Synthesis and Characterization of Magnetite and Activated Carbon Binary Composites. Synthetic Metals (SYNMET-D-13-00837), submitted December 2013.

Manuscript 2: Kwon, J. H.; Wilson, L. D.*; Sammynaiken, R. Sorptive uptake of selenium with magnetite and composite materials with activated carbon. Journal of Colloid and Interface Science (JCIS-14-56), submitted January 2014.

Manuscript 3: Kwon, J. H.; Wilson, L. D.*; Sammynaiken, R. Sorptive Uptake Studies of an Arylarsenical with Iron Oxide Composites on an Activated Carbon Support. Materials-47936, submitted December 2013.

There is a short summary of the work and a preamble describing the contributions of each author in each respective Chapter. In addition, a description of how each manuscript relates to the stated objectives of this Ph.D. dissertation has been described.

Chapter 1 is an introduction and overview of the entire Ph.D. dissertation and describes how the overall objectives were pursued in a systematic fashion, and how each hypothesis contributed to the overall goals of this dissertation.

Chapter 2 describes that selenium and arsenic have variable adsorption affinity onto the surface of magnetite (iron oxide) and goethite (iron oxyhydrate) in aqueous solution. The sorptive properties of the materials related to the synthetic strategy and were further supported by the characterization of these minerals as novel adsorbents in Manuscript 1. In addition, composite materials comprised of magnetite and activated carbon are anticipated to have reduced Fe leaching from the magnetite crystal structure. This hypothesis was outlined by the research concerning the “Synthesis and Characterization of Magnetite Composites with Activated Carbon Using a Novel Adsorbent." The iron leaching effect was described in detail in Chapter 3 where it was shown that leaching was attenuated at low temperatures. Greater leaching occurred above room temperature conditions due to the increased thermal breakdown of magnetite particles in the pores or on the surface of activated carbon.

Chapter 3 describes the sorption properties of the composite materials and their respective components (described in Manuscript 2) for the removal of selenium in aqueous solution. The adsorptive properties were evaluated by comparing the adsorption of selenium with magnetite, magnetite composites, activated carbon, and goethite through adsorption kinetics and at equilibrium conditions. Adsorbents such as magnetite, goethite, magnetite composites with activated carbon, and activated carbon were compared from their sorption parameters for adsorptive removal of selenium species in aqueous solution. A novel "*in situ*" kinetic set-up for this experiment was developed using a non-magnetic stirrer device with a semi-permeable filtration barrier. The analytical measurement of selenium uptake was achieved using atomic absorption spectrophotometry with hydride generation.

Chapter 4 presents a systematic study of the sorptive materials and their respective components with an aryl arsenical in aqueous solution. It was shown that the development of a sorbent with suitable surface functional groups for uptake of such species in solution was possible by simple modification of the surface of activated carbon described in Manuscript 2. Adsorbents such as magnetite, goethite, magnetite composites with activated carbon, and activated carbon were used for the removal of an arylarsenical (roxarsone) in aqueous solution. To control the speciation of roxarsone, a consecutive solution treatment for adsorbate/adsorbent system using Millipore water in equilibrium with phosphate buffer for UV-vis absorbance measurement was used for quantitative analysis. A novel one-pot kinetic experiment using a non-magnetic stirrer and a dialysis-based tubing filter was designed and applied to obtain kinetic data. The method offers several advantages over conventional batch kinetic experiments.

Chapter 5 summarizes the conclusions and future work, followed by Appendices of selected experimental data and results.

1.5 Overview of removal method of Se and As in aqueous solution

Since Se and As species are considered as important environmental toxins, various adsorbents for removing them in aqueous solution have been developed. Removal of selenium and arsenic species in aqueous solution has been accomplished by physical, chemical, and biological treatments. As shown in Table 1.14, these methods are well known for their technologies and operations and compared in terms of the removal method, and the corresponding advantages/and disadvantages. Although adsorption methods are typically physical in nature if one neglects chemisorption processes, , the unique binding affinity and availability of binding sites of the adsorbent materials to Se/As species via synthetic engineeering enables specialized advantages as a treatment method.

Coupled metals (Fe/Cu and Fe/Ni) have used an electrochemical reaction between the anode (Fe) and the cathode (Cu and Ni), resulting in Se and As deposits on the surface of the cathode.[133] However, there are leaching of particles in this method. Binary metals layered double hydroxides have relatively high anion exchange capabilities.[134] Sorption onto biogenic metal oxides have been accomplished using iron and manganese-oxidizing bacteria (*Gallionella ferruginea* and *Leptothrixochracea*).[135] These bacteria can oxidize As(III) to As(V) by dissolved oxygen and metal oxides adsorbs arsenic species. Iron coated granular activated carbon have used $FeCl_3$ for removing oxyanions.[136] Ferric chloride forms ferric hydroxide in an acidic solution that can adsorb oxyanions. Aluminum oxide/iron-coated materials can remove oxyanions by coordinating Se/As species into the modified surface of sand or quartz oxide.[137-139] Rice husk was used to prepare a biochar by sulfuric acid that can reduce selenite to elemental selenium on the surface of rice husk by forming -COOH and -OH groups onto the rice husk.[140] Multi-walled carbon nanotubes was used to remove roxarsone by π- π electron-donor-acceptor (EDA) interaction.[141] Chitosan-surface functionalized polymer with glutaraldehyde was used removing roxarsone by forming H-bonding interactions.[142]

Various iron oxide composites with different matrices such as activated carbon,[143-146] chitosan,[147] graphene,[148,149] polyaniline,[150] cellulose/AC,[151] metal oxide,[152] and silver/AC,[153] and zeolite[154] have been reported. These composites may be used as multi-purpose adsorbents which can increase the sorptive uptake properties by providing favourable adsorptive interactions for Se/As species, as follows: surface complexation with iron oxide and iron oxyhydroxide, H-bonding with iron oxyhydroxide, chitosan, polyaniline, and cellulose, EDA interaction with activate carbon, graphene, and polyaniline. With regard to the properties of an adsorbent, the removal of Se/As species in aqueous solution depends on its surface area and surface reactivity, using high surface area with surface reactivity may be critical. Considering these chemical interactions, composites of iron oxyhydroxide (e.g., goethite) with a strong matrix such as activated carbon may provide excellent uptake capacities of Se/As species due to the highly favoured complexation interactions at the adsorbent surface such as, H-bonding and EDA.

Table 1.14 Comparison of removal methods of Se and As species in aqueous solution

Methods	Removal by	Descriptions	Advantages	Disadvantages	References
Physical	Reverse Osmosis	Using a semi-permeable membrane for screening Se/As species out of wastewaters that is pumped by high pressure	• Dependable and well understood process	• Membrane fouling • Pre-treatment • Brine disposal • High operating and managing cost and technical complexity	8,17
	Nanofiltration	Using membrane filtration based on molecular size and ionic charge for rejecting As/Se species from wastewaters that is pumped by pressure	• Consistent and well understood process • Low operating pressures		8,17
	Ion Exchange	Reversible exchange of Se/As species from a process flow with more desirable ions of a similar charge adsorbed to a solid surface	• Selective removal of Se/As	• Backwashing and regeneration of resin • Waste disposal; • Sulfate competition • Failure to remove Selenate	8,17, 155, 156

Physical	Evaporation	Evaporation of pure water to concentrate Se/As species as a solid or in a brine stream	• Insignificant energy requirements • No pre-treatment requirements	• Large footprint • Dependent on solar radiation levels and temperature • Disposal of accumulated sediments • Pathway for Se/As exposure to wildlife	8,17
Chemical	Electro-coagulation	Formation and removal of As/Se species precipitates by electrolysis	• Effective removal of Se/As species • Low sludge production	• Costly • May require pre- and post-treatment • Leaching	8,17,157
	Se/As reduction using iron	Use of ZVI or Fe(II) for Se/As species reduction and subsequent precipitation	• Established technology to reduce Se/As concentrations	• High chemical consumption • Waste disposal • Temperature dependent	158

	Catalyzed cementation	Removal of Se species by cementation onto an iron surface and subsequent settling	- Successful removal of both selenate and selenite	- High chemical consumption - Waste disposal - Long-term stability of waste is unknown	8,17
Chemical	Photo-reduction	Reduction of SeO_4^{2-} and SeO_3^{2-} to Se^0 using UV light in the presence of a TiO_2 catalyst	- Minimal sludge production - Recoverable elemental selenium fraction	- High energy requirements - Production of toxic H_2Se gas	8,17
Biological	Algal volatilization	Evaporation of methylated Se by motivating algal growth by adding nutrients including carbon	- Low cost, *in situ* treatment process	- Difficulty motivating satisfactory algal growth - Failure to reduce Se below regulatory limits - Temperature dependent	8,17
	Active microbial reduction	Microbial Se reduction to Se^0 by the dynamic addition of	- Verified technology to meet regulatory	- Costly - Pre-treatment - Plugging by	8,17

		nutrients including carbon and energy	limits	Se Precipitates • Re-oxidation and mobilization of Se possible	
Biological	Passive microbial reduction	Passive flow system constructed with materials facilitating microbial reduction of Se without the dynamic addition of chemicals or energy	• Low capital and operation and management costs	• Questionable long term performance • Reoxidation and mobilization of Se possible • Temperature dependent	8,17
	In Situ microbial reduction	Microbial reduction of Se by the *in situ* addition of a carbon source to facilitate reducing conditions	• Low cost • *In situ* treatment of large volumes of water	• Generation of anoxic conditions to be toxic to wildlife • Questionable long term stability of Se precipitates	8,17
Adsorption	Ferrihydrite	Removal of Se by adsorption to amorphous	• EPA best offered verified technology	• High chemical consumption • Waste	

		ferrihydrite		disposal • Questionable long-term stability of waste • Effective with selenite only	
Adsorption	Activated carbon	Removal of Se/As by adsorption to amorphous activated carbon	• Excellent to organic As/Se species	• Insufficient removal of oxyanions • Waste disposal	This study
	Coupled metals	Formation and removal of Se/As precipitates by electrolysis	• Excellent to oxyanions • Magnetic	• Leaching	17, 133
	Iron coated granular activated carbon	Removal of Se/As by adsorption to amorphous activated carbon and surface complexation	• Excellent to oxyanions and organic As/Se species • Magnetic	• Waste disposal	159
	Iron oxide	Removal of Se/As by surface complexation	• Excellent to oxyanions • Magnetic	• Insufficient removal of organic Se/As species	This study, 160
	Iron oxyhydroxide	Removal of Se/As by suface complexation and H-bonding	• Excellent to oxyanions and organic Se/As species	• Non-magnetic	This study, 161,162

Adsorption	Polymer based retention	Removal of Se/As species by H-bonding	• Excellent to organic Se/As species	• Insufficient to inorganic Se/As species • Non-magnetic	142
	Biosorption using reactive Mn/Fe oxide	Removal of Se/As by surface complexation and H-bonding	• Excellent to inorganic Se/As species • Magnetic	• Insufficient to organic Se/As species	135

1.6 References

1. Fernández-Martínez, A.; Charlet, L. Selenium environmental cycling and bioavailability: a structural chemist point of view. *Rev. Environ. Sci. Biotechnol.*, **2009**, *8*, 81-110.

2. Barceloux, D. G. Selenium. *Clin. Toxicol.*, **1999**, *37*, 145-172.

3. http://www.sierraclub.bc.ca/media-centre/press-clips/no-new-elk-valley-coal-mines-until-selenium-issue-resolved-lake (accessed September 03, 2013)

4. http://ecowatch.com/2013/coal-mining-influences-epas-selenium-standards/ (accessed September 03, 2013)

5. Gilron, G. The selenium drinking water quality guideline in Canada: The case for a re-evaluation. *Integr. Environ. Assess. Manag.*, **2012**, *8*, 194-196.

6. http://www.medindia.net/patients/patientinfo/arsenic-poisoning.htm (accessed September 03, 2013)

7. Viet, H. P.; Con, H. T.; Ha, T. C.; Ha, V. H.; Berg, M.; Giger, W.; Schertenleib, R. Investigation of arsenic removal technologies for drinking water in Vietnam. In *ArsenicExposure and Health Effects V.*; Chappell, W. R., Abernathy, C. O., Calderon, R. L., Thomas, D. J., Eds.; Elsevier B.V.: Amsterdam, the Netherlands , 2003; pp 459-469.

8. Gallegos-Garcia, M.; Ramírez-Muñiz, K.; Song, S. Arsenic Removal from Water by Adsorption Using Iron Oxide Minerals as Adsorbents: A Review. *Miner. Process. Extr. M.*, **2012**, *33*, 301-315.

9. Jackson, B. P.; Seaman, J. C.; Bertsch, P. M. Fate of arsenic compounds in poultry litter upon land application. *Chemosphere*, **2006**, *65*, 2028-2034.

10. Makris, K. C.; Salazar, J.; Quazi, S.; Andra, S. S.; Sarkar, D.; Bach, S. B. H.; Datta, R. Controlling the fate of roxarsone and inorganic arsenic in poultry litter. *J. Environ. Qual.*, **2008**, *37*, 963-971.

11. Arai, Y.; Lanzirotti, A.; Sutton, S.; Davis, J. A.; Sparks, D. L. Arsenic speciation and reactivity in poultry litter. *Environ. Sci. Technol.*, **2003**, *37*, 4083-4090.

12. Church, C. D.; Kleinman, P. J. A.; Bryant, R. B.; Saporito, L. S.; Allen, A. L. Occurrence of arsenic and phosphorous in ditch flow from litter-amended soils and barn areas. *J. Environ. Qual.*, **2010**, *39*, 2080-2088.

13. Makris, K. C.; Quazi, M.; Punamiya, P.; Sarkar, D.; Datta, R, Fate of arsenic in swine waste from concentrated animal feeding operations. *J. Environ. Qual.*, **2008**, *37*, 1626-1633.

14. Stolz, J. F.; Perera, E.; Kilonzo, B.; Kail, B.; Crable, B.; Fisher, E.; Ranganathan, M.; Wormer, L.; Basu, P. Biotransformation of 3-Nitro-4-hydroxybenzene arsenic acid (roxarsone) and release of inorganic arsenic by *Clostridium* species**.** *Environ. Sci. Technol.*, **2007**, *41*, 818-823.

15. http://www.gazette.gc.ca/rp-pr/p2/2012/2012-03-14/html/sor-dors22-eng.html (accessed May 5, 2013)

16. Shaw, S. A.; Hendry, J. M.; Essilfie-Dughan, J.; Kotzer, T.; Wallschlager, D. Distribution, characterization, and geochemical controls of elements of concern in uranium mine tailings, Key Lake, Saskatchewan, Canada. *Appl. Geochem.,* **2011**, *26*, 2044-2056.

17. Golder Associates Inc. Literature review of treatment technologies to remove selenium from mining influenced water. **2009**, *08-1421-0034 Rev. 2*. pp 9-24.

18. Hayes, K.F., Roe, A.L., Brown, Jr. G.E., Hodgson, K.O., Lecknie, J.O., Parks, G.A., In situ X-ray absorption study of surface complexes: selenium oxyanions on α-FeOOH. *Science*, **1987**, *238*, 783-786.

19. Barceloux, D. G. Selenium. *Clin. Toxicol.*, **1999**, *37*, 145-172.

20. Sarquis, M.; Mickey, C. D. Selenium. Part 1: Its chemistry and occurrence. *J. Chem. Educ.*, **1980**, *57,* 886-889.

21. Dzul Erosa, M. S.; Höll, W. H.; Horst, J. Sorption of selenium species onto weakly basic anion exchangers: I. Equilibrium studies. *React. Funct. Polym.*, **2009**, *69*, 576-585.

22. Cutter, G. A. Species determination of selenium in natural waters. *Anal. Chim. Acta*, **1978**, *98*, 59-66.

23. Welch, A. H.; Lico, M. S.; Hughes, J. L. Arsenic in groundwater of the Western United States. *Ground Water*, **1988**, *26,* 333-347.

24. Cullen, W. R.; Reimer, K. J. Arsenic Speciation in the Environment. *Chem. Rev.* **1989**, *89*, 713-764.

25. Tallman, D. E.; Shaikh, A. U. Redox stability of inorganic arsenic(III) and arsenic(V) in aqueous solution. *Anal. Chem*., **1980**, *52*, 196-199.

26. Katsoyiannis, I. A.; Zouboulis, A. I. Application of biological processes for the removal of arsenic from groundwaters. *Water Res*., **2004**, *38*, 17-26.

27. Jackson, B. P.; Seaman, J. C.; Bertsch, P. M. Fate of arsenic compounds in poultry litter upon land application. *Chemosphere*, **2006**, *65,* 2028-2034.

28. Makris, K. C.; Salazar, J.; Quazi, S.; Andra, S. S.; Sarkar, D.; Bach, S. B. H.; Datta, R. Controlling the fate of roxarsone and inorganic arsenic in poultry litter. *J. Environ. Qual.*, **2008**, *37*, 963-971.

29. Arai, Y.; Lanzirotti, A.; Sutton, S.; Davis, J. A.; Sparks, D. L. Arsenic speciation and reactivity in poultry litter. *Environ. Sci. Technol*., **2003**, *37*, 4083-4090.

30. Church, C. D.; Kleinman, P. J. A.; Bryant, R. B.; Saporito, L. S.; Allen, A. L. Occurrence of arsenic and phosphorous in ditch flow from litter-amended soils and barn areas. *J. Environ. Qual*., **2010**, *39*, 2080-2088.

31. Makris, K. C.; Quazi, M.; Punamiya, P.; Sarkar, D.; Datta, R. Fate of arsenic in swine waste from concentrated animal feeding operations. *J. Environ. Qual*., **2008**, *37*, 1626-1633.

32. Stolz, J. F.; Perera, E.; Kilonzo, B.; Kail, B.; Crable, B.; Fisher, E.; Ranganathan, M.; Wormer, L.; Basu, P. Biotransformation of 3-Nitro-4-hydroxybenzene arsenic acid (roxarsone) and release of inorganic arsenic by *Clostridium* species. *Environ. Sci. Technol*., **2007**, *41*, 818-823.

33. Yu, X.; Tong, S.; Ge, M.; Zuo, J.; Cao, C.; Song, W. One-step synthesis of magnetic composites of cellulose@iron oxide nanoparticles for arsenic removal. *J. Mater. Chem. A*., **2013**, *1*, 959-965.

34. Silver, J. Chemistry of Iron, 1st ed.; Blackie Academic & Professional: Glasgow, 1993; p 5.

35. Silver, J. Chemistry of Iron, 1st ed.; Blackie Academic & Professional: Glasgow, 1993; p 6.

36. Silver, J. Chemistry of Iron, 1st ed.; Blackie Academic & Professional: Glasgow, 1993; p 6.

37. Silver, J. Chemistry of Iron, 1st ed.; Blackie Academic & Professional: Glasgow, 1993; pp 8-18.

38. Silver, J. Chemistry of Iron, 1st ed.; Blackie Academic & Professional: Glasgow, 1993; pp 10-11.

39. Pensak, D. A.; McKinney, R. J. Application of molecular orbital theory to transition-metal complexes. Fully optimisied geometries of first-row metal carbonyl compounds. *Inorg. Chem*., **1979**, *18*, 3407-3413.

40. Chin. H.; Smith, M. B.; Wilson, R. D.; Bau, R. Variations in molecular geometry along the isoelectronic series $[Co_2(CO)_8]$, $[FeCo(CO)_8]^-$, and $[Fe_2(CO)_8]^{2-}$. *J. Amer. Chem. Soc*., **1974**, *96*, 5285-5287.

41. Beagley, B.; Cruicksank, D. W. J.; Pinder, P. H.; Robiette, A. G.; Sheldrick, G. M. The molecular structure of $Fe(CO)_5$ in the gas phase. *Acta. Cryst.*, **1969**, *B25*, 737-744.

42. Griffith, W. P.; Lewis, J.; Wilkinson, G. Some nitric oxide complexes of iron and copper. *J. Chem. Soc.*, **1958**, 3993-3998.

43. Lauher, J. W.; Ibers, J. A. Structure of tetramethylammonium tetrachloroferrate(II) $[N(CH_3)_4]_2[FeCl_4]$. Comparison of iron(II) and iron(III) bond lengths in high-spin tetrahedral environments. *Inorg. Chem.*, **1975**, *14*, 348-352.

44. Buerger, H.; Wannagut, U. Silylamide derivatives of iron and cobalt. *Monatsh. Chem.*, **1963**, *94*, 1007-1012.

45. Bower, B. K.;Tennent, H. G. Transition metal bicyclo [2.2.1] hept-1-yls. *J. Amer. Chem. Soc.*, **1972**, *94*, 2512-2514.

46. Levason, W. A.; McAuliffe, C. A. Higher oxidation state chemistry of iron, cobalt, and nickel. *Coord. Chem. Rev*., **1974**, *12*, 151-184.

47. Audette, R. J.; Quail, J. W. Potassium, rubidium, cesium, and barium ferrate(VI). Preparations infrared spectra and magnetic susceptibilities. *Inorg. Chem.*, **1972**, *11*, 1904-1908.

48. Kopelev, N. S.; Perfil'ev, Yu. D.; Kiselev, Yu. M. The Mössbauer spectra of solutions of compounds of iron in higher oxidation states. *Russian J. Inorg. Chem.*, **1990**, *35*, 1022-1025.

49. Cornell, R. M.; Schwertmann, U. *The Iron Oxides: Structure, Properties, Reactions, Occurrences and Uses*, 2nd ed.; John Wiley & Sons: Weinheim, 2003; p 2.

50. Cornell, R. M.; Schwertmann, U. *The Iron Oxides: Structure, Properties, Reactions, Occurrences and Uses*, 2nd ed.; John Wiley & Sons: Weinheim, 2003; p 13.

51. Cornell, R. M.; Schwertmann, U. *The Iron Oxides: Structure, Properties, Reactions, Occurrences and Uses*, 2nd ed.; John Wiley & Sons: Weinheim, 2003; p 9.

52. Cornell, R. M.; Schwertmann, U. *The Iron Oxides: Structure, Properties, Reactions, Occurrences and Uses*, 2nd ed.; John Wiley & Sons: Weinheim, 2003; p 10.

53. Cornell, R. M.; Schwertmann, U. *The Iron Oxides: Structure, Properties, Reactions, Occurrences and Uses*, 2nd ed.; John Wiley & Sons: Weinheim, 2003; p 11.

54. Housecroft, C. E.; Sharpe, A. G. Inorganic chemistry, 2nd ed.; Pearson Educatkion Limited: New York, USA, 2005; p 558.

55. Cornell, R. M.; Schwertmann, U. *The Iron Oxides: Structure, Properties, Reactions, Occurrences and Uses*, 2nd ed.; John Wiley & Sons: Weinheim, 2003; p 32.

56. http://www.emg.tu-bs.de/forschung/material/magnetite_d.html (accessed September 14, 2013)

57. Yang, C.; Wu. J.; Hou, Y. Fe_3O_4 nanostructures: synthesis, growth mechanism, properties and applications. *Chem. Commun.*, **2011**, *47*, 5130-5141.

58. Liao, Z. M.; Li, Y. D.; Xu, J.; Zhang, J. M.; Xia, K.; Yu, D. P. Spin-filter effect in magnetite nanowire. *Nano Lett*., **2006**, *6*, 1087-1091.

59. Wang, Z. L. Transmission electron microscopy of shape-controlled nanocrystals and their assemblies. *J. Phys. Chem. B*, **2000**, *104*, 1153-1175.

60. Cornell, R. M.; Schwertmann, U. *The Iron Oxides: Structure, Properties, Reactions, Occurrences and Uses*, 2nd ed.; John Wiley & Sons: Weinheim, 2003; p 541.

61. Cornell, R. M.; Schwertmann, U. *The Iron Oxides: Structure, Properties, Reactions, Occurrences and Uses*, 2nd ed.; John Wiley & Sons: Weinheim, 2003; p 548.

62. Ong, B. H.; Devaraj, N. K.; Matsumoto, M.; Abdullah, M. H. Thermal stability of magnetite (Fe_3O_4) nanoparticles. *Mater. Res. Soc. Symp. Proc*., **2008**, *1118*, 56-62.

63. Tang, J.; Myers, M.; Bosnick, K. A.; Brus, L. E. Magnetite Fe_3O_4 Nanocrystals: Spectroscopic observation of aqueous oxidation kinetics. *J. Phys. Chem. B*, **2003**, *107*, 7501-7506.

64. Kinoshita, K. *Carbon: Electrical and Physicochemical Properties.* John Wiley & Sons: New York, USA, 1988, p. 10.

65. NORIT Americas Inc., *Understanding Activated Carbons*, Jul. **2005**, 00-010-TP

66. Do, D. D. Model for surface diffusion of ethane and propane in activated carbon. *Chem. Eng. Sci.*, **1996**, *51*, 4145-4158.

67. Kwon, J. H. Sorption studies of the surface modified activated carbon with β-cyclodextrin. M.Sc. Thesis, University of Saskatchewan, Saskatoon, 2007.

68. Sing, K. S. W.; Everett, D. H.; Haul, R. A. W.; Moscou, L.; Pierotti, R. A.; Rouquerol, J.; Siemieniewska, T. Reporting physisorption data for gas/solid systems with special reference to the determination of surface area and porosity. *Pure & Appl. Chem*., **1985**, *57*, 603-619.

69. Abe, I.; Fukuhara, T.; Kawasaki, N.; Hitomi, M.; Kera, Y. Characteristics of cyclodextrin adsorption onto activated carbons. *J. Colloid Interface Sci.*, **2000**, *229*, 615-619

70. http://www.prominentinc.com/literature-activated_carbon_terms.html (accessed September 20, 2013)

71. Fanning, P.E., Vannice, A., *Carbon*, **1993**, *31*, 721-730

72. Ruthven, D. M. Principles of adsorption and adsorption processes. John Wiley & Sons: New York, USA, 1984; pp. 7-8.

73. Ruthven, D. M. Principles of adsorption and adsorption processes. John Wiley & Sons: New York, USA, 1984; p 29.

74. Ruthven, D. M. Principles of adsorption and adsorption processes. John Wiley & Sons: New York, USA, 1984; p 30.

75. Zettlemoyer, A. C. Modern techniques for investigating interactions with surfaces. *Chem. Rev*., **1959**, *59*, 937-981.

76. Laszlo, K.; Podkoscielny, P.; Dabrowski, A. Heterogeneity of activated carbons with different surface chemistry in adsorption of phenol from aqueous solutions. *Appl. Surf. Sci.*, **2006**, *252*, 5752-5762.

77. http://www.fhi-berlin.mpg.de/acnew/department/pages/teaching/pages/teaching__wintersemester__2010_2011/klaus_christmann__adsorption__101105.pdf (accessed on September 22, 2013)

78. Freundlich, H. M. F. Over the adsorption in solution. *J. Phys. Chem*. **1906**, *57*, 385-471.

79. Langmuir, I. The constitution and fundamental properties of solids and liquids. *J. Am. Chem. Soc.*, **1916**, *38*, 2221-2295.

80. Bruanuer, S.; Emmett, P. H.; Teller, E. Adsorption of gases in multimolecular layers, *J. Am. Chem. Soc*., **1938**, *60*, 309-316.

81. Tempkin, M. I.; Pyzhev, V.; Kinetics of ammonia synthesis on promoted iron catalyst. *Acta Phys. Chim. USSR*., **1940**, *12*, 327-356.

82. Dubinin, M. M.; Radushkevich, L. V. The equation of the characteristic curve of the activated charcoal. *Proc. Acad. Sci. USSR Phys. Chem. Sect*., **1947**, *55*, 331-337.

83. Sips, R. On the structure of a catalyst surface. *J. Chem. Phys*., **1948**, *16*, 490-495.

84. Toth, J. State equations of the solid gas interface layer. *Acta Chem. Acad. Hung*., **1971**, *69*, 311-317.

85. Khan, A. R.; Ataullah, R.; Al-Haddad, A. Equilibrium adsorption studies of some aromatic pollutants from dilute aqueous solutions on activated carbon at different temperatures. *J. Colloid Interface Sci.*, **1997**, *194*, 154-165.

86. Redlich, O.; Peterson, D. L. A useful adsorption isotherm, *J. Phys. Chem.*, **1959**, *63*, 1024-1026.

87. Gimbert, F.; Crini, N. M.; Renault, F.; Badot, P. M.; Crini, G. Adsorption isotherm models for dye removal by cationized starch-based material in a single component system: Error analysis. *J. Hazard. Mater.*, **2008**, *157*, 34-46.

88. Hall, K. R.; Eagleton, L. C.; Acrivos, A.; Vermeulen, T. Pore and solid-diffusion kinetics in fixed-bed adsorption under constant-pattern conditions. *I & EC Fundamentals*. , **1966**, *5*, 212-223.

89. Aharoni, C.; Ungarish, M. Kinetics of activated chemisorption. Part 2. Theoretical models, *J. Chem. Soc. Faraday Trans.*, **1977**, *73*, 456-464.

90. Hobson, J. P. Physical adsorption isotherms extending from ultra high vacuum to vapor pressure. *J. Phys. Chem*., **1969**, *73*, 2720-2727.

91. Giles, C. H.; Smith, D.; Huitson, A. A general treatment and classification of the solute adsorption isotherm. I. Theoretical. *J. Colloid Interface. Sci.*, **1974**, *47*, 755-765.

92. Limousin, G.; Gaudet, J. P.; Charlet, L.; Szenknect, S.; Barthés, V.; Krimissa, M. (2007). Sorption isotherms: A review on physical bases, modeling and measurement. *Appl. Geochem*., **2007**, *22*, 249-275.

93. Toth, J. Thermo dynamical correctness of gas/solid adsorption isotherm equations. *J. Colloid Interface Sci.*, **1995**, *163*, 299-302.

94. Gregg, S. J.; Sing, K. S. Adsorption, Surface Area and Porosity, 2nd Ed.; Academic Press: New York, USA, 1982; p 4.

95. Brauner, S.; Deming, L. S.; Deming, E.; Teller, E. On a theory of the van der Waals adsorption of gases. *J. Am. Chem. Soc*., **1940**, *62*, 1723-1732.

96. Park, H. J.; Suh, M. P.; Stepwise and hysteretic sorption of N_2, O_2, CO_2, and H_2 gases in a porous metal–organic framework [$Zn_2(BPnDC)_2(bpy)$]. *Chem. Commun.*, **2010**, *46*, 610-612.

97. Thommes, M. Physical adsorption characterization of nanoporous materials. *Chemie Ingenieur Technik,* **2010**, *82*, 1059-1073.

98. Allen, T. Particle Size Measurement, 3rd Ed.; Chapman and Hall: New York, USA, 1981; pp. 523-525.

99. İnel, O.; Tümsek, F. The measurement of surface areas of some silicates by solution adsorption. *Turk. J. Chem*., **2000**, *24*, 9-19.

100. http://www.tcd.ie/CMA/misc/Surface_area_and_porosity.pdf (accessed on September 29, 2013)

101. Ismail, I. M. K. Cross-sectional areas of adsorbed N_2, Ar, Kr, and O_2 on carbons and fumed silicas at liquid nitrogen temperature. *Langmuir*, **1992**, *8*, 360-365.
102. Azizian, S. Kinetic models of sorption: A theoretical analysis. *J. Colloid Interf. Sci.*, **2004**, *276*, 47-52.
103. Sparks, D. L. Kinetics of soil chemical processes.; Academic Press: San Diego, USA, 1989; p 5.
104. Ho, Y. S.; McKay, G. The sorption of lead(II) ions on peat. *Water Res*., **1999**, *33*, 578-584.
105. Lagergren, S. About the theory of so-called adsorption of soluble substances. *Kungliga Svenska Vetenskapsakademiens Handlingar*, **1898**, *24*, 1-39.
106. Blanchard, G.; Maunaye, M.; Martin, G. Removal of heavy metals from waters by means of natural zeolites. *Water Res.*, **1984**, *18*, 1501-1507.
107. Ho, Y. S. Adsorption of heavy metals from waste streams by peat. Dissertation for the Doctoral Degree, University of Birmingham, Birmingham, 1995.
108. Lin, J.; Wang, L. Comparison between linear and non-linear forms of pseudo-first-order and pseudo-second-order adsorption kinetic models for the removal of methylene blue by activated carbon. *Front. Environ. Sci. Engin. China*, **2009**, *3,* 320-324.
109. Gerente, C.; Lee, V. K. C.; Le Cloirec, P.; McKay, G. Application of chitosan for the removal of metals from wastewaters by adsorption - Mechanisms and models review. *Crit. Rev. Env. Sci. Technol.*, **2007**, *37*, 41-127.
110. Alkan, M.; Demirbaş, Ö.; Doğan, M. 2007. Adsorption kinetics and thermodynamics of an anionic dye onto sepiolite. *Microporous Mesoporous Mater.*, **2007**, *101*, 388-396.
111. Sparks, D. L. Kinetics of soil chemical processes.; Academic Press: San Diego, USA, 1989; p 32.
112. Anslyn, E. V.; Dougherty, D. A. Modern Physical Organic Chemistry; University Science Books: Virginia, USA, 2006; pp. 365-366.
113. Tampouris, K.; Petrou, A. L. Thermodynamic parameters of geochemical processes. The free energy of activation rather than the activation energy is the controlling factor. *Hell. J. Geosci.,* **2010***, 45*, 299-306.
114. Petrou, A. L.; Economou-Eliopoulos, M. Platinum-group mineral formation: Evidence of an interchange process from the entropy of activation values. *Geochim. Cosmochim. Ac.*, **2009**, *73*, 5635-5645.

115. http://depa.fquim.unam.mx/amyd/archivero/Ecuacion_Eyring_7482.pdf (accessed on September 25, 2013)

116. Atkins, P.; De Paula, J. Physical Chemistry. 9th Ed.; W. H. Freeman and Company: New York, USA, 2010; p 849.

117. Anslyn, E. V.; Dougherty, D. A. Modern Physical Organic Chemistry; University Science Books: Virginia, USA, 2006; p 442.

118. Van Geen, A.; Robertson, A. P.; Leckie, J. O. Complexation of carbonate species at the goethite surface: Implications for adsorption of metal ions in natural waters. *Geochim. Cosmochim. Acta*, **1994**, *58*, 2073-2086.

119. Koretsky, C. The significance of surface complexation reactions in hydrologic systems: a geochemist's perspective. *J. Hydrology*., **2000**, *230*, 127-171.

120. Stumm, W. Chemistry of the solid-water interface: processes at the mineral-water and particle-water interface in natural systems. John Wiley & Sons: New York, USA, 1992; pp. 43-46.

121. Grahame, D. C. The electrical double layer and the theory of electrocapillarity. *Chem. Rev.* **1941**, *41*, 441-501.

122. Miettinen, T.; Ralston, J.; Fornasiero, D. The limits of fine particle flotation. *Miner. Eng.*, **2010**, *23*, 420-437.

123. Koretsky, C. M.; Sverjensky, D. A.; Sahai, N. A model of surface site types on oxide and silicate minerals based on crystal chemistry: implications for site types and densities, multi-site adsorption, surface infrared spectroscopy, and dissolution kinetics. *Am. J. Sci*., **1998**, *298*, 349-438.

124. Burton, W. K.; Cabrera, N.; Frank, F. C. The growth of crystals and the equilibrium structure of their surfaces. *Philos. Trans. R. Soc. London, Ser. A*, **1951**, *243*, 299-358.

125. Thompson, H. A.; Brown Jr., G. E. Parks, G. A. XAFS spectroscopic study of uranyl coordination in solids and aqueous solution. *Am. Mineral*., **1997**, *82*, 483-496.

126. Bargar, J. R.; Towle, S. N.; Brown Jr., G. E.; Parks, G. A. Outer-sphere Pb(II) adsorbed at specific surface sites on single crystal α-alumina. *Geochim. Cosmochim. Acta*, **1996**, *60*, 3541-3547.

127. O’Day, P. A.; Chisholm-Brause, C. J.; Towle, S. N.; Parks, G.; Brown Jr., G. E. X-ray absorption spectroscopy of Co(II) sorption complexes on quartz (a-SiO2) and rutile (TiO2). *Geochim. Cosmochim. Acta*, **1996**, *60*, 2515-2532.

128. Chowdhury, S.; Saha, P. Pseudo-second-order kinetic model for sorption of malachite green onto sea shell: Comparison of linear and non-linear methods. *Institute of Integrative Omics and Applied Biotechnology (IIOAB).*, **2010**, *1*, 3-7.

129. Foo, K. Y.; Hameed, B. H. Insights into the modeling of adsorption isotherm systems. *Chem. Eng. J.*, **2010**, *156*, 2-10.

130. Ng, J. C. Y.; Cheung, W. H.; McKay, G. Equilibrium studies of the sorption of Cu(II) ions onto chitosan. *J. Colloid Interface Sci.*, **2002**, *255*, 64-74.

131. Marquardt, D. W. An algorithm for least-squares estimation of nonlinear parameters, *J. Soc. Ind. Appl. Math.*, **1963**, *11*, 431- 441.

132. http://www.originlab.com/forum/topic.asp?TOPIC_ID=4058 (accessed on September 27, 2013)

133. Twidwell, L .G.; Hunag, H. H. An investigation to develop a galvanically enhanced cementation technology for removing oxyanions of arsenic and selenium from minewaste waters. *MWTP-213*, **2004**. Apr.

134. You, Y.; Vance, G. F.; Zhao, H. Selenium adsorption on Mg-Al and Zn-Al layered double hydroxides. *Appl. Clay Sci.*, **2001**, *20*, 13-25.

135. Katsoyiannis, I. A.; Zouboulis, A. I.; Jekel, M. Kinetics of bacterial As(III) oxidation and subsequent As(V) removal by sorption onto biogenic manganese oxides during groundwater treatment. *Ind. Eng. Chem. Res.*, **2004**, *43*, 486-493.

136. Zhang, N.; Lina, L. S.; Gang, D. Adsorptive selenite removal from water using iron-coated GAC adsorbents. *Water Res*., **2008**, *42*, 3809-3816.

137. Kuan, W. H.; Lo, S. L.; Wang, M. K.; Lin, C. F. Removal of Se(IV) and Se(VI) from water by aluminum-oxide-coated sand. *Water Res*., **1998**, *32*, 915-923.

138. Lo, S. L.; Chen, T. Y. Adsorption of Se(IV) and Se(V1) on an iron-coated sand from water. *Chemosphere*, **1997**, *35*, 919-930.

139. Chan, Y. T.; Kuan, W. H.; Chen, T. Y.; Wang. M. K. Adsorption mechanism of selenate and selenite on the binary oxide systems. *Water Res*., **2009**, *43*, 4412-4420.

140. El-Shafey, E. I. Sorption of Cd(II) and Se(IV) from aqueous solution using modified rice husk. *J. Hazard. Mater.*, **2007**, *147*, 546-555.

141. Hu, J.; Tong, Z.; Hu, Z.; Chen, G. W.; Chen, T. H. Adsorption of roxarsone from aqueous solution by multi-walled carbon nanotubes. *J. Colloid Interface. Sci*., **2012**, *377*, 355-361.

142. Poon, L.; Younus, S.; Wilson, L. D. Adsorption study of an organo-arsenical with chitosan-based sorbents. *J. Colloid Interface Sci*., **2014**, in press, DOI: 10.1016/j.jcis.2014.01.003

143. Kwon, J. H.; Wilson, L. D.*; Sammynaiken, R.* Synthesis and Characterization of Magnetite and Activated Carbon Binary Composites. Synthetic Metals (SYNMET-D-13-00837), **2014**, manuscript submitted for publication.

144. Kwon, J. H.; Wilson, L. D.*; Sammynaiken, R. Sorptive uptake of selenium with magnetite and composite materials with activated carbon. Journal of Colloid and Interface Science (JCIS-14-56), **2014**, manuscript submitted for publication.

145. Kwon, J. H.; Wilson, L. D.*; Sammynaiken, R. Sorptive Uptake Studies of an Arylarsenical with Iron Oxide Composites on an Activated Carbon Support. Materials-47936, **2014**, manuscript submitted for publication.

146. Castro, C. S.; Guerreiro, M. C.; Gonçalves, M.; Oliveira, L. C. A.; Anastácio, A. S. Activated carbon/iron oxide composites for the removal of atrazine from aqueous medium. *J. Hazard. Mater*., **2009**, *164*, 609-614.

147. Zhi, J.; Wang, Y.; Lu, Y.; Ma, J.; Luo, G. In situ preparation of magnetic chitosan/Fe_3O_4 composite nanoparticles in tiny pools of water-in-oil microemulsion. *React. Funct. Polym*. **2006**, *66*, 1552-1558

148. Wang, C.; Feng, C.; Gao, Y.; Ma, X.; Wu, Q.; Wang, J. Preparation of a graphene-based magnetic nanocomposite for the removal of an organic dye from aqueous solution. *Chem. Eng. J*. **2011**, *173*, 92-97.

149. Liu, M.; Chen, C.; Hu, J.; Wu, X.; Wang, X. Synthesis of magnetite/graphene oxidecomposite and application for cobalt(II) removal. *J. Phys. Chem. C*., **2011**, *115*, 25234-25240.

150. Wan, M.; Zhou, W.; Li, J. Composite of polyaniline containing iron oxides with nanometer size. *Synthetic. Met.*, **1996**, *78*, 27-31.

151. Zhu, H. Y.; Fu, Y. Q.; Jiang, R.; Jiang, J. H.; Xiao, L.; Zeng, G. M.; Zhao, S. L.; Wang, Y. Adsorption removal of congo red onto magnetic cellulose/Fe_3O_4/activated carbon composite

equilibrium, kinetic and thermodynamic studies. *Chem. Eng. J*. **2011**, *173*, 494-502.

152. Fan, H.; Xu, Q.; Guo, Y.; Cao, Y. Al_2O_3/Fe_2O_3 Mesoporous composite prepared with activated carbon template in supercritical carbon dioxide. *Ind. Eng. Chem. Res.* **2006**, *45*,5009-5012.

153. Valusová, E.; Vandzurová, A.; Pristas, P.; Antalík, M.; Javorský, P. Water treatment using activated carbon supporting silver and magnetite. *Water Sci. Technol*. **2012**, *66*, 2772-2778.66

154. Salah El-Din, T. A.; Elzatahry, A. A.; Aldhayan, D. M.; Al-Enizi, A. M.; Al-Deyab, S. S. Synthesis and characterization of magnetite zeolite nano composite. *Int. J. Electrochem. Sci.*, **2011**, *6*, 6177-6183.

155. Zhang, X.; Jiang, K.; Tian, Z.; Huang, W.; Zhao, L. Removal of arsenic in water by an ion-exchange fiber with amino groups. *J. Appl. Polym. Sci.*, **2008**, *110*, 3934 -3940.

156. Masotti, A. Arsenic: Sources, environmental impact, toxicity and human health – a medical geology persepective. Nova Publishers: New York, USA, 2013; pp 269, 270, 275, 306.

157. Sánchez, J. A.; Rivas, B. L.; Pooley, S. A.; Basaez, L.; Pereira, E.; Pignot-Paintrand, I.; Bucher, C.; Royal, G.; Saint-Aman, E.; Moutet, J-C. Electrocatalytic oxidation of As(III) to As(V) using noble metal–polymer nanocomposites. *Electrochim. Acta*, **2010**, *55*, 4876-4882.

158. Lackovic, J. A.; Nikolaidis, N. P.; Dobbs, G. Inorganic arsenic removal by zero-valent iron. *Environ. Eng. Sci.*, **2000**, *17*, 29-39.

159. Zhang, N.; Lina, L. S.; Gang, D. Adsorptive selenite removal from water using iron-coated GAC adsorbents. *Water Res*., **2008**, *42*, 3809-3816.

160. Gonzalez, C. M.; Hernandez, J.; Peralta-Videa, J. R.; Botez, C. E.; Parsons, J. G.; Gardea-Torresdeya, J. L. Sorption kinetic study of selenite and selenate onto a high and low pressure aged iron oxide nanomaterial, *J. Hazard. Mater.*, **2012**, *211-212*, 138-145.

161. Sharrad, M. O. M.; Liu, H.; Fan, M. Evaluation of FeOOH performance on selenium reduction, *Sep. Purif. Technol.*, **2012**, *84*, 29-34.

162. Chen, W. U; Huang, C. H. Surface adsorption of organoarsenic roxarsone and arsanilic acid on iron and aluminum oxides. *J. Hazard. Mater.*, **2012**, *227- 228*, 378- 385.

CHAPTER 2

MANUSCRIPT 1

Description

The synthesis and characterization of magnetite, magnetite composites with activated carbon, and goethite is described in this Chapter, which is a verbatim copy of a manuscript submitted for publication to a peer-reviewed journal entitled Synthetic Metals. The mole ratio of Fe^{3+} to Fe^{2+} was maintained as 2:1 in all synthesis. The final solution mixtures were controlled pH 10-11, 50-60 °C and under oxygen free conditions. With regard to prepared goethite, it was carried out by employing a high OH^{-}/Fe^{3+} molar ratio (5:1) at 30 °C for 24 h with vigorous stirring.

Authors' Contribution

The conception of the idea of magnetite impregnation into activated carbon was proposed by R. Sammynaiken. I did the literature review for the appropriate methodology for preparing fine particle size of magnetite. Synthesis and characterization of magnetite, magnetite composites with activated carbon, and goethite was performed by me. I drafted the first draft of the manuscript with subsequent editing by Lee. D. Wilson and R. Sammynaiken. My mentors guided me throughout the research process to complete experimental work.

Relation of Chapter 2 (Manuscript 1) to the overall objectives of this project

This work relates to the research hypothesis as described in the section 1.2 in Chapter 1. The development of carbon-based materials was the cornerstone of my research that enabled further studies of adsorption in solution. The appropriate methodology for preparing fine particle sizes of magnetite was developed.

Graphical Abstract

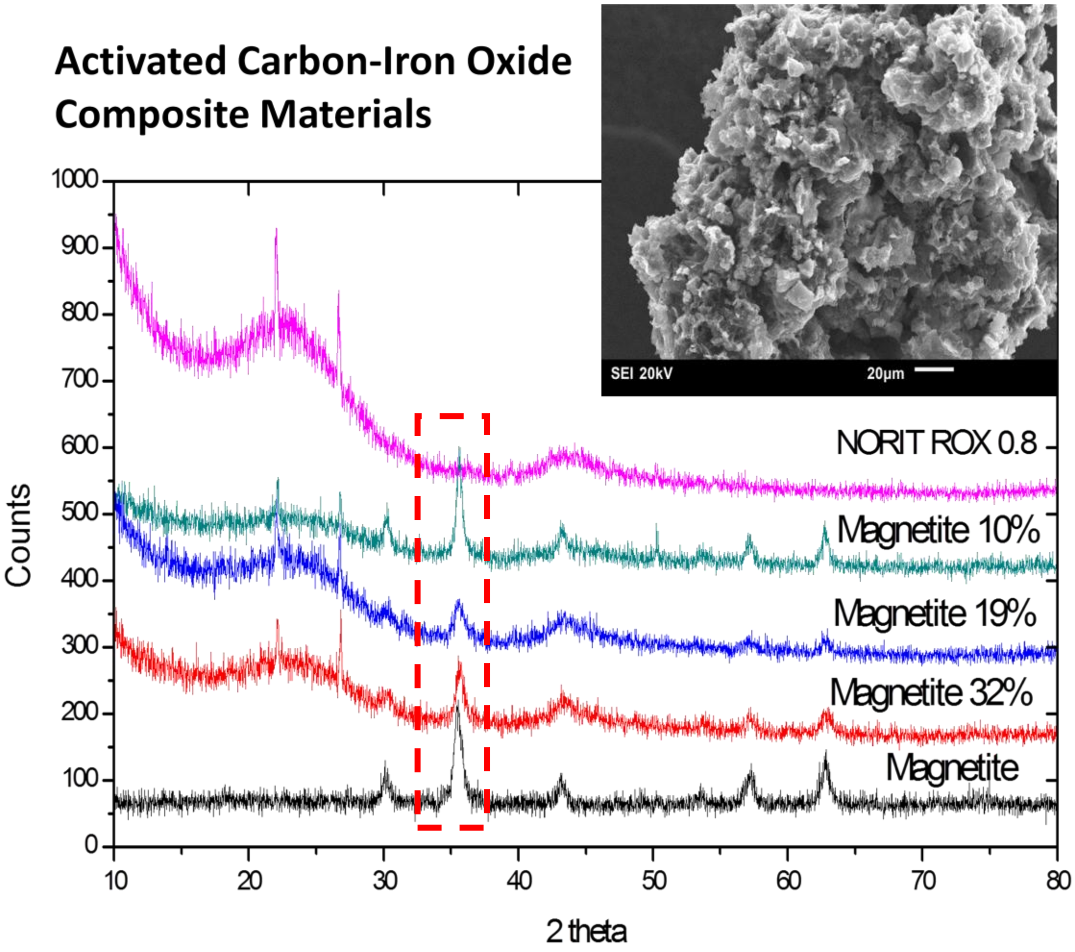

Research Highlights

- Composite materials were prepared using activated carbon and co-precipitation of Fe^{2+}/Fe^{3+}
- Composite materials were characterized using multiple methods
- Composites display variable textural properties, surface chemistry, and reduced Fe leaching

2. SYNTHESIS AND CHARACTERIZATION OF MAGNETITE AND ACTIVATED CARBON BINARY COMPOSITES

Jae H. Kwon[1], Lee D. Wilson[2*], R. Sammynaiken[3*]

[1] University of Saskatchewan, 110 Science Place, Saskatoon, SK S7N 5C9 Canada; E-Mail: jak878@mail.usask.ca

[2*] University of Saskatchewan, 110 Science Place, Saskatoon, SK S7N 5C9 Canada; E-Mail: lee.wilson@usask.ca

[3*] Saskatchewan Structural Science Centre, University of Saskatchewan, 110 Science Place, Saskatoon, SK S7N 5C9 Canada; E-Mail: r.sammynaiken@usask.ca

***** Author to whom correspondence should be addressed; E-Mail: lee.wilson@usask.ca; Tel.: +1-306-966-2961; Fax: +1-306-966-4730

Received: / Accepted: / Published:

2.1 Abstract

Magnetite and its composite materials with activated carbon were prepared using a co-precipitation method with Fe^{2+}/Fe^{3+} at 60 °C under anaerobic conditions. Iron oxyhydroxide (goethite, α-FeOOH) was synthesized at the 5/1 OH^-/Fe^{3+} molar ratio. Characterization of these composite materials and goethite were obtained using Powder X-ray Diffraction (PXRD), Raman spectroscopy, Diffuse Reflectance Infra-red Fourier Transform Spectroscopy (DRIFTS), Thermogravimetric analysis (TGA), Scanning Electron Microscopy (SEM), Transmission Electron Microscopy (TEM), and N_2 adsorption-desorption analysis. Inhomogeneous growth of magnetite in the activated carbon was revealed by electron microscope images. N_2 adsorption-desorption isotherm analysis and the total Fe content in the composites were determined. Composite materials of activated carbon and iron oxide possessed modified pore structure and oleophilicity relative to the starting materials, activated carbon and iron oxide. Iron oxide-activated carbon composites may have application as sorbents for oxyanion and cation species in wastewater treatment.

Keywords: magnetite; goethite; activated carbon; PXRD; synthesis; characterization

2.2. Introduction

Iron oxides exist in 16 different identified forms of oxides, hydroxides, and oxyhydroxides.[1] Among them, magnetite (Fe_3O_4), maghemite (γ-Fe_2O_3), and hematite (α-Fe_2O_3) have been studied actively by researchers because they are the principal forms used in industrial applications such as the iron and steel industry for ores, paints for pigments, industrial processes for catalysts, and the recording industry for magnetic pigments.[2] As pigments, iron oxides exhibit different colors as evidenced in their different forms. For example, hematite-based pigments are red, maghemite-based pigments are brown, and magnetite-based pigments are black.[2] Therefore, magnetite is also used in the formulation of toner and ink for printers, photocopiers, facsimile machines, and in some security inks.[2] Hematite and magnetite are used for the Haber process, the Fischer-Tropsch synthesis, and water-gas-shift reaction as catalysts.[1] In the media recording areas, magnetite and maghemite are the major sources of magnetic pigment due to their high magnetic property. However, hematite is rarely used in these areas because of its weak ferromagnetic nature.[2]

Another very important aspect of iron oxide is its particle size for the aforementioned applications. Surface area and particle size are is interrelated as important properties for catalytic activity. The magnetic behavior of iron oxide depends on size[3] and superparamagnetic when the particle size is smaller than 10 nm.[4,5] pH and ionic strength also affect the particle size of iron oxide. Higher pH and ionic strength tends to favour smaller particle size and uniform size distribution[6,7] which attributes to the stable thermodynamic properties of the crystals arising by reducing the amount of super-saturation of iron oxide small crystals. However, at a lower pH and ionic strength, the particles with lower zeta-potential still continue to grow during the ageing phase associated with Ostwald ripening, resulting in the formation of larger particles.[7]

The most common method to prepare magnetite was reported by Massart.[8] Different methods were developed by addition of base to an aqueous solution of ferrous (Fe^{2+}) and ferric (Fe^{3+}) ions in a 1:2 stoichiometry in an oxygen free environment. It is important to have an oxygen free environment during the synthesis; otherwise magnetite can be further oxidized to ferric hydroxide in the reaction medium. Synthesis of magnetite can be achieved by various processes, such as thermal decomposition,[9] microemulsion,[10] hydrothermal,[11] and co-precipitation[13,14] methods. Among these methods, the co-precipitation method has been regarded as an eco-friendly way to synthesize magnetite nanoparticles from a basic aqueous iron salt (Fe^{2+} and Fe^{3+}) solution under anaerobic conditions below 100 °C.[15,16]

There is continued interest in the application of iron oxide-based adsorbents and their composites due to the relatively high affinity of such materials to oxyanions.[17,18] For example, the removal of metal cations and their oxyanions from wastewater employ iron oxides and oxyhydroxides such as magnetite, Fe_3O_4; maghemite, γ-Fe_2O_3; hematite, α-Fe_2O_3; goethite, α-FeOOH, and other oxides of iron. Such iron oxide adsorbents were used for decades due to their low cost and high affinity[18] for oxyanion species attributed to the favourable Lewis acid (metal)-Lewis base (pi) interactions involved in surface complexation processes.

Goethite (α-FeOOH) as a one of iron oxyhydroxides does not show any magnetic properties at ambient temperature. However, it is one of the magnetic carriers and is characterized by a weak capacity to provide a thermoremanent magnetization (TRM) acquired by cooling from a Néel temperature of 120°C in the presence of a magnetic field.[19] TRM is believed to originate from the presence of anti-ferromagnetism in goethite with the Néel temperature, resulting from the presence of unpaired spins of electrons with neighboring spins due to the presence of small grain size, or imperfections and impurities in goethite.[19] As magnetite contains iron and oxygen atoms in the crystal structure, goethite has the same elements as well as hydroxyl groups, which enable surprising results in adsorptive processes.

As a carbon-based nanomaterial, activated carbon (AC) is often characterized by a relatively high surface area and high porosity. Its structure[20] consists primarily of sp^2 graphitic domains comprised of 3 to 4 parallel hexagonal carbon ring layers separated by 3.44 - 3.65 Å interlayer void spacing. This interlayer spacing is approximately 10 nm in length and is to some extent larger than that (3.35 Å) of graphite. A common structural motif observed in activated carbon are the microcrystalline (amorphous) graphitic-like sheets ("*basal planes*") which are randomly cross-linked, unevenly stacked, and surrounded by a number of unpaired electrons due to the presence of surface defects.[21] These structural features make AC highly porous in terms of its pore width (pw): *micro*- (pw < 2 nm), *meso*- (2 nm < pw < 50 nm), and *macro*-pores (50 nm < pw); useful for various applications in catalysis and adsorption for diverse suitably sized adsorbates. Moreover, AC contains various heteroatoms (e.g., O, N, P, and S). However, covalently bound oxygen atoms or physisorbed molecular oxygen is the major heteroatom species which affects the physiochemical properties of AC.

Regarding iron oxide composites, various materials such as chitosan,[22] graphene,[23] polyaniline,[24] AC,[25] cellulose/AC,[26] metal oxide,[27] and silver/AC[28] have been used in its preparation. However, a sole magnetite composite with AC using a co-precipitation method of Fe^{3+}/Fe^{2+} ions in water has not yet been reported to the best of our knowledge. In addition, iron oxide composites with AC may give rise to some advantages in wastewater treatment; *i*) providing enhanced adsorptive properties selective removal of waterborne pollutants such as oxyanions and cations due to the oleophilicity of activated carbon and chemical affinity of iron oxide, *ii*) iron leaching may be attenuated by forming composites, and *iii*) the magnetic susceptibility of iron oxides enables facile separation of the sorbent phase from wastewater using an electromagnetic field. In this study, activated carbon supported composites and non-supported magnetite and goethite were prepared and characterized. Evaluation of the structure and physicochemical properties of such composites was made using various spectroscopic methods with an assessment of their potential application as adsorbent materials.

2.3. Experimental Section

2.3.1. Synthesis of magnetite

Magnetite was prepared by co-precipitation methods.[29] Briefly, 10 mL of 2.0 M $FeCl_2{\cdot}4H_2O$ (98 %; Alfa Aesar) solution was prepared (3.976 g $FeCl_2{\cdot}4H_2O$ in 2.0 M HCl). 10 mL of 1.0 M $FeCl_3{\cdot}6H_2O$ (98 %; Alfa Aesar) solution was prepared (2.703 g $FeCl_3{\cdot}6H_2O$ in 2.0 M HCl). In a 500 mL three-neck round bottom flask, 200 mL Millipore water was added with a magnetic stir bar and a dropping funnel containing 50 mL of 1.45 M NH_4OH (ACS grade from EDM) was maintained in an oil bath at 50 - 60 °C. To purge residual oxygen in the system, argon (99.999 %) gas was flushed for 5 min over the solution and for 10 min through the solution. 1. 0 mL of 2.0 M $FeCl_2{\cdot}4H_2O$ was added and followed by 4.0 mL of 1.0 M $FeCl_3{\cdot}6H_2O$ whilst stirring during argon purging. After stirring for 5 min., the basic solution was added drop-wise for about 45 min. with stirring and Ar purging. The final solution was pH 10-11 and was stirred vigorously for 1 h and further stirred for 1 h after removal from the heater source. The magnetic product (magnetite) was washed with Millipore water at ambient pH, followed by methanol, with subsequent air drying, and finally by drying in a vacuum oven at ambient temperature overnight. The overall yield was 97.0%.

The overall balanced chemical equation of the reaction is shown in equation (2-1); where it is noted that the molar ratio of Fe^{2+}: Fe^{3+} is 1:2.

$$2FeCl_{3(aq)} + FeCl_{2(aq)} + 8NH_{3(aq)} \rightarrow Fe_3O_{4(aq)} + 8NH_4Cl_{(aq)} \qquad (2\text{-}1)$$

2.3.2. Synthesis of activated carbon-based magnetite composites

A similar synthetic procedure of preparing magnetite was applied as above (*cf.* §2.1). In case of impregnation of magnetite onto activated carbon, 1.0 g of NORIT ROX 0.8 (as received from NORIT America) was added in the flask with Millipore water before adding $FeCl_2{\cdot}4H_2O$ and $FeCl_3{\cdot}6H_2O$ solution. By adjusting the molar ratio of $FeCl_2{\cdot}4H_2O$ and $FeCl_3{\cdot}6H_2O$ solution relative to the amount of AC, the magnetite-based composite containing AC was prepared. The ratio of magnetite in the AC (w/w %) was 32%, 19%, and 10%, respectively. The yield was 97.5%.

2.3.3.Goethite

Synthesis of nanoscale acicular goethite (α-FeOOH) was achieved by employing a 5/1 OH^-/Fe^{3+} molar ratio.[30] 10 mL of 4.0 M NaOH was added into 170 mL of Millipore water followed by 20 mL of 0.4 M $FeCl_3{\cdot}6H_2O$. The mixture was stirred vigorously at 30 °C for 24 h and the base with the salt in the mixture was continuously rinsed with Millipore water until the filtrate washings reached neutral pH. The product was dried in the air overnight and in a vacuum oven for 2 h at 55 °C. The overall balanced chemical equation of the reaction is shown in equation (2-2).

$$3NaOH_{(aq)} + FeCl_{3(aq)} \longrightarrow FeOOH_{(s)} + 3NaCl_{(aq)} + H_2O_{(l)} \qquad (2\text{-}2)$$

2.3.4. Characterization of magnetite and its composites

2.3.4.1. *Powder X-ray Diffraction (PXRD)*

Cu-K_α and Co-K_α were used as the X-ray irradiation source in the PXRD instrument (Model: Empyrean, manufacturer: PANalytical, the Netherland). The simulation of scanned magnetite and its composites were examined with the software of X'Pert Highscore Plus (Ver. 3.0b (3.0.2), PANalytical, Almelo, The Netherlands). The PXRD of magnetite and its composites (32%, 19%, and 10%), magnetite 19% were obtained by manual mixing commercial magnetite from Aldrich or goethite with NORIT ROX 0.8, respectively.

2.3.4.2. *Raman Spectroscopy*

Raman spectra were acquired using a Renishaw Invia spectrophotometer. Raman shifts were obtained at ambient temperatures by using a 514 nm Argon ion laser with following operating conditions: scan range (2000 ~ 100 cm^{-1}), power (1 mW), objective lens (50×), cosmic ray removal (on), detection time (10 s), and the number of accumulation scans (n=50). Raman spectra of the following materials were obtained: magnetite, magnetite composites (32%, 19%, and 10%), NORIT ROX 0.8, the commercial magnetite (Aldrich, nanopowder <50 nm), and goethite.

2.3.4.3. *Diffuse Reflectance Infra-red Fourier Transform Spectroscopy (DRIFTS)*

Samples were diluted with KBr (FTIR grade; Alfa Aesar) by 10% and scanned (n=256) from 4000 to 400 cm^{-1}. The applied resolution was 4 cm^{-1}. Diffuse Reflectance Infrared Fourier Transform (DRIFT) spectra were obtained using a Bio RAD FTS-40 spectrophotometer. DRIFTS spectra of magnetite, magnetite composites (32%, 19%, and 10%), NORIT ROX 0.8, commercial magnetite (Aldrich, nanopowder <50 nm), and goethite were obtained.

2.3.4.4. *Thermogravimetric analysis (TGA)*

TGA Q50 (TA Instruments) was used for analyzing samples. The procedure and mass flow control settings are listed in Table 2.1.

Table 2.1. Operating conditions of TGA Q 50

Procedure	**Mass flow control settings (N_2 gas 99.999 %)**
• Equilibrate at 32 °C	• Balance purge flow 50.00 mL/min
• Isothermal for 5 min	• Sample purge flow 90.00 mL/min
• Ramp 5.00 °C/min to 499.00 °C	

Thermograms were obtained for magnetite, magnetite composites (32%, 19%, and 10%), NORIT ROX 0.8, commercial magnetite (Aldrich, nanopowder <50 nm), and goethite.

2.3.4.5. *N_2 adsorption - desorption analysis (BET)*

The specific surface areas of magnetite, magnetite composites (32%, 19%, and 10%), NORIT ROX 0.8, the commercial magnetite (Aldrich, nanopowder <50 nm), and goethite were measured by Micromeritics ASAP 2020 (ver. 3.04). The accuracy of BET surface areas was ± 5 %. Samples weight ~ 200 mg were used “as received” for the magnetite from Aldrich and “as purified” for the synthesis of magnetite and magnetite composites. The degassing temperature was 100 °C.

2.3.4.6. *Scanning Electron Microscopy (SEM) and Transmission Electron Microscopy (TEM)*

SEM images of magnetites, magnetite composites, activated carbon, and goethite were obtained by a JEOL Scanning Electron Microscope (JEOL JSM-6010) using secondary electron irradiation and 20 kV. TEM images of magnetites, magnetite composites, activated carbon, and goethite were obtained by a Philips Transmission Electron Microscope (CM10) using 105,000× magnification and 80 kV accelerating voltage

2.4. Results and Discussion

2.4.1. Powder X-ray Diffraction (PXRD)

PXRD patterns of magnetite, magnetite composites with activated carbon (AC; NORIT ROX 0.8), and goethite are shown in Fig. 2.1. PXRD results of magnetite composites show two different Bragg diffraction patterns. PXRD for AC reveals amorphous features appearing between 20° and 30°; whereas, magnetite contributions in the composite material showed a more crystalline structure between 30° and 80°. The PXRD results are similar to the characteristic peaks at $2\theta = 30.17°$, 35.46°, 43.38°, 53.69°, 57.23°, and 62.77°, corresponding to (220), (311), (400), (422), (511), and (440) Miller indices respectively. The phase identification of magnetite (Fig. 2.1. A) and goethite[31] (Fig. 2.1. D: powder diffraction file (PDF) pattern 00-029-0713) are well described by the simulated PXRD spectral results using the X’Pert Highscore Plus software (refer to the blue lines under Bragg diffraction peaks). The physical mixture of magnetite 19% with the activated carbon retained both the amorphous activated carbon features and the crystal magnetite Bragg reflections. The peak intensities were not scaled by the content of magnetite in the composites because the size of scattering domains, the content of the unit cell, density of the crystalline materials, and structure factor and volume were not identical between samples. The grain sizes of magnetite and the commercial sample from Aldrich are shown in Table 2.2. that was calculated using the Scherrer relationship.[32] In equation 2-3, τ is the grain size (nm), k is the Scherrer constant (0.94 for spherical crystals with cubic symmetry), λ is the wavelength (0.179 nm) of Co K_{α}, β is the full-width-half maximum of the highest intensity peak in radians, and cos ϴ is the angle (degree) value at the highest intensity peak in radians.

$$\tau = \frac{k \times \lambda}{\beta \times \cos \mathit{\Theta}} \qquad (2\text{-}3)$$

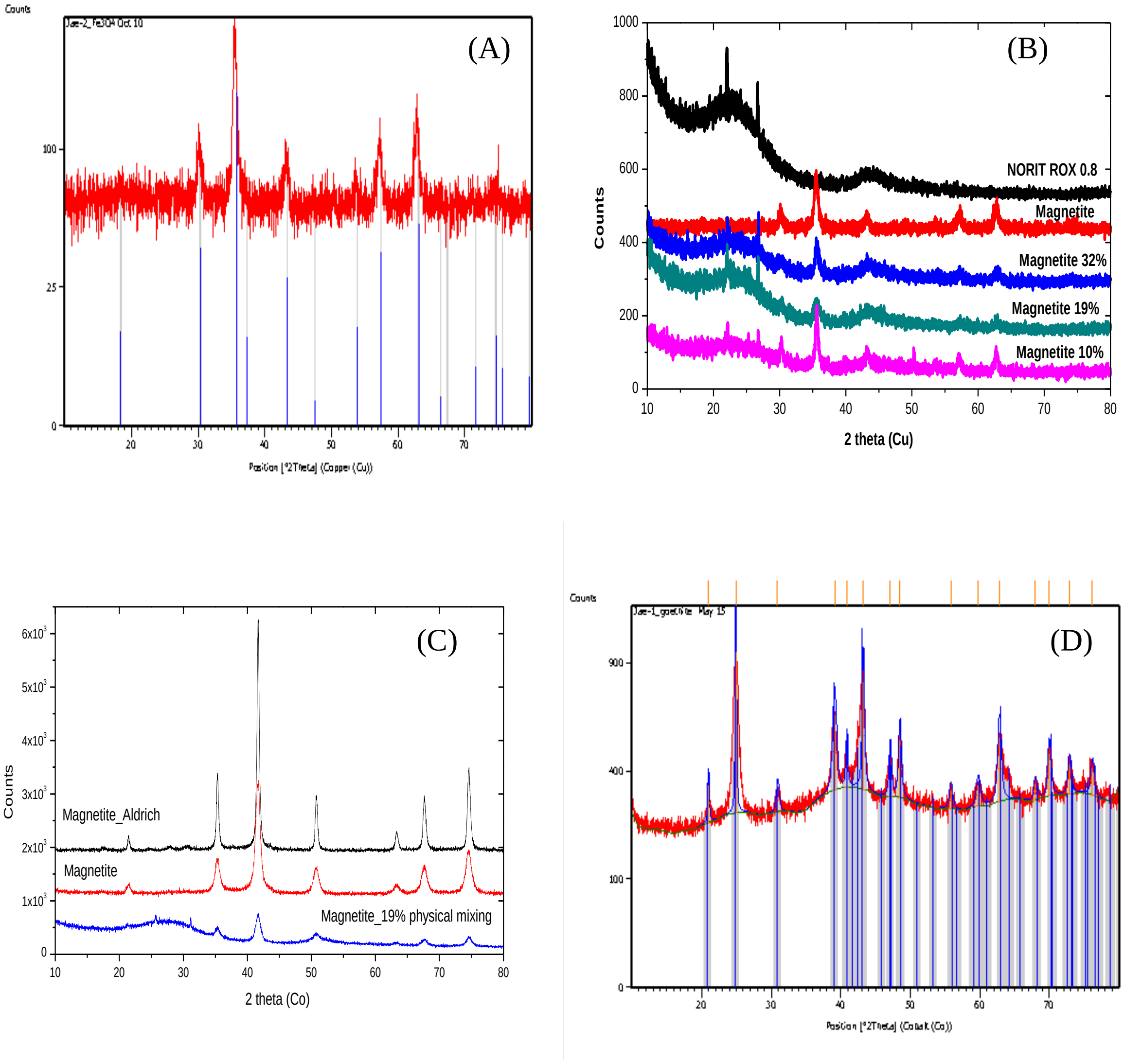

Figure 2.1. PXRD results for magnetite (A), composite AC materials (B), comparison of the commercial product from Aldrich and physical mixtures made magnetite composite (19%) with AC (C), and goethite (D).

Table 2.2. Comparison of grain size (nm) for commercial and synthetic magnetite

Magnetite	**As prepared**	**Magnetite_Aldrich**
Grain size (nm)	14	28

2.4.2. Raman Spectroscopy

The Raman spectra of magnetite, and its composites, along with goethite are shown in Fig. 2.2. The diagnostic band of magnetite occurs at 680 cm^{-1}. The observed Raman spectra of the synthesized magnetite and its composite materials are assigned 184 cm^{-1} (Fe-O asymmetric bending, $T_{2g(1)}$), 337 cm^{-1} (Fe-O symmetric bending, E_g), 503 cm^{-1} (Fe-O asymmetric stretching, $T_{2g(2)}$), 689 cm^{-1} (Fe-O symmetric stretching, A_{1g}), and 707 cm^{-1}.[33] Among them, the band near 707 cm^{-1} is the typical signature of Fe-O symmetric stretching for maghemite present in magnetite.[24] The intensity of the Raman bands for composite materials is not proportional to the content of magnetite in the AC composites. This difference in intensity can be explained by presence of different crystalline forms of magnetite in the sample composites with different sample orientations, owing to the band polarization effects[34] and self-absorption. The overtone band of maghemite appeared around 1,413 cm^{-1} and D band and G band of the activated carbon for the composites are shown at 1,350 cm^{-1} and 1,599 cm^{-1} respectively. Raman bands for goethite appeared at 245 cm^{-1} (Fe-O symmetric bending), 301 cm^{-1}, 396 cm^{-1} (Fe-O-Fe and Fe-OH symmetric stretching), 480 cm^{-1}, 553 cm^{-1} (Fe-OH asymmetric stretching), and 686 cm^{-1} and are in good agreement with results reported elsewhere.[34] Other peaks at 893 cm^{-1}, 1,001 cm^{-1} (Fe-OH asymmetric stretching), 1,134 cm^{-1} (overtone band of Fe-OH asymmetric stretching), and 1,312 cm^{-1} (probably Fe-OH asymmetric stretching of lepidocrocite, γ-FeOOH as a contaminant) also appeared. The Raman results are summarized in Table 2.3.

Table 2.3. Assigned Raman bands of the prepared magnetite, its composites, and goethite

Magnetite and its composites	**Goethite**
184 cm^{-1} Fe-O asymmetric bending, $T_{2g(1)}$	245 cm^{-1} Fe-O symmetric bending
337 cm^{-1} Fe-O symmetric bending, E_g	301 cm^{-1} Fe-O-Fe symmetric stretching
503 cm^{-1} Fe-O asymmetric stretching, $T_{2g(2)}$	396 cm^{-1} Fe-OH symmetric stretching
689 cm^{-1} Fe-O symmetric stretching, A_{1g}	480 cm^{-1} Fe-OH asymmetric stretching
707 cm^{-1} Fe-O symmetric stretching of maghemite	553 cm^{-1} Fe-OH asymmetric stretching
1413 cm^{-1} overtone band of maghemite	893 cm^{-1} Fe-OH asymmetric stretching
1350 cm^{-1} D band of AC	1,001 cm^{-1} Fe-OH asymmetric stretching
1599 cm^{-1} G band of AC	1,134 cm^{-1} overtone band of Fe-OH asymmetric stretching
	1,312 cm^{-1} probably Fe-OH asymmetric stretching of lepidocrocite, γ-FeOOH as a contaminant

The total iron (Fe) content in the magnetite composite materials was determined using a flame-based Atomic Absorption Spectrophotometer (Flame AAS: novAA® 300, Analytik Jena Group) at 248.3 nm, as shown in Table 2.4. The theoretical content of Fe in the magnetite is 72.3 %. The magnetite showed some residual iron (II) and iron (III) chlorides. Because of the heterogeneous distribution of magnetite in the composites, the average total Fe content varies.

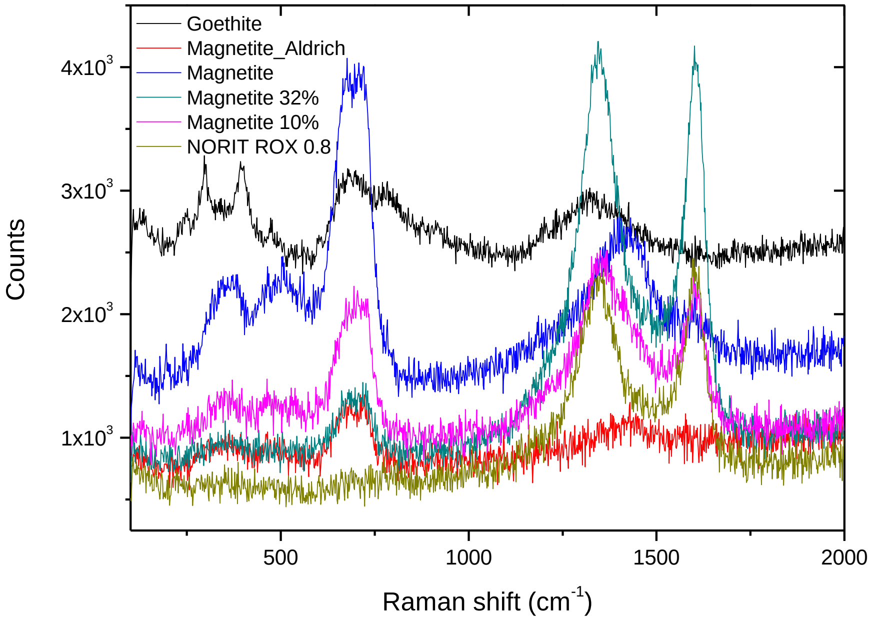

Figure 2.2. Raman spectra of magnetite and its composites with NORIT ROX 0.8 at ambient temperature and λ_{ex} = 514 nm. Particles from the preparation procedure were used as samples without further evidence of morphological change and their sizes were variable.

Table 2.4. The total Fe content (%)[1] of magnetite and its composite materials determined by AAS

Materials	Sample 1	Sample 2	Sample 3	Average
Magnetite	77.4±1.1	74.0±0.4	51.7±0.5	67.7±0.7
Magnetite (32%)	24.3±0.0	79.8±0.5	32.5±0.1	45.5±0.1
Magnetite (19%)	21.8[1]	12.6[1]	28.9±0.4	21.1±0.1
Magnetite (10%)	43.3±0.1	7.30[1]	19.3±0.1	23.3±0.07
NORIT ROX 0.8	0.13[1]	2.03±0.01	0.143±0.006	0.768±0.03

[1] The standard error is not reported since it was negligible within the limits of detection for various samples. Each sample # represents an estimate of Fe content determined in duplicate; where samples 1, 2, and 3 represent different regions of the sample.

2.4.3. Diffuse Reflectance Infra-red Fourier Transform Spectroscopy (DRIFTS)

FT-IR (DRIFTS) spectra of bulk magnetite composites and goethite are shown in Fig. 2.3. with spectral assignments listed in Table 2.5. The magnetite and its composites exhibit two strong infrared absorption bands at 570 cm^{-1} (v_1) for the Fe^{3+}-O stretching mode of the tetrahedral and octahedral sites and 390 cm^{-1} (v_2) for the Fe^{2+}-O stretching mode of the octahedral sites,[35,36] provided that Fe^{3+} ion displacements at tetrahedral sites are negligible.[36] However, the v_1 band at 570 cm^{-1} is shifted and split into two bands at 632 cm^{-1} and 594 cm^{-1}. This shift may be due to the increased surface area of the surface oxides of the nanoparticles where the sites are relaxed and not crystalline. This structural change results in a change in symmetry and charge redistribution of the surface states. Maghemite, a defective form of magnetite, also appeared at 630 cm^{-1}, 590 cm^{-1}, and 430 cm^{-1}. The physical mixing of magnetite 19% with AC showed a very weak intermolecular interaction with the AC support material, and thus its molecular vibrational modes were similar to the composite 10%. The characteristic IR bands of goethite were found at 630, 795 and 890 cm^{-1}.[37] The synthesized goethite showed these bands at 623 cm^{-1} for lattice vibration, 793 cm^{-1} for -OH deformation (γ-OH), and 887 cm^{-1} for -OH deformation (δ-OH).[38] There are also absorption bands of intramolecular H-bonds (3,167 cm^{-1}) and of residual FeCl$_3$ (1,533 cm^{-1}, 1,325 cm^{-1}, and 443 cm^{-1}).

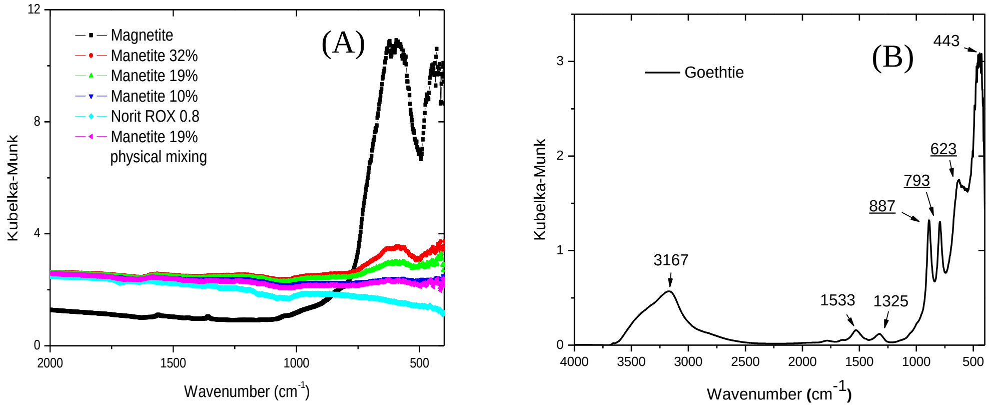

Figure 2.3. IR spectra of magnetite composites (A) and goethite (B).

Table 2.5. FT-IR (DRIFTS) spectra of magnetite, its composite, and goethite

Magnetite and its composites	**Goethite**
390 cm^{-1} Fe^{2+}-O stretching in octahedral sites	623 cm^{-1} lattice vibration
594 and 632 cm^{-1} Fe^{3+}-O stretching in tetrahedral and octahedral sites	793 cm^{-1} -OH deformation (γ-OH)
630, 590, and 430 cm^{-1} maghemite as a defect	887 cm^{-1} -OH deformation (δ-OH)
	1,533, 1,325, and 443 cm^{-1} residual $FeCl_3$
	3,167 cm^{-1} intramolecular H-bond

2.4.4. Thermogravimetric analysis (TGA)

TGA results for magnetite composites and goethite are shown in Fig. 2.4. Thermal behavior of iron oxide/oxyhydroxide illustrates how removal of hydroxyl groups and phase transformation of composite materials vary as heating occurs. Surface bound water to the surface of magnetite composites can be grouped into several categories: absorbed free surface water, pore bound crystal water, and hydroxyl groups. The decomposition temperature (T_m) of these waters might be 25 - 140 °C, 200 - 480 °C, and 500 - 800 °C, respectively.[33] All composites including magnetite showed these hydrates display characteristic of free and bound pore water, except goethite. In case of goethite, an additional thermal event around 355 °C was observed, and is consistent with the goethite-hematite (α-Fe_2O_3) transformation[39,40] followed by loss of hydroxyl groups, described by equation (2-4).

$$2\ \alpha\text{-FeOOH} \rightarrow \alpha\ Fe_2O_3 + H_2O \qquad (2\text{-}4)$$

For the high crystalline goethite-hematite transformation, this endothermic peak is found at 385 °C. However, for a fine-grained and amorphous goethite, this dissociation peak is often observed at lower temperature.[34]

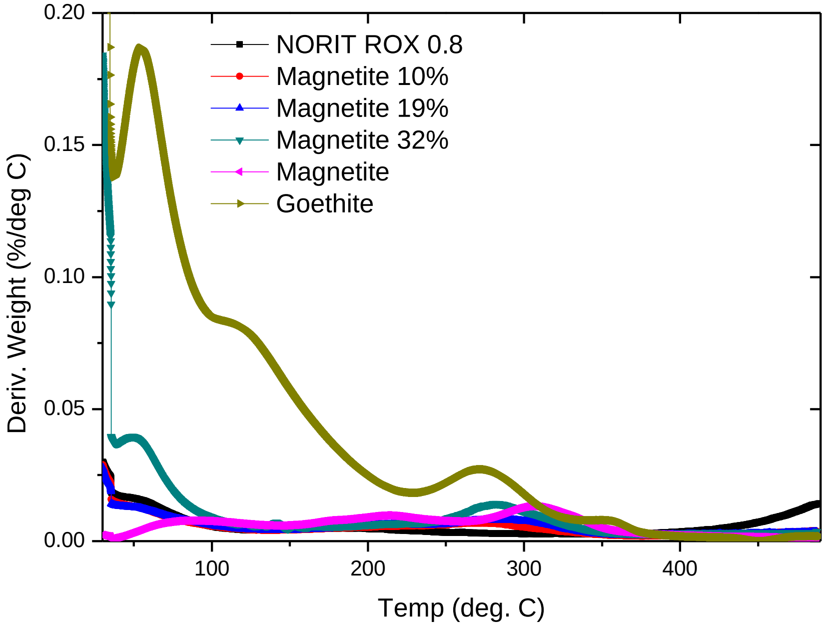

Figure 2.4. TGA results for magnetite composites and goethite.

2.4.5. N_2 adsorption – desorption analysis (BET)

The nitrogen adsorption-desorption results are shown in Fig. 2.5. and Table 2.6. The BET surface area consists of the external surface calculated from a *t*-plot and the micro-pore area (internal surface area) calculated from the BET equation.[41] The relationship between the specific surface area and the content of magnetite in the NORIT ROX 0.8 shows a linear correlation. The results show a trend of increasing micropore area and micropore volume with a decreasing average pore diameter as the ratio of magnetite decreases or as the content of NORIT ROX 0.8 increases. The hysteresis loops of the composites and magnetite represent the H-3 or H-4 type of the non-rigid slit-shaped pores.[42] An overview of the BET specific surface areas are given in Table 2.6 and it is believed that magnetite crystals were distributed within pores up to two times that greater than the surface sites.

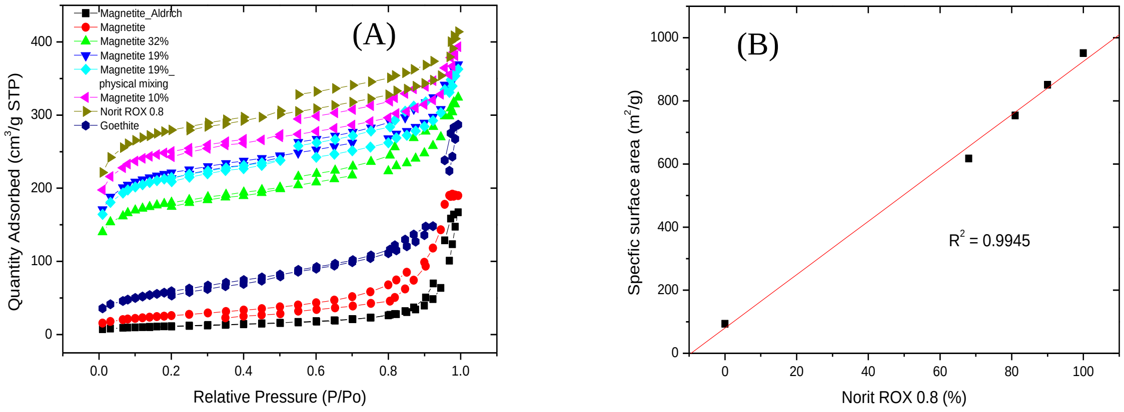

Figure 2.5. N_2 adsorption-desorption isotherms (A) for magnetite composites and goethite at -196. °C and a linear relationship (B) between specific surface area (m^2/g) of magnetic composites and the relative content (%) of NORIT ROX 0.8.

The pore-blocking ratio with magnetite in the composite materials was calculated and listed in Table 2.7. As the ratio of magnetite in the composites increased, the ratio of pore blockage by magnetite in the composites also increased in the pore sites and on the external surface accessible sites. However, blockage occurs within the pores as the level of magnetite impregnation increased. The physical mixture of magnetite and activated carbon (magnetite 19%)* showed slightly higher blockage than that of the magnetite 19% composite material. Blockage occurs mainly in the pores than on the surface due to the uneven distribution of magnetite by manual mixing of the activated carbon and possible damage of the pore structure by grinding the materials prior to physical mixing. Therefore, magnetite particles form on the surface, followed by the pores and surface sites, resulting in possible pore blockage.

Table 2.6. BET results of magnetite composite materials with activated carbon

Iron Oxide	**Specific Surface Area** (SSA, m^2/g)		**Micropore Area** (m^2/g)	**External Surface Area** (m^2/g)	**Micropore Volume** (cm^3/g)	**Average Pore Diameter** (Å)
	BET	Langmuir				
Magnetite (Aldrich)	4.10E+01	5.68E+01	4. 60	3.64E+01	1.74E-03	1.52E+02
Magnetite (100 %)	9.35E+01	1.30E+02	6.90E+00	8.66E+01	2.20E-03	1.26E+02
Magnetite (32 %)	6.17E+02	8.23E+02	3.84E+02	2.33E+02	1.76E-01	2.99E+01
Magnetite (19 %)[1]	7.33E+02	9.82E+02	4.52E+02	2.81E+02	2.08E-01	2.79E+01
Magnetite (19 %)	7.54E+02	1.01×10^3	4.80E+02	2.74E+02	2.22E-01	2.78E+01
Magnetite (10 %)	8.51E+02	1.14×10^3	5.66E+02	2.85E+02	2.62E-01	2.58E+01
NORIT ROX 0.8	9.51E+02	1.27×10^3	6.41E+02	3.10E+02	2.96E-01	2.47E+01

[1] refers to manual mixing of magnetite (19 %)/ NORIT ROX 0.8 (81 %).

Table 2.7. Ratio of pore blockage with magnetite in the composite materials

Iron Oxides	**Specific Surface Areas (m^2/g)**			**Ratio of blockage in the composites (%)**		
	BET	Micropore	External	Pore	External	Total
Magnetite (Aldrich)	41.0	4.60	36.4	-	-	-
Magnetite (100%)	93.5	6.90	86.6	-	-	-
Magnetite (32%)	617.	384.	233.	27.0	8.10	35.1
Magnetite (19%)[*]	733.	452.	281.	19.9	3.05	23.0
Magnetite (19%)	754.	480.	274.	16.9	3.79	20.7
Magnetite (10%)	851.	566.	285.	7.89	2.63	10.5
NORIT ROX 0.8	951.	641.	310.	-	-	-

Note: The uncertainty of BET measurement is ± 5%.

Pore blocking ratio (%) = (BET specific area of pores of NORIT ROX 0.8 - BET specific area of a composite) / BET specific area of NORIT ROX 0.8 × 100. For Magnetite (10%), (641-566)/951 × 100 = 7.89

2.4.6. Scanning Electron Microscopy (SEM) and Transmission Electron Microscopy (TEM)

Figure 2.6 illustrates electron microscopy images of goethite (A: SEM, A': TEM), NORIT ROX 0.8 (B: SEM, B': TEM), magnetite (C: SEM, S': TEM), magnetite 32 % (D: SEM, D': TEM), magnetite 19 % (E: SEM, E': TEM), and magnetite 10 % (F: SEM, F': TEM). The shape of goethite, magnetite, and the activated carbon is acicular (100-200 × 20-40 nm), round (diameter: 10-30 nm), and slit-like porous, respectively. However, the magnetite composites show pseudo-cubic structure with evidence of pores in the SEM images. Based on the SEM images, the pores and surface sites of AC were covered by a layer of amorphous crystalline magnetite. As well, magnetite may nucleate firstly in the pores of activated carbon with further growth over the remaining available surface of activated carbon.

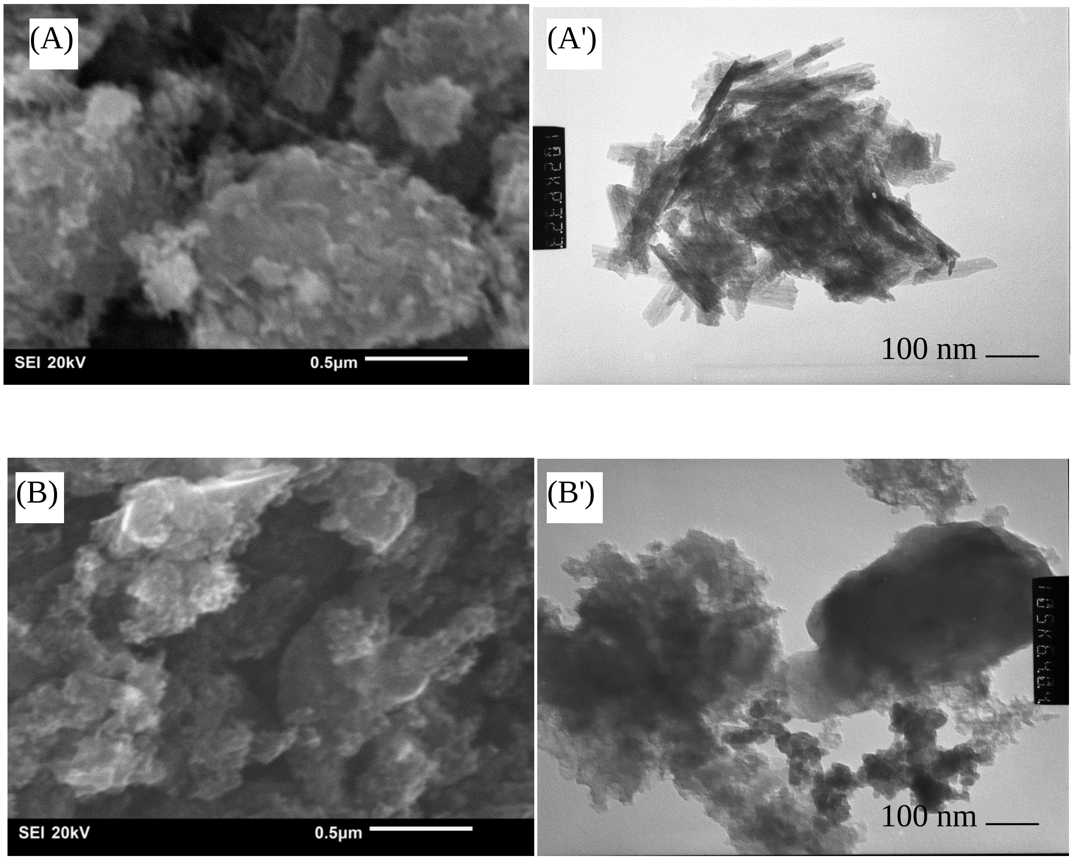

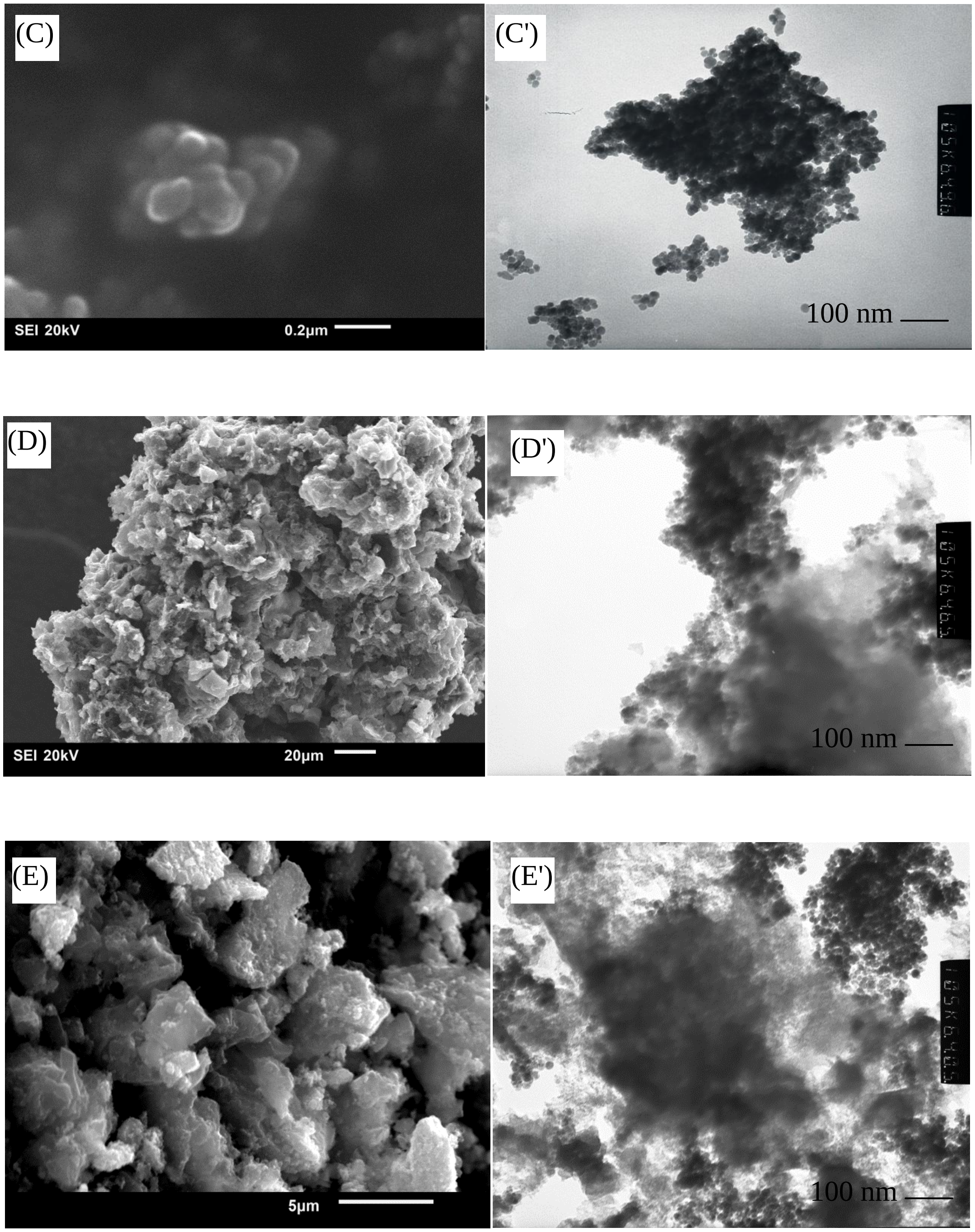
(C)
SEI 20kV
0.2μm
(C')
100 nm
(D)
SEI 20kV
20μm
(D')
100 nm
(E)
5μm
(E')
100 nm

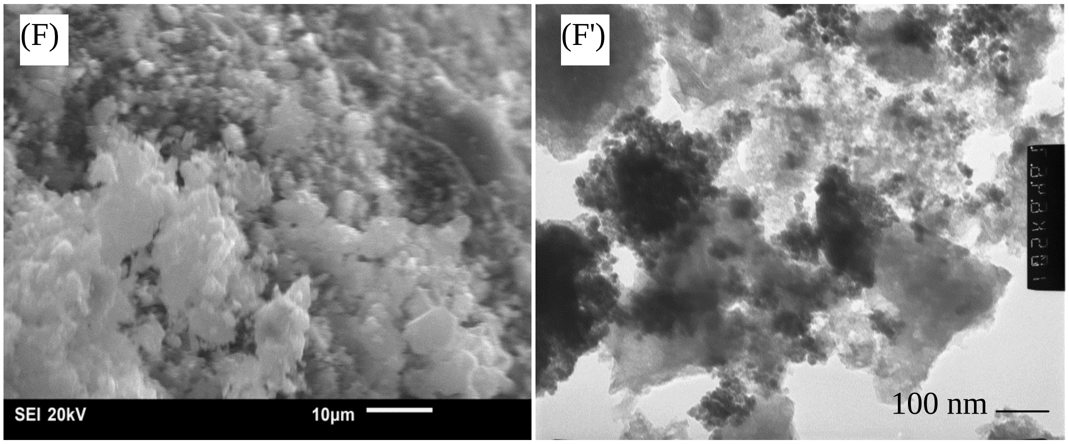

Figure 2.6. SEM and TEM images of goethite (A: SEM, A': TEM), NORIT ROX 0.8 (B: SEM, B': TEM), magnetite (C: SEM, S': TEM), magnetite 32 % (D: SEM, D': TEM), magnetite 19 % (E: SEM, E': TEM), and magnetite 10 % (F: SEM, F': TEM).

2.5. Conclusions

The co-precipitation method using Fe (II) and Fe (III) solutions at anaerobic conditions represents a facile and eco-friendly preparation method for small particle sizes (~ 14 nm) of magnetite in which can provide better adsorption performance than large particles due to its greater surface area. Commercial magnetite served as a reference material and showed almost double particle size (~28 nm) relative to the synthesized product. Raman spectroscopy (689 cm^{-1} for magnetite and 301, 396, 686 cm^{-1} for goethite), IR spectroscopy (594 and 632 cm^{-1} for magnetite and 623, 793, 887 cm^{-1} for goethite), and PXRD using simulated results support that the synthesized magnetite, goethite, and magnetite composites with activated carbon were successfully prepared. The total Fe content of the prepared magnetite was in good agreement with the theoretical content (72.3 %), with some residual Fe (II and III) ions. However, the magnetite composites showed a variable distribution of the total Fe content because of the presence of inhomogeneous Fe in the activated carbon matrix during the preparation process by the Kelvin effect to stimulate particle growth in solution (Ostwald ripening). The location of magnetite in the activate carbon was not unequivocally supported by instrumental techniques investigated herein. Further evidence for the location of iron oxide on surface *vs*. pore sites can be accomplished by using X-ray crystallography. Most X-rays deeply penetrate into a crystal, but some scattering by atomic sites which may reside in pores or on the surface of activated carbon.

The scattered X-rays add up in phase in some directions, resulting in a bright spot and analysis can provide the location of magnetite on the surface *vs*. pore sites of activated carbon. Phase transformation of goethite to hematite occurred by dehydration of goethite and magnetite particles in the activated carbon that were grown in the pores and on the surface of AC was evidenced by N_2 adsorption-desorption results. The magnetic property of the activated carbon composites with magnetite represent a promising material for the facile separation of waterborne organics (e.g., dyes, volatile organic compounds, etc) and inorganics (e.g., heavy metals and oxyanions of selenium and arsenic) in wastewater treatment processes if an electromagnet is used for separation and recycling the adsorbent material.

2.6. Acknowledgments

The authors acknowledge NORIT America Inc. for provision of activated carbon research samples. The Natural Sciences and Engineering Research Council of Canada (NSERC) and the University of Saskatchewan are gratefully acknowledge for financial support of this project.

2.7. References

1. Cornell, R. M.; Schwertmann, U., *The Iron Oxides: Structure, Properties, Reactions, Occurrences, and Uses*, 2nd ed.; Wiley-VCH: Weinheim, Germany, 2003, pp. 2-3.

2. Lam, U. T.; Mammucari, R.; Suzuki, K.; Foster, N. R. Processing of iron Oxide nanoparticles by supercritical fluids. *Ind. Eng. Chem. Res.* **2008**, *47*, 599-614.

3. Wernsdorfer, W. Magnetism of Nanometer-Sized Particles and Clusters. In *Metal Clusters at Surfaces: Structure, Quantum Properties, Physical Chemistry*; Meiwes-Broer; K.-H., Ed.; Springer: Berlin, Germany, 2000, pp. 211-231.

4. Tartaj, P.; Morales, M. D.; Veintemillas-Verdaguer, S.; Gonzalez-Carreno, T.; Serna, C. J. The preparation of magnetic nanoparticles for applications in biomedicine. *J. Phys. D: Appl. Phys.* **2003**, *36*, R182-R197.

5. Neuberger, T.; Schopf, B.; Hofmann, H.; Hofmann, M.; von Rechenberg, B. Superparamagnetic nanoparticles for biomedical applications: Possibilities and limitations of a new drug delivery system. *J. Magn. Magn. Mater.* **2005**, *293*, 483-496.

6. Jiang W.; Yang H. C.; Yang S. Y.; Horng, H. E.; Hung, J. C.; Chen, Y. C.; Hong, Chin-Yih. Preparation and properties of superparamagnetic nanoparticles with narrow size distribution and biocompatible. *J. Magn. Magn. Mater.* **2004**, *283*, 210-214.

7. Vayssières, L.; Chanéac, C.; Tronc, E.; Jolivet, J. P. Size tailoring of magnetite particles formed by aqueous precipitation: An example of thermodynamic stability of nanometric oxide particles. *J.Colloid. Interf. Sci*. **1998**, *205*, 205-212.

8. Massart, R. Preparation of aqueous magnetic liquids in alkaline and acidic media. *IEEE Transactions on Magnetics*, **1981**, *MAG-17*, 1247-1248.

9. Park, J.; An, K.; Hwang, Y.; Park, J. G.; Noh, H. J.; Kim, J. Y.; Park, J. H.; Hwang, N. M.; Hyeon, T. Ultra-large-scale syntheses of monodisperse nanocrystals. *Nat. Mater*. **2004**, *3*, 891-895.

10. Baier, J.; Koetz, J.; Kosmella, S.; Tiersch, B.; Rehage, H. J. Polyelectrolyte-modified inverse microemulsions and their use as templates for the formation of magnetite nanoparticles. *Phys. Chem. B.* **2007**, *111*, 8612-8618.

11. Taniguchi, T.; Nakagawa, K.; Watanabe, T.; Matsushita, N.; Yoshimura, M. J. Hydrothermal growth of fatty acid stabilized iron oxide nanocrystals. *Phys. Chem. C.* **2009**, *113*, 839-843.

12. Tronc, E.; Jolivet, J. P.; Massart, R. Defect spinel structure in iron oxide colloids. *Mater. Res. Bull*. **1982**, *17*, 1365-1369.

13. Neveu-prin, S.; Cabuil, V.; Massart, R.; Escaffre, P.; Dussaud, J.J. Encapsulation of magnetic fluids. *Magn. Magn. Mater*. **1993**, *122*, 42-45.

14. Massart, R.; Dubois, E.; Cabuil, V.; Hasmonay, E. J. Preparation and properties of monodisperse magnetic fluids. *Magn. Magn. Mater*. **1995**, *149,* 1-5.

15. Lu, A.-H.; Salabas, E. L.; Schuth, F. Magnetic nanoparticles: Synthesis, protection, functionalization, and application. *Angew. Chem., Int. Ed*. **2007**, *46*, 1222-1244.

16. Laurent, S.; Forge, D.; Port, M.; Roch, A.; Robic, C.; Elst, L. V.; Muller, R. N. Magnetic iron oxide nanoparticles: Synthesis, stabilization, vectorization, physicochemical characterizations, and biological applications. *Chem. Rev*. **2008**, *108*, 2064-2110.

17. Gallegos-Garcia, M.; Ramírez-Muñiz, K.; Song, S. Arsenic removal from water by adsorption using iron oxide minerals as adsorbents: A Review. *Miner. Process. Extr. M.*, **2012**, *33,* 301-315.

18. Vaclavikova, M.; Gallios, G. P.; Hredzak, S.; Jakabsky, S. Removal of arsenic from water streams: an overview of available techniques. *Clean. Techn. Environ. Policy*, **2008**, *10*, 89-95.

19. Strangway, D. W.; Honea, R. M.; McMahon, B. E.; Larson, E. E. The magnetic properties of naturally occurring goethite. *Geophys. J. R. Astr. Soc.* **1968**, *15,* 345-359.

20. Do, D. D. A model for surface diffusion of ethane and propane in activated carbon. *Chem. Eng. Sci*. **1996**, *51*, 4145-4158.

21. Kwon, J. H.; Wilson, L. D. Surface modified activated carbon with β-cyclodextrin - Part I. Synthesis and characterization. *J. Environ. Sci. Heal. A*, **2010**, *45*, 1775-1792.

22. Zhi, J.; Wang, Y.; Lu, Y.; Ma, J.; Luo, G. In situ preparation of magnetic chitosan/Fe_3O_4 composite nanoparticles in tiny pools of water-in-oil microemulsion. *React. Funct. Polym*. **2006**, *66*, 1552-1558.

23. Wang, C.; Feng, C.; Gao, Y.; Ma, X.; Wu, Q.; Wang, J. Preparation of a graphene-based magnetic nanocomposite for the removal of an organic dye from aqueous solution. *Chem. Eng. J*. **2011**, *173,* 92-97.

24. Wan, M.; Zhou, W.; Li, J. Composite of polyaniline containing iron oxides with nanometer size. *Synthetic. Met.*, **1996**, *78,* 27-31.

25. Castro, C. S.; Guerreiro, M. C.; Gonçalves, M.; Oliveira, L. C. A.; Anastácio, A. S.

Activated carbon/iron oxide composites for the removal of atrazine from aqueous medium. *J. Hazard. Mater.*, **2009**, *164*, 609-614.

26. Zhu, H. Y.; Fu, Y. Q.; Jiang, R.; Jiang, J. H.; Xiao, L.; Zeng, G. M.; Zhao, S. L.; Wang, Y. Adsorption removal of congo red onto magnetic cellulose/Fe_3O_4/activated carbon composite equilibrium, kinetic and thermodynamic studies. *Chem. Eng. J.* **2011**, *173*, 494-502.

27. Fan, H.; Xu, Q.; Guo, Y.; Cao, Y. Al_2O_3/Fe_2O_3 Mesoporous composite prepared with activated carbon template in supercritical carbon dioxide. *Ind. Eng. Chem. Res.* **2006**, *45,* 5009-5012.

28. Valusová, E.; Vandzurová, A.; Pristas, P.; Antalík, M.; Javorský, P. Water treatment using activated carbon supporting silver and magnetite. *Water Sci. Technol*. **2012**, *66,* 2772-2778.

29. Berger, P.; Adelman, N. B.; Beckman, K. J.; Campbell, D. J.; Lisensky, G. C.; Ellis, A. B. Preparation and properties of an aqueous ferrofluid. *J. Chem. Ed*., **1999**, *76*, 943-948.

30. Montes-Hernandez, G.; Renard, F.; Chiriac, R.; Findling, N.; Ghanbaja, J.; Toche, F. Sequential precipitation of a new goethite–calcite nanocomposite and its possible application in the removal of toxic ions from polluted water. *Chem. Eng. J.*, **2013**, *214,* 139-148.

31. Gao, X.; Schulze, D. G. Precipitation and transformation of secondary Fe oxyhydroxides in a histosol impacted by runoff from a lead smelter. *Clay. Clay Miner*. **2010**, *58*, 377-387.

32. Langford, J. I.; Wilson, A. J. C. Scherrer after sixty years: A survey and some new results in the determination of crystallite size. *J. Appl. Cryst*., **1978**, *11*, 102-113.

33. Shebanova, O. N.; Lazor, P. Raman spectroscopic study of magnetite ($FeFe_2O_4$): a new assignment for the vibrational spectrum. *J. Solid State Chem*., **2003**, 174, 424–430.

34. de Faria, D. L. A.; Silva, S. V.; de Oliveira, M. T. Raman Microspectroscopy of some iron oxides and oxyhydroxides. *J. Raman Spectrosc*., **1997**, *28,* 873-878.

35. Waldron, R. D. Infrared spectra of ferrites. *Phys. Rev.*, **1955**, *99,* 1727-1735.

36. Ishii, M.; Nakahira, M. Infrared absorption spectra and cation distributions in $(Mn, Fe)_3O_4$. *Solid. State. Commun.,* **1972**, *11*, 209-212.

37. Cambier, P. Infrared study of goethites of varying crystallinity and particle size: I. Interpretation of OH and lattice vibration frequencies. Clay Miner., **1986**, 21, 191-200.

38. Ristić, M.; Opačak, I.; Musić, S. The synthesis and microstructure of goethite particles precipitated in highly alkaline media. J. Alloy. Compd., **2013**, 559, 49-56.

39. Rizov, B. Phase transformations from goethite to hematite and thermal decomposition in

various nickeliferous laterite ores. *J. Chem. Technol. Metall*., **2012***, 47,* 207-210.
40. Swamy, Y. V.; Kar, B. B.; Mohanty, J. K. Physico-chemical characterization and sulphatization roasting of low-grade nickeliferous laterites. *Hydrometallurgy*, **2003**, *69*, 89-98.
41. Dandy, A. J.; Nadiye-Tabbiruka, M. S. The Effect of heating in vacuo on the microporosity of sepiolite. Clays Clay Miner., **1975**, 23, 428-430.
42. Thommes, M. Physical adsorption characterization of nanoporous materials. *Chemie. Ingenieur Technik*, **2010**, *82*, 1059-1073.

CHAPTER 3

MANUSCRIPT 2

Description

This chapter is a verbatim copy of a manuscript submitted for publication to a peer-reviewed journal entitled the Journal of Colloid and Interface Science (JCIS-14-56).

Aqueous solutions containing sodium selenite (Na_2SeO_3) as a representative of inorganic toxic non-metal were adsorbed onto the surface of magnetite, magnetite composites with activated carbon, NORIT ROX 0.8, and goethite at pH 5.26 at 21 °C at variable time increments and at equilibrium. The equilibrium and kinetic parameters such as the adsorbed amount of selenium, Q_m (Se, µmol/g) and Q_e (Se, mg/g) were evaluated, and the Fe leaching dependence with temperature was studied.

Authors' Contribution

I carried out all experiments and Lee D. Wilson and R. Sammynaiken supervised the research. I investigated various analytical methods of Se determination such as Hydride Generation Atomic Absorption spectroscopy (HGAAS). To avoid any cross-contamination of magnetite nano-particles into my analyte solutions, careful sampling was done over specific time intervals. I developed a protocol "*in-situ*" sampling of Se in aqueous solution for applications in solid-solution kinetic studies. I carried out the experimental work, wrote the first draft and following amendment, and received assistance from my supervisors in the editing of subsequent drafts. My mentors guided me throughout the research process to complete experimental work.

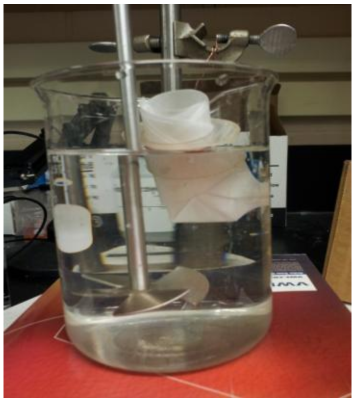

Relation of Chapter 3 (manuscript 2) to the overall objectives of this project

This work relates to the research hypothesis described in the section 1.2 in Chapter 1. By evaluating sorptive uptake capacity for inorganic selenium species with the synthetic and commercial magnetite, magnetite composites, activated carbon, and goethite, the kinetic parameters were investigated using pseudo-first and second-order reaction models and the Eyring equation. The Fe leaching dependence on temperature was studied.

Graphical Abstract

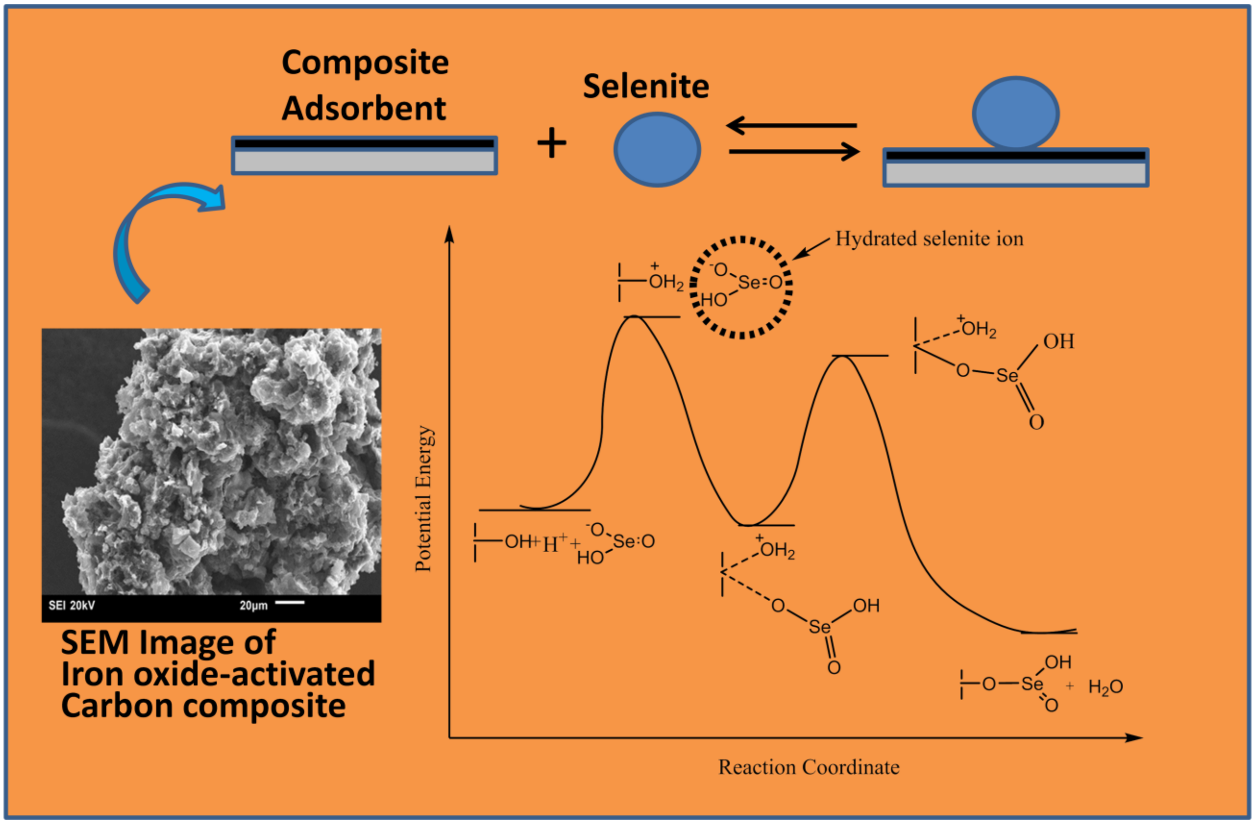

Research Highlights

- Composite materials containing activated carbon and iron oxide were studied
- The sorption properties of sorbents were studied at equilibrium and kinetic conditions
- Composites display variable Se affinity, reduced Fe leaching, and magnetic properties
- Se uptake was favoured by goethite and magnetite domains of the sorbent
- Lewis acid sites (Fe-OH and Fe-O groups) enable tuning of the surface chemistry

3.

SORPTIVE UPTAKE OF SELENIUM WITH A MAGNETIE AND COMPOSITE MATERIALS WITH ACTIVATED CARBON

Jae H. Kwon[1], Lee D. Wilson[1]*, and R. Sammynaiken[2]

[1] University of Saskatchewan, 110 Science Place, Saskatoon, SK S7N 5C9 Canada; E-Mail: jak878@mail.usask.ca

[2] Saskatchewan Structural Science Centre, University of Saskatchewan, 110 Science Place, Saskatoon, SK S7N 5C9 Canada; E-Mail: r.sammynaiken@usask.ca

***** Author to whom correspondence should be addressed; E-Mail: lee.wilson@usask.ca; Tel.: +1-306-966-2961; Fax: +1-306-966-4730

3.1 Abstract

Kinetic and equilibrium sorption studies for the uptake of selenite with synthetic magnetite (Mag-P), commercial magnetite (Mag-C), synthetic magnetite/ activated carbon composite with 19% magnetite (CM-19), goethite, and activated carbon (AC) were studied. Uptake studies were carried out using an *in-situ* one-pot device at pH 5.26 in aqueous phthalate buffer solution at variable temperature with atomic absorbance for measurement of equilibrium selenite. The sorptive uptake at equilibrium and kinetic conditions showed the following order: goethite > Mag-P > Mag-C > CM-19. Mag-P showed an *apparent* negative E_a and $\Delta H^{\ddagger}$ kinetic parameters, indicative of a composite kinetic process. In contrast, Mag-C, CM-19, and goethite showed positive values for E_a and $\Delta H^{\ddagger}$. The value of $\Delta S^{\ddagger}$ for AC showed a positive value suggesting that bond breakage occurs during the transition state between unbound and adsorbed species. Fe leaching was significantly attenuated in the case of CM-19 by immobilizing magnetite particles within the pores and onto the graphene surface of AC at temperatures below 293 K.

Keywords: magnetite; goethite; composite material; sorption kinetics; selenite; adsorption; kinetics

3.2 Introduction

The fate and distribution of selenium in aquatic environments is of great concern to human health due to the dual role of selenium as an essential trace micronutrient or as a toxic contaminant at elevated levels in the environment. Furthermore, the fate and distribution of selenium is altered by its oxidation state as evidenced by its variable solubility, stability, and toxicity.[1a] The fate and distribution of Se species is further complicated by the ability of selenite anions to form stable complexes with iron and aluminum oxides (Fe_2O_3, Al_2O_3), whereas; selenates do not form such complexes as evidenced by their greater bioavailability to plants after leaching from soils. Various inorganic and forms of selenium are known; selenide (Se^{2-}), selenite (Se^{4+}), and selenate (Se^{6+}). Selenate (SeO_4^{2-}) oxoanions are reduced to selenite (SeO_3^{2-}) anions under acidic conditions,[1b] however; SeO_3^{2-} species are more toxic and soluble in aqueous solution than SeO_4^{2-} species. The toxicological symptoms of selenium accumulation to human health are wide-ranging: hair loss, nail brittleness, skin rashes, irritability of eyes, disruption of the nervous and digestive system. The recommended dietary allowance (RDA) by the Institute of Medicine for selenium (55 µg Se/day) for male and female adults.[2,3]

The occurrence of selenium in wastewater supplies may often exceed the RDA value cited above and originates from industrial activities as reflected by the varying regulatory wastewater release standards for selenium. In Canada, the *Metal Mining Effluent Regulations* (MMER)[4] established limits on the release of arsenic, copper, cyanide, lead, nickel, zinc, radium-226 and total suspended solids. Recent reports indicate that metals/metalloid species such as As, Mo, Ni and Se coexist in the aqueous and solid phase tailings from uranium mines.[5] [Several countries have set upper threshold limits for Se in their drinking water quality guidelines (DWQG)[6]: 50 µg/L for the US-EPA and South Africa (Class 2), 20 µg/L for South Africa (Class 1), 10 µg/L for Canada, United Kingdom, Australia, European Union, New Zealand, and the World Health Organization.

Selenium removal can summarized by three categories of treatment: *i*) physical (e.g., reverse osmosis, nanofiltration, ion exchange, and evaporation), *ii*) chemical (iron reduction and precipitation, ferric coagulation and filtration, cementation, electrocoagulation, and photoreduction), and *iii*) biological (microbial reduction, and phytoremediation) treatment.[7] Adsorption is a versatile physical removal method because of its relatively low cost and it overall technological simplicity. Iron oxides and oxyhydroxides (magnetite, Fe_3O_4; maghemite, γ-Fe_2O_3; hematite, α-Fe_2O_3; goethite, α-FeOOH, etc.) and aluminum oxides/oxyhydroxides (activated alumina, γ-Al_2O_3 and gibbsite, $Al(OH)_3$) have been used for decades due to their high affinity for selenite species attributed to Lewis acid-base complexes.[8] For the general removal of metal cations, carbonaceous industrial adsorbents such as activated carbon (AC) represent a commonly used material. AC possess high surface area, microporosity, and amorphous structure with various surface functional groups such as carbonyl (-C=O) and hydroxyl (-OH), and heteroatoms such as oxygen, nitrogen, and sulfur.[9] The graphene surface and polar functional groups serve as electron donor systems that favour adsorptive interactions with metal cations *via* metal-pi complexes.[8]

The adsorption and catalytic properties of nanomaterials are of great interest due to their high *surface-to-volume* ratio, however; such systems have the potential disadvantage of exfoliation and leaching[10] due to their high chemical reactivity. Herein, we hypothesize that impregnation of magnetite nanomaterials onto carbonaceous supports such as AC may overcome these disadvantages since the resulting nanostructured composite material is stabilized within the pore structure and the extensive graphene surface of activated carbon. Lewis acid-base interactions between activated carbon (AC) and metal oxides may be employed as templates for the growth of nanoscale magnetite (Fe_3O_4) within the pores and onto the surface sites of AC to yield composite sorbent materials with unique physicochemical properties. In particular, we anticipate that composite materials of this type will display tunable adsorptive properties toward various inorganic and organic species in wastewater environments.

Herein, we report the equilibrium and kinetic sorption properties of supported and non-supported iron oxides (e.g., magnetite and goethite) with selenite in aqueous solution. The results of this study are compared with conventional materials (e.g., activated carbon and goethite) to obtain a greater understanding of the adsorptive properties of magnetite and its AC composites toward waterborne selenite species.

3.3 Experimental Section

3.3.1 Preparation of Magnetite, Goethite, and Composite Materials

The preparation and characterization of goethite, magnetite and magnetite composite with the activated carbon were adapted from procedures reported elsewhere.[11] Commercial magnetite was obtained from Sigma-Aldrich (nanopowder <50 nm). Briefly, magnetite was prepared by co-precipitation methods.[11] Briefly, 10 mL of 2.0 M $FeCl_2·4H_2O$ (98 %; Alfa Aesar) solution was prepared (4.0 g $FeCl_2·4H_2O$ in 2.0 M HCl). 10 mL of 1.0 M $FeCl_3·6H_2O$ (98 %; Alfa Aesar) solution was prepared (2.7 g $FeCl_3·6H_2O$ in 2.0 M HCl). In a 500 mL three-neck round bottom flask, 200 mL Millipore water was added with a magnetic stir bar and a dropping funnel containing 50 mL of 1.45 M NH_4OH (ACS grade from EDM) was maintained in an oil bath at 50 - 60 °C. To purge residual oxygen in the system, high purity argon (>99.9 %) gas was flushed for 5 min over the solution and for 10 min through the solution. 1.0 mL of 2.0 M $FeCl_2·4H_2O$ was added and followed by 4.0 mL of 1.0 M $FeCl_3·6H_2O$ with stirring. After 5 min., the basic solution was added drop-wise over 45 min. The final solution (pH 10-11) was stirred vigorously for 1 h and stirred additionally for 1 h at ambient temperature. The magnetite product was washed with Millipore water at ambient pH, followed by methanol washing and air drying, Final drying was carried out in a vacuum oven at ambient temperature overnight with an overall yield of 97.0%. A similar synthetic procedure of preparing magnetite-AC composites as above by adding 1.0 g of NORIT ROX 0.8 (as received from NORIT America) was added to the flask with Millipore water before adding $FeCl_2·4H_2O$ and $FeCl_3·6H_2O$ solution. By adjusting the molar ratio of $FeCl_2·4H_2O$ and $FeCl_3·6H_2O$ solution relative to the amount of AC. The weight ratio (w/w %) of magnetite in the AC composite was 19%. The preparation of nanoscale acicular goethite (α-FeOOH) was achieved by employing a 5/1 OH^-/Fe^{3+} molar ratio.[12] 10 mL of 4.0 M NaOH was added to 170 mL of Millipore water followed by 20 mL of 0.4 M $FeCl_3·6H_2O$. The mixture was stirred for 24 h at 30 °C and was continuously rinsed with Millipore water until the filtrate washings reached pH 7. The product was air dried for 12 h and subsequently in a vacuum oven for 2 h at 55 °C.

3.3.2 Equilibrium and kinetic sorption studies of selenite in aqueous solution

The detailed experimental conditions for the various sorption studies are listed in Table 3.1. Table 3.1 also defines the acronyms used to describe the various sorbent materials investigated in the equilibrium and kinetic studies. The Se species studied herein was sodium selenite obtained from Sigma-Aldrich and used without further purification. An aqueous solution of potassium phthalate buffer at 49 mM was used as the solvent system for selenite by adjusting the pH with NaOH to pH 5.26±0.02 at 22 °C. A stock solution (1000 ppm Se) of sodium selenite was prepared using phthalate buffer with appropriate dilutions in buffer (20 and 50 ppb for equilibrium and 20 and 200 ppb for kinetics). After shaking for the planned time for equilibrium and kinetics, the aliquots (5.0 mL) for the equilibrium and kinetic tests were sampled while the adsorbent particulates were separated *in-situ* from the sampling volume using a magnet in conjunction with an *in-situ* filter paper (Whatman #42) setup, as shown in Fig. 3.1. The residual equilibrium concentration (C_e; refer to eqn 3-1) of selenite species were analyzed with Hydride Generation Atomic Absorption Spectrophotometer (HGAA, novAA® 300, Analytik Jena Group) at λ_{ex} = 196.0 nm for determining the content of selenium. Calibration of the instrument was performed using a series of blank samples at concentrations matching the range of experimental conditions for kinetic and equilibrium studies.

Table 3.1. Experimental conditions for the sorptive uptake of selenite with magnetite (Mag-P and Mag-C), CM-19, AC, and goethite at pH 5.26 in phthalate buffer for 24 h.

Sample ID	**Adsorbents**	**T (°C)**	**Amount Sorbent (mg)**	**Selenite C_o (ppb)**	**Volume (L)**
Mag-P	Magnetite (prepared)	22[1]	1 - 80	20	0.010
Mag-C	Magnetite (commercial)	22[1]	1 - 80	20	0.010
CM-19	Magnetite 19%	22[1]	1 - 80	20	0.010
Goethite	Goethite	22[1]	1 - 80	50	0.010
Mag-P	Magnetite (prepared)	(5, 15, 22, 29, 39)[2]	150	20	0.500
Mag-C	Magnetite (commercial)	(5, 15, 22, 29, 39)[2]	150	20	0.500
CM-19	Magnetite 19%	(5, 15, 22, 29, 39)[2]	150	20	0.500
AC	NORIT ROX 0.8	(5, 15, 22, 29, 39)[2]	150	20	0.500
Goethite	Goethite	(5, 15, 22, 29, 39)[2]	100	200	0.500

[1] Selenite uptake at equilibrium (isotherm studies)

[2] Selenite uptake at variable time (kinetic studies)

Because magnetite and its composite adsorbents possess a measureable magnetic susceptibility besides activated carbon and goethite, the kinetic experiments used an overhead aluminum mixer. Fig. 3.1. illustrates the *in-situ* setup used for the selenium uptake experiments. To minimize evaporative losses during the uptake measurements, the device was covered using a sheet of aluminum foil during variable temperature (5 °C to 39 °C) studies.

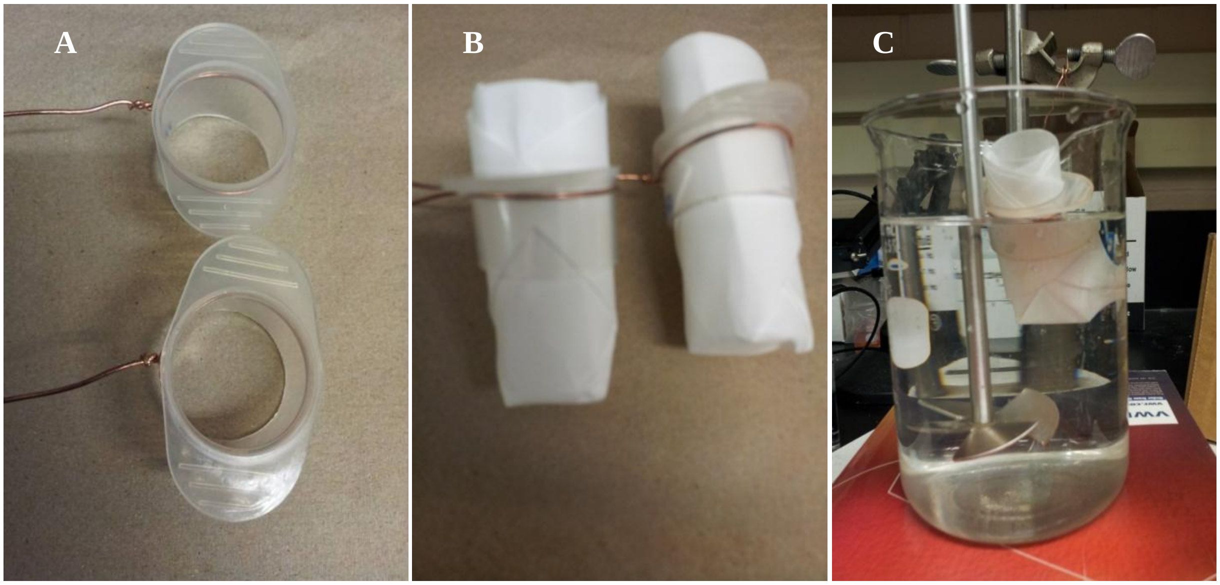

Figure 3.1. The experimental set-up for kinetic uptake experiments (A: Filter holder, B: *in-situ* filter, C: kinetic set-up using the aluminum mixer and the *in-situ* filter).

3.3.3 Sorption Models and Equations

The uptake of selenite by an adsorbent at the equilibrium (Q_e, mg/g) is calculated using the equation (3-1), where C_o (mol/L) is the initial concentration of the adsorbate, C_e (mol/L) is the equilibrium concentration of the adsorbate, V (L) is the volume of the adsorbate, and m is the mass (g) of the adsorbent. The monolayer adsorption capacity (Q_m) of the adsorbent with selenite (μmol/g) was obtained using the Sips isotherm model,[13] as shown in equation (3-2) because it adequately describes the empirical sorption results such as surface heterogeneities described by the Langmuir and Freundlich isotherm models, respectively.

$$Q_e = \frac{(C_o - C_e) \times V}{m} \tag{3-1}$$

$$Q_e = \frac{Q_m(K_S(C_e)^n)}{(1+K_S(C_e)^n)} \tag{3-2}$$

K_S is the Sips equilibrium constant and the value of n accounts for surface heterogeneities (when $n \neq 1$); whereas when $n = 1$, equation (3-2) reduces to the Langmuir equation. In this case, the Sips isotherm model overcomes the limitation of the Freundlich isotherm by providing estimates of Q_m that may be compared to those obtained from the Langmuir equation.

3.4. Results and Discussion

3.4.1 Sorption Equilibrium

The determination of the equilibration time for uptake of selenite in aqueous solution with various sorbents (magnetite, magnetic-AC composites, or AC) is shown in Fig. 3.2. The dosage of sorbent and the initial concentration of selenite (20 ppb, 0.010 L) was a fixed value at pH 5.26 in phthalate buffer and 22 °C. The equilibration time of selenite uptake was taken to be 24 h at these conditions. The magnetite (prepared) showed desorption after 24h.

Figure 3.2. Variation of selenite concentration against time for the sorptive uptake of selenite with various sorbents at pH 5.26 phthalate buffer at 22 °C for 24 h. (C_o: ~20 ppb, Volume: 0.010 L).

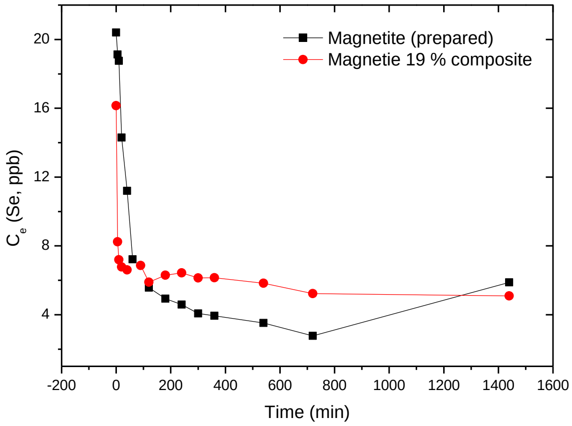

Note: 1. RSD of Magnetite (P): 4.0% (t = 0), 3.2% (t = 1440); the lowest RSD (LRSD) - 0.16% and the highest RSD (HRSD) - 4.0%.

2. RSD for Magnetite 19%: 2.2% (t = 0), 4.1% (t = 1440); LRSD (0.011%), HRSD (4.1%)

The equilibrium sorption results for selenite with Mag-P, Mag-C, CM-19, and goethite are shown in the Fig. 3.3 and Table 3.2. The maximum sorption removal capacity of selenite (Q_m = 18.3 μmol/g) was observed for the synthetic goethite sorbent. As the magnetite content in the composite materials decreased, the value of Q_m correspondingly decreased. The observed effect was attributed to adsorption onto the iron oxide sites since magnetite in the composite material is anticipated to interact favourably with selenite anions. The Fe-O sites of goethite, or magnetite and its composites provide π-electron acceptor domains suitable for the oxygen atoms (π-electron donor) of the selenite anion via Lewis acid-base interactions to form surface complexes by chelation.[14] Heterogeneous adsorption ($n > 1$; *cf.* eqn 3-2) was evidenced by multi-site binding of selenium on the surface of the composite adsorbent. However, the commercial magnetite displays ideal Langmuir behavior due to its greater chemical purity and more crystalline structure relative to Mag-P. AC did not show any significant sorption because the surface is apolar in nature and the overall coverage of surface bound polar functional groups is low.

Figure 3.3 The Sips sorption isotherm model for selenite with various adsorbent materials at pH 5.26 in phthalate buffer at 22 °C for 24 h. (C_o: ~20 ppb for Mag-P, Mag-C, and CM-19; whereas C_o ~200 ppb for goethite). Variable adsorbent weights (1~80 mg) with a total volume of 0.010 L, where C_o is the initial concentration of selenite.

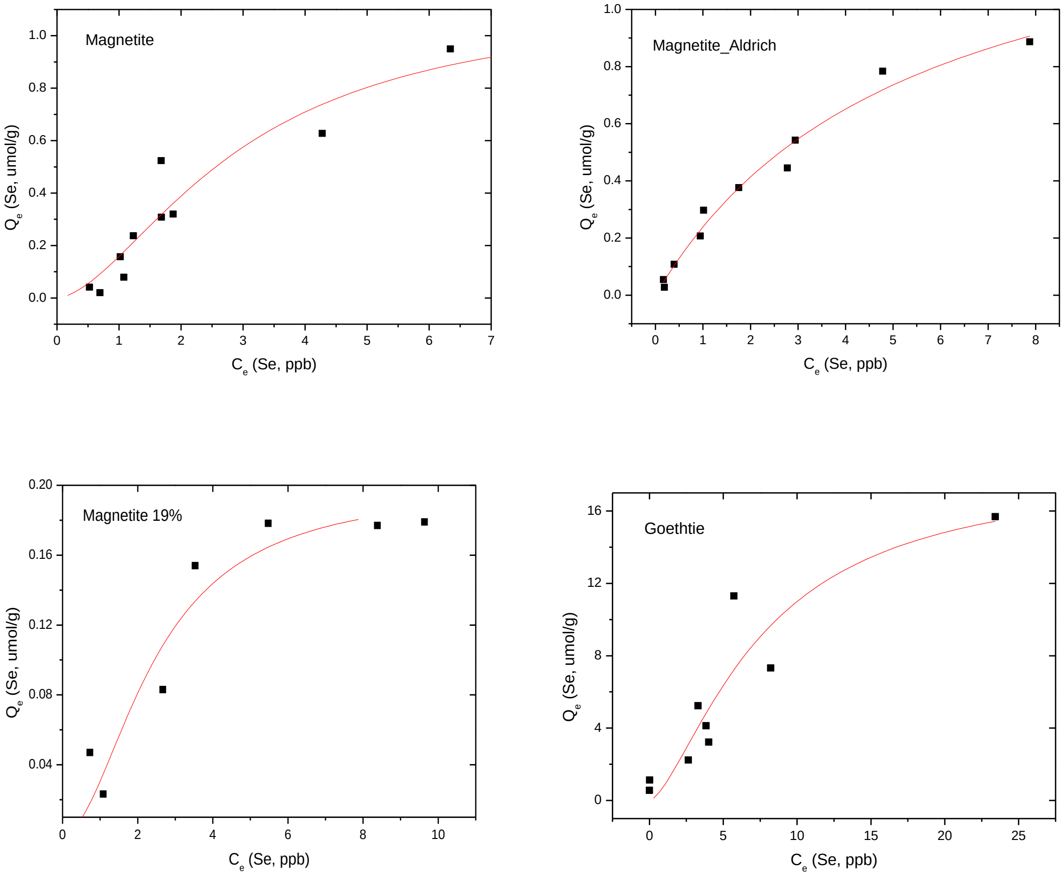

Note: 1. RSD for Magnetite-P: 0.86% at the low end of C_e to 3.2% in the high end of C_e. The highest one was 12.%.

2. RSD for Magnetite-C: 39.% at the low end of C_e to 2.4% in the high end of C_e

3. RSD for Magnetite 19%: 1.4% at the low end of C_e to 0.57% in the high end of C_e. The lowest one was 0.021% and the highest one was 6.9%.

4. RSD for goethite: 47.% at the low end of C_e to 0.025% in the high end of C_e

Increased sorption can be achieved by considering factors such as pH, buffer system, ionic potential of adsorbate, and the point of zero charge (pH_{pzc}) of the adsorbent. The advantage of employing buffer conditions instead of water at ambient pH is that the ionic strength and pH of the solution are maintained constant. If the concentration of buffer is higher than that of the adsorbate, the activity of the adsorbate goes to the unity.[15] Moreover, the occurrence of various protolytic forms of SeO_3^{2-} anions are controlled by the appropriate pH conditions. Another factor affecting sorption in solution is the right selection of pH, relative to pH_{pzc} of the adsorbent. The pH where the net surface charge of the adsorbent is zero is called pH_{pzc}. Thus, the pH conditions can be chosen to increase the sorptive uptake by maximizing the electrostatic attraction between the adsorbate and adsorbent by consideration of the pK_a value and the pH_{pzc} values of the adsorbent. If the solution pH is below the pK_a (adsorbate) and the pH_{pzc} (sorbent), the surface charge of the adsorbate and the adsorbent is positive or negative when the solution pH is above or below these pK_a and pH_{pzc} values, respectively. Accordingly, the sorptive uptake will be negligible. At the following pH conditions: $pK_a > pH > pH_{pzc}$, the surface charge of the adsorbate is positive, the adsorbent is negative, and favorable uptake occurs. By contrast, the following pH conditions: $pK_a < pH < pH_{pzc}$, the surface charge of the adsorbate is negative, the adsorbent is positive, and the maximum sorptive uptake occurs. An example of these effects was recently illustrated by Guo and Wilson for the adsorption of a cationic dye with chitosan-poly(acrylic acid) copolymers.[16]

Protolytic equilibria of various selenium species with variable pK_a values in aqueous solution are listed in Table 3.3. For example, the pK_a values of selenous and selenic acid are listed in Table 3.3.[17] Figure 3.4 illustrates the fractional abundance of various protolytic forms of selenium in aqueous solution.[17,18]

Table 3.2. The Sips sorption isotherm parameters for selenite with various adsorbent materials at pH 5.26 in phthalate buffer at 22 °C for 24 h. (C_o ~20 ppb for Mag-P, Mag-C, and CM-19; C_o ~200 ppb for goethite. Variable adsorbent weight (~1 to 80 mg) in a total volume of 0.010 L of selenite solution was employed.

Adsorbents	**Q_m (Se, μmol/g)**	**K_s**	**n**	**R^2**	**Chi^2/DoF**
Magnetite	1.13±0.48	0.163±0.068	1.68±0.77	0.904	1.09E-02
Magnetite (Aldrich)	1.52±0.05	0.187±0.067	1.01±0.19	0.982	2.05E-03
Magnetite 19%	0.200±0.033	0.181±0.112	1.92±0.80	0.916	5.70E-04
Goethite	18.3±7.3	0.0474±0.0486	1.50±0.95	0.852	4.97E+00

Table 3.3. pK_a values for selenium species at 25 °C and 1 bar pressure.

Equilibrium Species	pK_a
$H_2SeO_3 \rightleftharpoons HSeO_3^- + H^+$	2.63
$HSeO_3^- \rightleftharpoons SeO_3^{-2} + H^+$	8.40
$H_2SeO_4 \rightleftharpoons HSeO_4^- + H^+$	-3.00
$HSeO_4^- \rightleftharpoons SeO_4^{-2} + H^+$	1.70

The pH value at the point of zero charge (pH_{pzc}) for magnetite is estimated to be 6.5[18] and the pK_a values of selenite are 2.63 and 8.40.[17] The use of buffer below pH 6.5 can produce a net positive surface charge on magnetite, but selenite exists as a monoanion species at these conditions. Therefore, there is a strong electrostatic interaction between magnetite and selenite. In addition, the selenite anion may be coordinated in a bidentate fashion with iron (Fe^{3+}) species[19] at the interstitial void area of a tetrahedral site and at the octahedral site of magnetite for the cubic spinel structure[20] to produce an inner-sphere complex.[14a] An illustration of this surface complexation model is shown schematically in Fig. 3.5. There are different types of surface bound complexes: (**1**) an outer-sphere complex an ion-pair adsorption complex, (**2**) a solid solution of the selenite in the oxide phase, (**3**) and an adsorbed inner-sphere coordinate complex (bidentate-mononuclear complex, (**4**) monodentate-mononuclear complex, and (**5**) bidentate-binuclear complex. As the magnetite ratio in the composite decreases, the number of Lewis acid sites decrease and the sorptive uptake decreases due to reduced formation of inner-sphere surface complexes.

Figure 3.4. Selenium speciation and mole fraction versus pH in the solution for selenous acid (A) and selenic acid (B), according to the data in Table 3.3.

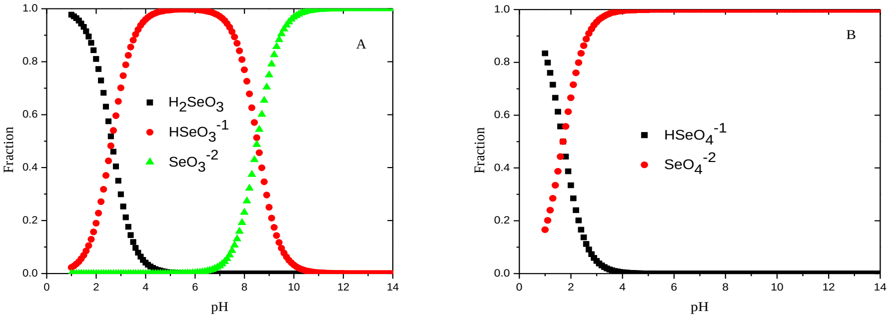

Figure 3.5. Proposed complexes for selenite adsorbed onto magnetite or its composites: (**1**) an outer-sphere ion-pair adsorption complex with the first hydration sphere shown as a dotted area, (**2**) a solid solution of the selenite in the oxide phase, and (**3-5**) inner-sphere complexes on the oxide surfaces. The oxide surface is the striped area below the line that represents the oxide-water interface.

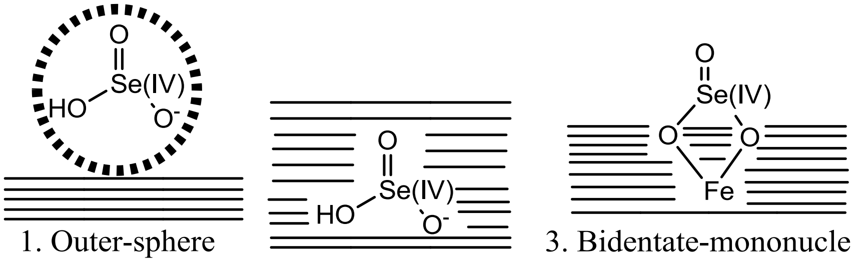

1. Outer-sphere surface complex

2. Solid solution

3. Bidentate-mononuclear inner-sphere surface complex

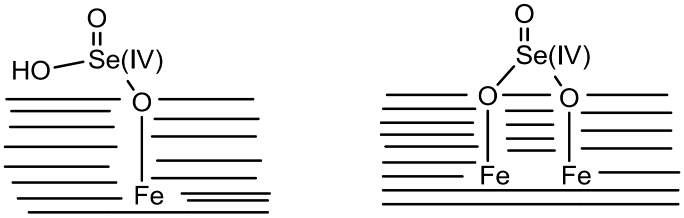

4. Monodentate-mononuclear inner-spher surface complex

5. Bidentate-binuclear inner-sphere complex

3.4.2 Sorption Kinetics

Fig. 3.6. illustrates the uptake kinetics for selenium (Q_e, Se mg/g) with magnetite, magnetite composites, and goethite. Table 3.4. lists the corresponding kinetic parameters. To determine the rate constant, a pseudo-first order (PFO) model (*cf.* eqn 3-3), originally proposed by Lagergren[21] and a pseudo-second order (PSO) model was employed (eqn 3-4), as proposed and developed by others.[22-24] The terms q_t (mg/g) refer to the temporal uptake of selenite by the adsorbent at time t, whereas; q_e (mg/g) is the uptake level of selenite by the adsorbent at equilibrium. The parameters, k_1 and k_2, are the rate constants (min^{-1} for PFO model and g mg^{-1} min^{-1} for PSO model). Integration of eqn (3-3) and (3-4) at the boundary conditions $q_t = 0$ at $t = 0$ and $q_t = q_t$ at $t = t$ with rearrangement affords the non-linear PFO equation (3-5) and the non-linear PSO (3-6), respectively.

$$\frac{dq_t}{dt} = k_1(q_e - q_t) \tag{3-3}$$

$$\frac{dq_t}{dt} = k_2(q_e - q_t)^2 \tag{3-4}$$

$$q_t = q_e(1 - e^{-k_1 t}) \tag{3-5}$$

$$q_t = \frac{k_2 {q_e}^2 t}{1 + k_2 q_e t} \tag{3-6}$$

To obtain the rate constant, PFO model was used because the value of root mean standard error (RMSE) of the PFO model was statistically lower than that of PSO model, as shown in Table 3.5.

Figure 3.6. The sorptive uptake kinetics for selenite (Q_e, Se mg/g) with various sorbents (Mag-P, Mag-C, CM-19, and AC), where C_o ~20 ppb, mass adsorbent = 0.150 g, V= 0.50 L). For goethite, C_o ~50 ppb, mass adsorbent = 0.100 g, V = 0.50 L) are shown at various temperatures at pH 5.26 in phthalate buffer over a 24 h interval.

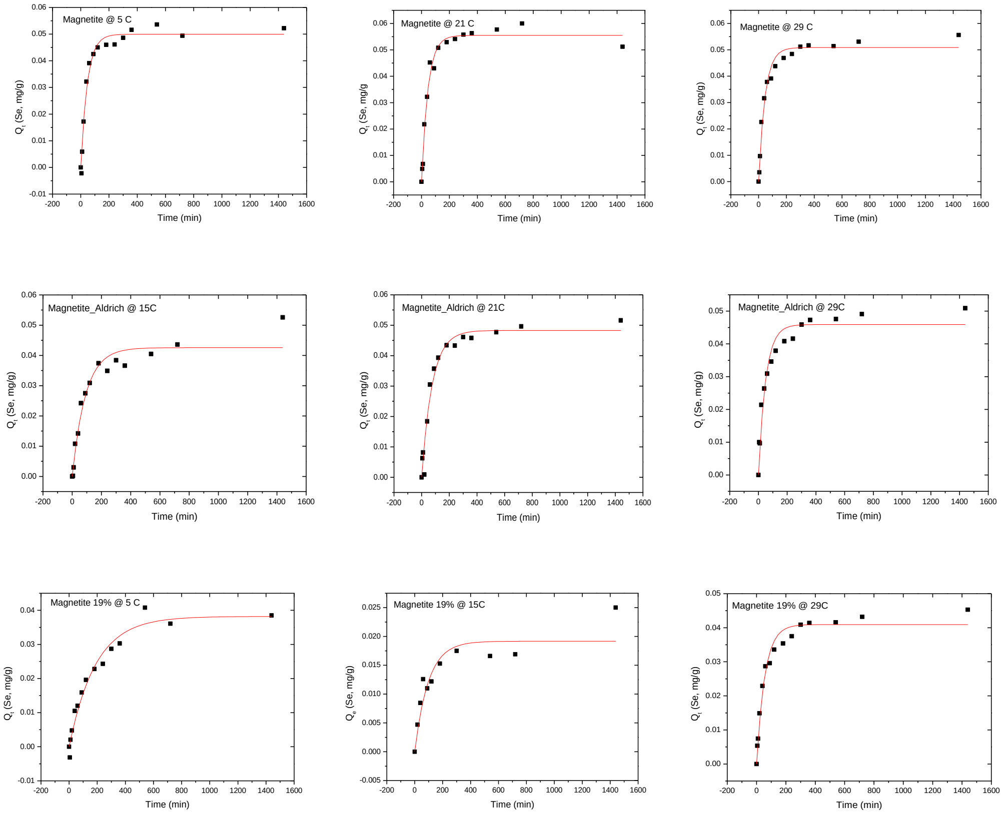

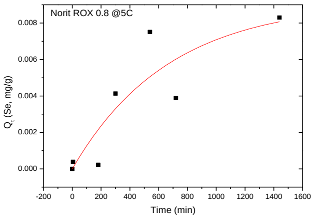

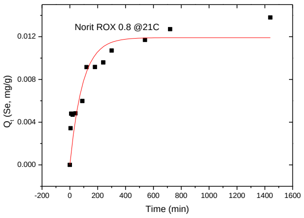

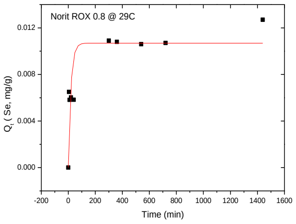

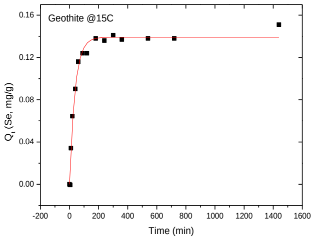

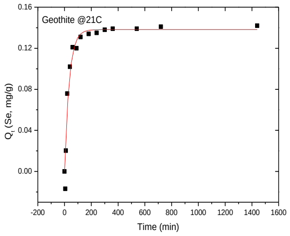

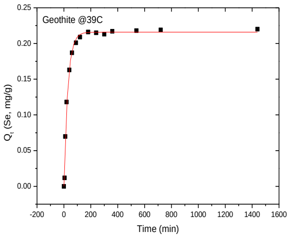

Note: RSD analysis

1. Magnetite-P at 5 °C: 1.6% (*t* = 0), 5.8% (*t* = 1440); LRSD (0.013%) and HRSD (6.7%)
2. Magnetite-P at 21 °C: 2.2% (*t* = 0), 2.8% (*t* = 1440); LRSD (0.0030%) and HRSD (4.3%)
3. Magnetite-P at 29 °C: 0.56% (*t* = 0), 1.4% (*t* = 1440); LRSD (0.078%) and HRSD (5.4%)
4. Magnetite-C at 15 °C: 1.7% (*t* = 0), 0.12% (*t* = 1440); LRSD (0.12%) and HRSD (7.5%)
5. Magnetite-C at 21 °C: 0.33% (*t* = 0), 0.82% (*t* = 1440); LRSD (0.22%) and HRSD (6.9%)
6. Magnetite-C at 29 °C: 2.0% (*t* = 0), 0.63% (*t* = 1440); LRSD (0.42%) and HRSD (3.5%)
7. Magnetite 19% at 5 °C: 2.5% (*t* = 0), 2.8% (*t* = 1440); LRSD (0.0030%) and HRSD (4.6%)
8. Magnetite 19% at 15 °C: 1.3% (*t* = 0), 3.2% (*t* = 1440); LRSD (0.57%) and HRSD (5.7%)
9. Magnetite 19% at 29 °C: 1.6% (*t* = 0), 0.22% (*t* = 1440); LRSD (0.22%) and HRSD (1.8%)
10. NORIT ROX 0.8 at 5 °C: 0.30% (*t* = 0), 1.7% (*t* = 1440); LRSD (0.037%) and HRSD (2.1%)
11. NORIT ROX 0.8 at 21 °C: 4.2% (*t* = 0), 1.8% (*t* = 1440); LRSD (0.055%) and HRSD (4.2%)
12. NORIT ROX 0.8 at 29 °C: 2.3% (*t* = 0), 1.8% (*t* = 1440); LRSD (0.048%) and HRSD (2.4%)
13. Goethite at 15 °C: 2.3% (*t* = 0), 7.6% (*t* = 1440); LRSD (0.84%) and HRSD (10.%)
14. Goethite at 21 °C: 1.2% (*t* = 0), 12.% (*t* = 1440); LRSD (0.076%) and HRSD (12.%)
15. Goethite at 39 °C: 3.0% (*t* = 0), 20.% (*t* = 1440); LRSD (0.92%) and HRSD (37.%)

Table 3.4. PSO kinetic sorption parameters for selenite uptake by sorbent materials at variable temperature at pH 5.26 in phthalate buffer for 24 h.

Adsorbents	**T (°C)**	**Q_e (Se; μg/g)**	**k_{obs} (min^{-1})$\times10^{-3}$**	**R^2**	**Chi^2/DoF**
Mag-P[1]	5	55.6±0.7	25.6±1.5	0.992	3.57×10^{-6}
	21	55.5±1.1	21.7±1.9	0.982	8.84×10^{-6}
	29	50.9±1.1	21.7±2.0	0.979	7.97×10^{-6}
Mag-C[1]	15	42.6±1.8	11.0±1.6	0.953	1.00×10^{-5}
	21	48.3±1.6	13.1±1.6	0.966	1.00×10^{-5}
	29	45.9±1.4	19.9±2.6	0.953	1.00×10^{-5}
CM-19[1]	5	38.2±1.6	5.29±0.60	0.973	6.06×10^{-6}
	15	19.2±1.9	10.3±3.2	0.853	1.00×10^{-5}
	29	40.9±1.0	17.8±1.8	0.974	6.35×10^{-6}
AC[1]	5	9.13±3.6	1.49±1.1	0.790	3.03×10^{-6}
	21	11.9±0.9	11.0±3.1	0.817	3.35×10^{-6}
	29	10.7±0.9	53.0±2.0	0.728	4.49×10^{-6}
Goethite[2]	15	139±3	26.6±2.3	0.983	5.00×10^{-5}
	21	138±4	29.0±4.4	0.955	1.50×10^{-4}
	39	216±3	35.0±2.2	0.991	6.00×10^{-5}

[1] Refers to C_o(selenite) ~20 ppb, adsorbent dosage = 0.150 g, and V= 0.50 L

[2] Refers to C_o(selenite) ~50 ppb, mass adsorbent = 0.100 g, and V=0.50 L

Table 3.5. Comparison of RMSE values of PFO and PSO models for selenite adsorption with sorbents at variable temperature at pH 5.26 in phthalate buffer for 24 h.

Adsorbents	**5 °C**		**22 °C**		**29 °C**	
	PFO	**PSO**	**PFO**	**PSO**	**PFO**	**PSO**
Mag-P^1	1.04×10^{-2}	7.38×10^{-1}	2.76×10^{-3}	7.25×10^{-1}	2.63×10^{-3}	7.40×10^{-1}
	15 °C		**22 °C**		**29 °C**	
	PFO	**PSO**	**PFO**	**PSO**	**PFO**	**PSO**
Mag-C^1	3.54×10^{-3}	7.26×10^{-1}	3.39×10^{-3}	7.15×10^{-1}	4.95×10^{-3}	7.30×10^{-1}
	5 °C		**15 °C**		**29 °C**	
	PFO	**PSO**	**PFO**	**PSO**	**PFO**	**PSO**
CM-19^1	2.29×10^{-3}	7.25×10^{-1}	3.46×10^{-3}	5.75×10^{-1}	2.35×10^{-3}	7.32×10^{-1}
	5 °C		**22 °C**		**29 °C**	
	PFO	**PSO**	**PFO**	**PSO**	**PFO**	**PSO**
AC^1	3.82×10^{-3}	4.68×10^{-1}	3.32×10^{-3}	5.30×10^{-1}	3.20×10^{-3}	4.73×10^{-1}
	15 °C		**22 °C**		**39 °C**	
	PFO	**PSO**	**PFO**	**PSO**	**PFO**	**PSO**
Goethite^2	6.57×10^{-3}	7.28×10^{-1}	1.13×10^{-2}	6.91×10^{-1}	6.99×10^{-3}	6.89×10^{-1}

[1] Refers to C_o(selenite) ~20 ppb, mass adsorbent = 0.150 g, and V= 0.50 L

[2] Refers to C_o(selenite) ~50 ppb, mass adsorbent = 0.100 g, and V = 0.50 L

In a chemical process, the observed rate constant (k_{obs}) in the Arrhenius relation (eqn 3-7) and the elementary single-step rate constant (k_{obs}) in the Eyring equation (eqn 3-8) are dependent on temperature (T). Strictly speaking, the Arrhenius equation is applicable for gas phase processes, but the Eyring equation can be applied to both gas and condensed phases. In the Eyring equation, the rate constant k is related to the Gibbs energy of activation ($\Delta G^{\ddagger}$) and is comprised of an enthalpy of activation ($\Delta H^{\ddagger}$), and the entropy of activation ($\Delta S^{\ddagger}$). The Eyring equation relates the rate constant for a process and the thermodynamic (i.e. entropy and enthalpy) parameters of activation according to transition-state theory. Comparing these two rate constant equations reveals that E_a relates to $\Delta H^{\ddagger}$ and the pre-exponential factor (A) to $\Delta S^{\ddagger}$ by the

Arrhenius equation.[25] Kinetic parameters such as the activation energy (E_a, kJ mol^{-1}) and thermodynamic terms such as the change in enthalpy ($\Delta H^{‡}$, kJ mol^{-1}), change in entropy change ($\Delta S^{‡}$, J mol^{-1}K^{-1}), and the change in Gibbs energy ($\Delta G^{‡}$, kJ mol^{-1}) were obtained using the Eyring relation (eqn 3-8). The physicals constants k_B, h, and R are the Boltzmann, Plank's, and universal gas constant, respectively. The Eyring plots are shown in Fig. 3.7, where $\Delta H^{‡}$ and $\Delta S^{‡}$ are calculated from the linear regression parameters (*cf.* eqn 3-8; slope ($-\Delta H^{‡}/R$) and the *y*-intercept $(\frac{\Delta S^{‡}}{R})$) for a plot of $ln\left(\frac{kh}{k_B T}\right)$ against T^{-1} (K^{-1}), according to kinetic results in Table 3.4. $\Delta G^{‡}$ and E_a are related by the following: $\Delta G^{‡} = \Delta H^{‡} - T\,\Delta S^{‡}$; and $\Delta H^{‡} = E_a - RT$ (solution phase). Table 3.6. lists the corresponding parameters.

$$\ln(k_{obs}) = \frac{-E_a}{RT} + \ln A \qquad (3\text{-}7)$$

$$\ln\left(\frac{k_h}{k_B T}\right) = \frac{-\Delta H^{\neq}}{RT} + \frac{\Delta S^{\neq}}{R} \qquad (3\text{-}8)$$

Figure 3.7. Eyring plots for selenite uptake with Mag-P, Mag-C, CM-19, and AC (C_o ~20 ppb, adsorbent dosage: 0.150 g, V= 0.50 L) and with goethite (C_o ~50 ppb, adsorbent dosage= 0.100 g, V= 0.50 L) at variable temperature at pH 5.26 in phthalate buffer for 24 h.

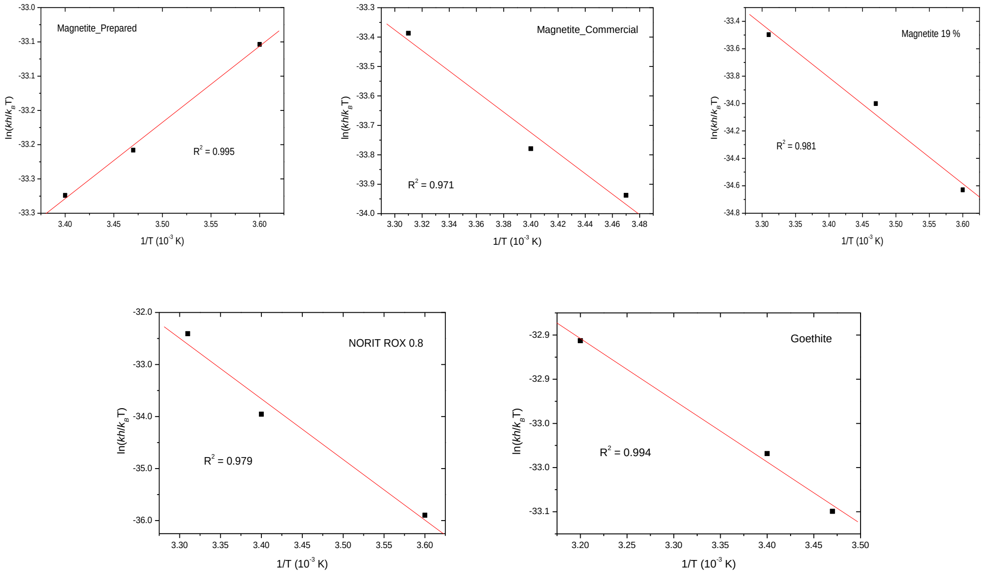

As shown in Table 3.4, the overall rate constant (k_{obs}) of Mag-P decreased as the temperature increased resulting in an *apparent* negative E_a with a more negative $\Delta H^{\ddagger}$ due to the increased activation barrier for the sorption process. Other examples of negative E_a have been reported elsewhere such as the separation process of pentlandite from the monosulfide solid solution,[25]and an elementary gas-phase reaction which forms an intermediate complex.[26,27] As well, negative E_a was reported for simple bimolecular metathesis reactions and for rapid reactions.[28] However, other adsorbents showed that their overall rate costants (k_{obs}) increased as the temperature increased, in agreement with a positive E_a and $\Delta H^{\ddagger}$ due to a decreased activation barrier. In addition, the rate law of kinetic results for the observed sorption processes may be interpreted based on the relative polarity of the adsorbent surface sites. All adsorbent surfaces are polar in nature with the exception of activated carbon. Since selenite is polar and relatively hydrohilic in nature, the value of rate constant for the adsorptive process follows a descending order according to the dipolar nature of the sorbent surface: goethite > Mag-P > Mag-C > CM-19 > AC. The greater rate constant of activated carbon at 29 °C may be assisted by thermal diffusion processes. Therefore, selenite may diffuse through the boundary layer of goethite fastest as shown by the largest rate constant. As the magnetite content decreased, the rate constant also decreased, in agreement with the decreasing polarity of adsorbent surface. Mag-P was more polar than that of Mag-C becasue the surface area differed by a factor of two. This difference is accounted for by the formation of more Fe species in the tetrahedral and octahedral sites.

The relationship between the values of $\Delta H^{\ddagger}$ and E_a are consistent with the magnitude of the rate constant. The results are in good agreement with the general rule that lower values of $\Delta H^{\ddagger}$ and E_a reflect processes with faster rates of reaction, and vice versa. Considering the values of Q_e, k_{obs}, E_a, and $\Delta H^{\ddagger}$ shown in Tables 3.4 and 3.6, the trend of k_{obs}, E_a, and $\Delta H^{\ddagger}$ was obeyed. The following general trend in uptake parameters was observed for selenite with the various sorbent materials: [$\mathbf{Q_e}$: Goethite > Mag-P > Mag-C > CM-19 > AC]; [$\boldsymbol{k_{obs}}$: Goethite > Mag-P > Mag-C > CM-19 > AC]; [$\mathbf{E_a}$: Mag-P < Goethite < Mag-C < CM-19 < AC]; and [$\boldsymbol{\Delta H^{\ddagger}}$: Mag-P < Goethite < Mag-C < CM-19 < AC].

With regard to the sorptive uptake (Q_e; mg/g) of selenite derived from the kinetic results, the values were in good agreement with thermodynamically driven proceses. Sorptive uptake increased as the temperature increaseed for an endothermic processes, while sorptive uptake decreased for an exothermic processes as the temperature increased. The strong negative contribution of the $\Delta S^{\ddagger}$ (-0.2 to -0.3 J/mol K) could be explained on account of the transformation of an activated complex to an inner-sphere complex. The relatively weak but positive contribution for $\Delta S^{\ddagger}$ (0.1 J/mol K) for the formation of the activated complex for AC may involve an outer-sphere selenite-water hydrate complex with several degrees of freedom arising from translation, rotation, and vibration.

Table 3.6. PFO kinetic and thermodynamic sorption parameters for selenite with Mag-P, Mag-C, CM-19, and AC (C_o ~20 ppb, mass adsorbent = 0.150 g, V= 0.50 L) and goethite (C_o ~50 ppb, mass adsorbents = 0.100 g, V= 0.50 L) at various temperatures at pH 5.26 in phthalate buffer for 24 h.

	ΔH‡ (kJ/mol)	**ΔS‡ (J/mol K)**	**T (K)**	**ΔG‡ (kJ/mol)**	**E_a (kJ/mol)**
Mag-P	-9.47	-309	278	76.4	-7.16
			294	81.4	-7.04
			302	83.9	-6.96
Mag-C	28.8	-182	288	81.4	31.2
			294	82.5	31.3
			302	83.9	31.3
CM-19	32.6	-170	278	80.0	35.0
			288	81.7	35.0
			302	84.1	35.2
AC	98.50	54.9	278	83.2	101
			294	82.4	101
			302	81.9	101
Goethite	5.89	-254	288	79.2	8.28
			294	80.7	8.33
			312	85.3	8.48

Table 3.7 Literature survey of various adsorbent materials and the sorptive removal of Se(IV) from aqueous solution.

Adsorbents	**Sorption conditions (${C_o}$ in [Se^{4+}])**	**Removal (Se^{4+}, mg/g)**	**References**
2-line ferrihydrite	pH 7, 22±2 °C for 24 h, C_o: 75 µM, 2 g/L mineral	2.42	29
hematite		0.861	
goethite		2.90	
mackinawite (FeS)	pH 7-10, 44 h, C_o: 20 mL of 127 - 253 µM, 0.5 g/L FeS	61.6-174	30
TiO_2 (anatase)	pH 3.00, 23±2 °C, 3 h, C_o: 5.89-589 µM, 5 g/L anatase	0.675-0.979	31
Mg/Al/Cl LDH	pH 1.9-10.6, 25 °C, 4h, 100 mL of aqueous C_o: 290 µM, 1g/L layered double hydroxide (LDH)	119.	32
Zn/Al/Cl LDH		123.	
Aluminum oxide coated sand	pH 2-12.5, 8 h, C_o: 50 mL of 0-1.8 mM, 5 g/L aluminum oxide coated sand	0.560-1.05	33
Tropical soil	PH 3-7, 24 h, C_o: 200 µM, 5% soil/solution	0.0813-0.145	34
Mg-Al LDH	PH 7, 12 h, C_o: 25 mL of 250 mM containg 200 mg LDH	203.	35
Zn-Al LDH		160	
Iron-oxide-coated sand (IGCS)	pH 6.5, 20 °C 36 h, C_o: 100 ml of 126 µM containing 10 g IGCS	1.11-1.34	36
Iron-coated granular AC (Fe-GAC)	pH 5, 25-45 °C, 48 h, C_o: 25-50 mL of 25µM, 2-3 g/L Fe-GAC	2.58 (equilibrium) 0.637 (kinetic)	37
Al(III)/SiO_2	pH 5, 25 °C, 24 h, C_o: 0-3 mM	14.9 (equilibrium) 10.3 (kinetic)	38
Fe(III)/SiO_2		9.31	

		(equilibrium) 7.57 (kinetic)	
Goethite	pH 7.6, 50 h, C_o: 20 mL of 20 µM containing 0.1 g goethite	0.520	39
Hematite	pH 7.2, 50 h, C_o: 20 mL of 20 µM containing 0.1 g goethite	0.390	
Magnetite	pH 4, 30 h, C_o: 20 mL of 3-500 µM containing 0.1 g magnetite	0.220	40
Rice husk	pH 1.5, 25 °C, 200 h, C_o: 50 mL of 633 µM containing 0.1 g rice husk	26.5	41
Fe_3O_4 nano-materials	pH 4, 5-60 min, C_o: 4 mL of 260µM containing 0.01 g Fe_3O_4 nano-materials	2.38	42
FeOOH	pH 5, 24h, C_o: 100 mL of 0.006-253 µM containing 0.05 g FeOOH	26.3	43
Mag-P	Equilibrium pH 5.26 buffer, 24 h, 22 °C, C_o: 0.555µM (others), 5.55 µM (goethite),	0.0894 (equilibrium) 0.0556 (kinetic)	This study
Mag-C	V: 0.0100 L Mass: 1-80.0 mg Kinetic	0.120 (equilibrium) 0.0483 (kinetic)	
CM-19	pH 5.26 buffer, 24 h, 5-39 °C, C_o: 0.555 µM (others), 1.39 µM (goethite), V: 0.500 L	0.0158 (equilibrium) 0.0409 (kinetic)	
AC	Mass: 0.100 g/L (goethite), 0.150 g/L (others)	Nil (equilibrium) 0.0119 (kinetic)	
Goethite		1.44 (equilibrium) 0.216 (kinetic)	

Table 3.7 provides a literature survey of examples for the sorptive uptake of Se(IV) species by various adsorbent materials. The sorptive removal results reported herein may not compare well with those in Table 3.7 due to the use of different experimental conditions such as the initial Se(IV) concentration or adsorbent dosage. Upon consideration of the sorptive removal based on considering the relative concentration of Se(IV) reveals that the values for Q_e reported herein study showed the highest level of sorptive removal, especially in the case of goethite.

When selenite is adsorbed to the surface of iron oxide/oxyhydrate, a modifed triple-layer model (TLM) may be applied to account for this surface complexation process.[43] In this model, the adsorbed iron can be bound to both the α-layer to form an inner-sphere complex and the β-layer to form an outer-sphere surface complex.[44] [In solution at pH 5.26, selenite is the major ion ($HSeO_3^-$) as shown in Table 3.3 and Fig. 3.4, and may be present as the monodentate-mononuclear inner-sphere surface (S) complex ($S\text{-}HSeO_3^0$), according to Scheme 3.1. Scheme 3.1 shows the bulk phase of reactants, the first transition complex between the protonated and hydrated iron oxide surface with the hydrated selenite ion. As well, the intermediate, the second transition complex between the iron oxide, selenite, and water, along with the adsorbed monodentate-mononuclear inner-sphere surface complex. The active site of iron oxide/oxyhydrate is a reversible surface complex. If the soluton is maintained at pH 11, the monodentate-mononuclear inner-sphere surface complex will be desorbed completely. However, at solution of $8.4 < pH < 11$, a possible two-step mechanism of the protonated selenite monoanion ($HSeO_3^-$) and the divalent selenite dianion (SeO_3^{2-}) species for this surface process are shown in Scheme 3.2. In the first step, the complex $S\text{-}OH_2^+\text{-}HSeO_3^-$ and $S\text{-}OH_2^+\text{-}SeO_3^{2-}$ are the outer-sphere surface complexes in the β-layer. In the second step, $S\text{-}HSeO_3^0$ and $S\text{-}SeO_3^-$ represent the inner-sphere surface complexes of the α-layer through a ligand-exchange process.[44]In Scheme 3.2, k_1, k_2, k_3, k_4 are the adsorptive rate constants, k_{-1}, k_{-2}, k_{-3}, k_{-4} are the desorptive rate constants, whereas; K_5 and K_6 are the equilibrium constants for the protolytic equilibria of the various complexes.[44]

Scheme 3.1 Proposed reaction coordinate diagram for the adsorption process of selenite on the surface of iron oxide/oxyhydrate at pH 5.26.

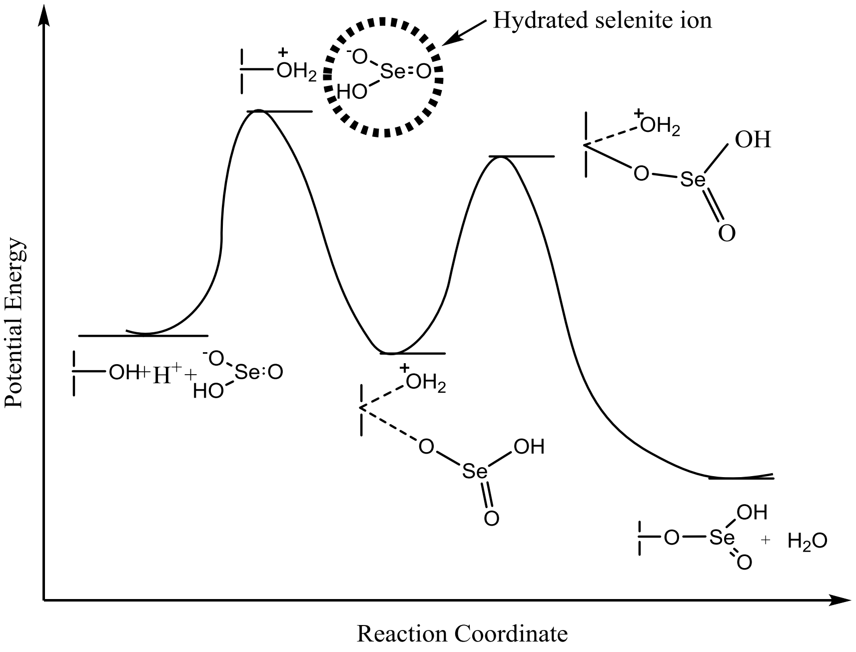

Scheme 3.2 The proposed adsorption mechanism of selenite on the surface of iron oxide/oxyhydrate: A) pH 5.26, B-1) 8.4 < pH < 11 for the protonated selenite anion and B-2) 8.4 < pH < 11for the divalent selenite anion. The vertical bar represents the surface of iron oxide/oxyhydrate, where -OH represents the active surface site of iron oxide/oxyhydrate.

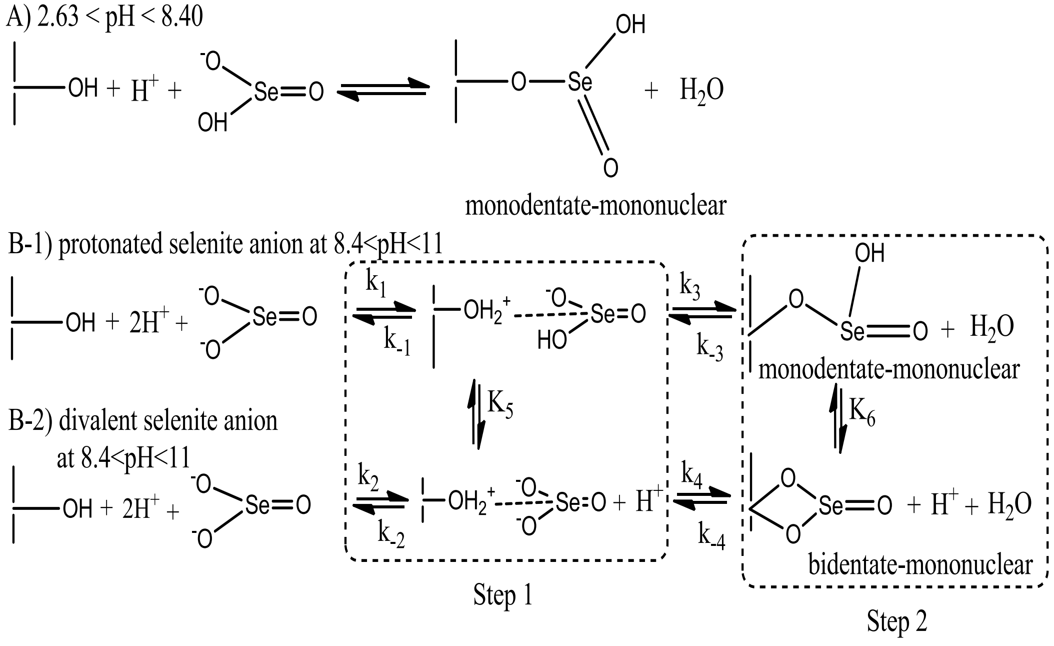

The occurrence leaching of Fe species are reported elsewhere for iron oxide materials.[45] Therefore, the iron leaching properties were studied herein to evaluate the stability of iron oxides in AC composite materials, and the results are shown in Fig. 3.8 and Table 3.8. Activated carbon showed the increased Fe dissolution at 21°C due to higher thermal diffusion of Fe dissolution than the sample at lower temperatures. Magnetite and its composite showed more leaching effect at lower temperature than higher temperature. The leaching effect may be more pronounced with the composites at elevated temperature due to their weak interaction between magnetite and the surface of activated carbon. By contrast, magnetite showed more Fe leaching than the composites due to its high surface energy and reactivity than its composites. Because magnetite particles were impregnated either within the pores sites or on the external surfaces of the activated carbon, Fe leaching was apparently reduced at 5 °C and 15 °C, due to reduced solvent accessibility. The ratio of coverage of magnetite within the pores and onto the surface sites of AC is estimated to be ~2:1. Therefore, magnetite particles were readily leached from the surface, and less readily leached from the pore sites. As temperature increased, greater thermal energy contributed to greater Fe leaching from the activated carbon, as compared with the magnetite materials. For example, AC showed noticeable Fe leaching at 22°C, whereas; nearly negligible leaching occured at 5 °C and 15 °C. In the case of goethite, the tendency of Fe leaching was proportional to the temperature change. The amount of Fe leached exceeded one of the magnetite composites due to its different crystal structure (crystal system: orthorhombic, space group: Pbnm (62) and hardness (5-5.5 by Mohs hardness) from magnetite (crystal system: cubic, space group: Fd3m (227), Mohs hardness 5.5-6.5).[46]

Table 3.8 Comparison of Fe leaching rate (%) among activarted carbon, magnetite, and magnetite 19% composite at different temperature.

Adsorbent	**Mass (g)**	**Fe content**	**Fe leach, max (μg)**			**Fe leach rate, max (%)**		
			5 °C	**15 °C**	**21 °C**	**5 °C**	**15 °C**	**21 °C**
Magnetite	0.150	0.677	528.	532.	28.2	0.520	0.523	0.028
Mag19% composite	0.150	0.211	152.	44.3	59.7	0.479	0.140	0.189
Activated carbon	0.150	0.00768	0	0	19.9	0	0	1.73

Figure 3.8 Fe leaching results from magnetite (Mag-P, Mag-C), CM-19, and AC (C_o: ~20 ppb, mass adsorbents= 0.150 g, V= 0.50 L), and goethite (C_o: ~50 ppb, mass adsorbent= 0.100 g, V= 0.50 L) at various temperatures at pH 5.26 in phthalate buffer for 24 h.

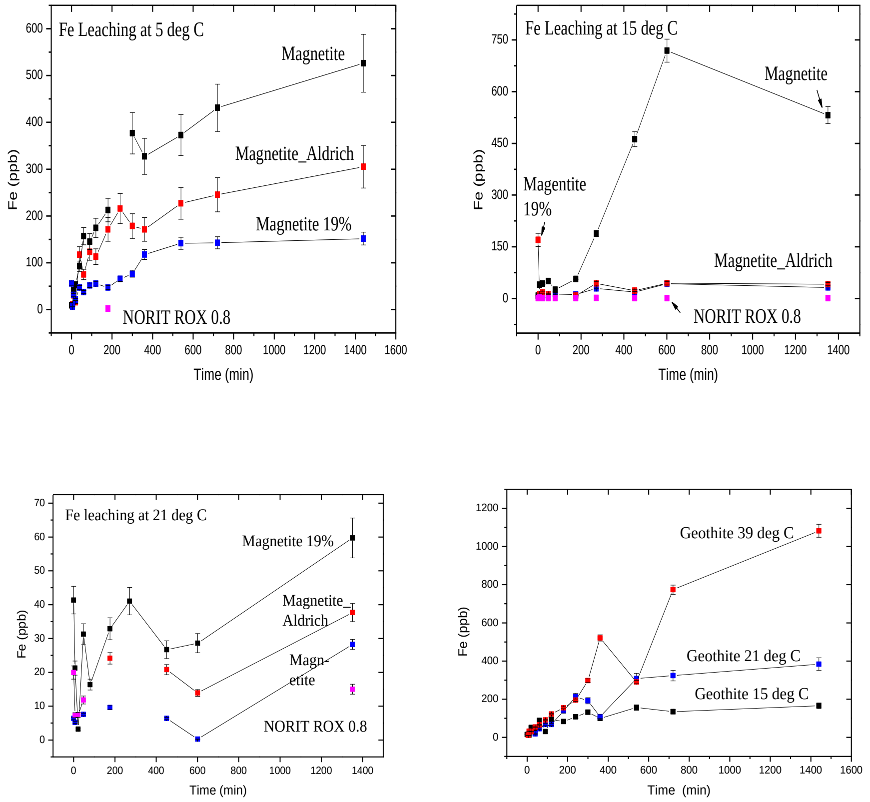

3.5. Conclusion

Equilibrium and kinetic studies for the uptake of selenite was studied using a one-pot *in-situ* in house experimental setup developed herein. This study showed that goethite provided the highest sorptive uptake followed by Mag-P, Mag-C, magnetite composite (CM-19), and AC. Mag-P showed an *apparent* negative E_a and $\Delta H^{\ddagger}$ due to contributions from hydration processes or composite kinetic steps that could not be explicitly accounted for using simple transition-state theory. Mag-C, CM-19, AC, and goethite showed a positive value for E_a and $\Delta H^{\ddagger}$. The value of $\Delta S^{\ddagger}$ for AC showed a positive value suggesting that bond breaking occurs during the sorptive process to the transition state. Fe leaching was dramatically reduced by impregnating magnetite within the pores and onto the surfaces of activated carbon, especially at temperatures below 293 K. At 295 K, the composite (CM-19) showed the highest Fe leaching due to the increased liberation of magnetite particles from the pores or surface of activated carbon. In the case of goethite, Fe leaching was proportional to the temperature change. Magnetite composites with activated carbon display reduced iron leaching at lower temperatures. Therefore, magnetite composites with reduced iron leaching offer advantages in various wastewater treatment processes in concert with magnetic separation[47] of the solid and solution phases for large-scale industrial processing.

3.6. Acknowledgments

The authors acknowledge NORIT America Inc. for the provision of research samples of activated carbon. The University of Saskatchewan and the Natural Sciences and Engineering Research Council of Canada are gratefully acknowledged for supporting this research.

3.7 References

1. a) M. Ihnat, In Occurrence & Distribution of Selenium, CRC Press, Boca Raton, Fl., 1989, and b) G.A. Cutter. Anal. Chim. Acta, 98 (1978) 59.

2. World Health Organization. Trace Elements in Human Nutrition and Health; World Health Organization: Genova, Swiss, 1996**,** p 119

3. Panel on Dietary Antioxidants and Related Compounds, Subcommittees on Upper Reference Levels of Nutrients and Interpretation and Uses of DRIs, Standing Committee on the Scientific Evaluation of Dietary Reference Intakes, Food and Nutrition Board, Institute of Medicine. Dietary Reference Intakes for Vitamin C, Vitamin E, Selenium and Carotenoids. National Academy Press: Washington, D.C., USA, 2000, p 284

4. http://laws-lois.justice.gc.ca/eng/regulations/SOR-2002-222/ (accessed 25/05/2013)

5. S.A. Shaw, M.J. Hendry, J. Essilfie-Dughan, T. Kotzer, D. Wallschlager. Appl. Geochem., 26 (2011) 2044.

6. G. Gilron. Integr. Environ. Assess. Manag., 8 (2012) 194.

7. Golder Associates Inc. Literature review of treatment technologies to remove selenium from mining influenced water. 2009, 08-1421-0034 Rev. 2. pp. 9-24.

8. M. Vaclavikova, G.P. Gallios, S. Hredzak, S. Jakabsky. Clean. Tech. Env. Policy, 10 (2008) 89.

9. J.H. Kwon, L.D. Wilson. J. Environ. Sci. Health. A, 45 (2010) 1775.

10. a) T.E.A. Chalew, K.J. Schwab. Water & Health. 2012. March 7 online issue. and b) H. Ramezani-Dakhel, P.A. Mirau, R.R. Naik, M.R. Knechtc, H. Heinz. Phys. Chem. Chem. Phys., 15 (2013) 5488.

11. P. Berger, N.B. Adelman, K.J. Beckman, D.J. Campbell, G.C. Lisensky, A.B. Ellis. J. Chem. Ed., 76 (1999) 943.

12. G. Montes-Hernandez, F. Renard, R. Chiriac, N. Findling, J. Ghanbaja, F. Toche. Chem. Eng. J., 214 (2013) 139.

13. R. Sips. J. Chem. Phys. 16 (1948) 490.

14. a) K.F. Hayes, A.L. Roe, G.E. Brown Jr., K.O. Hodgson, J.O. Lecknie, G.A. Parks. Science, 238 (1987) 783. and b) W. Stumm. *In* Chemistry of the solid-water interface: processes at the mineral-water and particle-water interface in natural systems. John Wiley & Sons: New York, USA, 1992; pp. 21-22.

15. F.J. Hingston, R.J. Atkinson, A.M. Posner, J.P. Quirk. Trans. 9th Int. Congr. Soil. Sci. 1 (1968) 669.
16. R. Guo, L.D. Wilson. J. Colloid. Interface. Sci., 388 (2012) 225.
17. M.S. Dzul Erosa, W.H. Höll, J. Horst. React. Funct. Polym., 69 (2009) 576.
18. N. Takeno. Intercomparison of thermodynamic databases. Geological Survey of Japan Open File Report No.419; National Institute of Advanced Industrial Science and Technology: Ibaraki, Japan, 2005, p. 229-231.
19. G. Parks. Chem. Rev., 65 (1965) 177.
20. T.J. Bastow, A. Trinchi. Solid State Nucl. Mag., 35 (2009) 25.
21. S. Lagergren. Kungliga Svenska Vetenskapsakademiens Handlingar, 24 (1898) 1.
22. G. Blanchard, M. Maunaye, G. Martin. Water Res., 18 (1984) 1501.
23. Y.S. Ho. Dissertation for the Doctoral Degree, University of Birmingham, Birmingham, 1995.
24. S. Azizian. J. Colloid Interface Sci., 276 (2004) 47.
25. K. Tampouris, A.L. Petrou. Hell. J. Geosci., 45 (2010) 299.
26. M. Mozurkewich, S.W. Benson. J. Phys. Chem., 88 (1984) 6429.
27. M. Mozurkewich, J.J. Lamb, S.W. Benson. J. Phys. Chem., 88 (1984) , 88, 6435.
28. S.W. Benson, O. Dobis. J. Phys. Chem. A., 102 (1998) 5175.
29. K. Mitchell, R-M. Couture, T.M. Johnson, P.R.D. Mason, P. Van Cappellen. Chem. Geol., 342 (2013) 21.
30. D.S. Han, B. Batchelor, A. Abdel-Wahab. J. Hazard. Mater., 186 (2011) 451.
31. K. Shi, X. Wang, Z. Guo, S. Wang, W. Wu. Colloids Surf. A., 349 (2009) 90.
32. S. Mandal, S. Mayadevi, B.D. Kulkarni. Ind. Eng. Chem. Res., 48 (2009) 7893.
33. W.H. Kuan, S.L. Lo, M.K. Wang, C.F. Lin. Water Res., 32 (1998) 915.
34. K.H. Goh, T.T. Lim. Chemosphere, 55 (2004) 849.
35. Y. You, G.F. Vance, H. Zhao. Appl. Clay Sci., 20 (2001) 13.
36. S.L. Lo, T.Y. Chen. Chemosphere, 35 (1997) 919.
37. N. Zhang, L.S. Lina, D. Gang. Water Res., 42 (2008) 3809.
38. Y.T. Chan, W.H. Kuan, T.Y. Chen, M.K. Wang. Water Res., 43 (2009) 4412.
39. M. Rovira, J. Gimenez, M. Martinez, X. Martinez-Llado, J. de Pablo, V. Marti, L. Duro. J. Hazard. Mater., 150 (2008) 279.

40. M. Martinez, J. Gimenez, J. de Pablo, M. Rovira, J. Duro. Appl. Surf. Sci., 252 (2006) 3767.

41. E.I. El-Shafey. J. Hazard. Mater., 147 (2007) 546.

42. C.M. Gonzalez, J. Hernandez, J.R. Peralta-Videa, C.E. Botez, J.G. Parsons, J.L. Gardea-Torresdeya. J. Hazard. Mater., 211-212 (2012) 138.

43. M.O. Sharrad, H. Liu, M. Fan. Sep. Purif. Technol., 84 (2012) 29.

44. P. Zhang, D.L. Sparks. Env. Sci. Technol. 24 (1990) 1848.

45. E. Matei, C. Predescu, A. Berbecaru, A. Predescu, R. Trusca. Digest Journal of Nanomaterials and Biostructures, 6 (2011) 1701.

46. R. C. Weast, M. J. Astle. *In* CRC Handbook of Chemistry and Physics. 63rd Ed., CRC Press Inc, Florida, USA. 1982, pp. B204-B205, B218.

47. C.M. Babu; B. Palanisamy; B. Sundaravel; M. Palanichamy; V. Murugesan, J. Nanosci. Nanotech., 13 (2013) 1.

CHAPTER 4

MANUSCRIPT 3

Description

The sorptive uptake of roxarsone as a representative of aryl toxic metal with iron oxide composites on an activated carbon support was described in the verbatim manuscript submitted for publication in a peer reviewed journal entitled Materials (materials-47936), as presented in Chapter 3. Roxarsone may contaminate soil and surface water supplies through the uncontrolled use of poultry litter as a fertilizer additive. Degradation of roxarsone in the environment may result in the formation of more toxic inorganic forms of arsenic (arsenite and arsenate). Therefore, there is a need to investigate novel adsorbent materials of the type described in Chapters 2-3 for the physical removal of roxarsone-contaminated wastewater and soil environments.

Authors' Contribution

I carried out all experimental work, data analysis, and the first draft of the manuscript. Supervision of the research and subsequent editing of the manuscript was carried out by me and my principal supervisor (Lee D. Wilson). Recrystallization of the raw roxarsone from Haohua Industry Co. Ltd. (Jinan City, China) was aided by a summer student (Lewis Casey) and with some assistance on equilibrium adsorption experiments. I carried out the kinetics and equilibrium studies along with data analysis and interpretation.

Relation of Chapter 4 to the overall objectives of this project

This work was related to the research hypothesis as described in section 1.2 in Chapter 1. Reactive surface functional groups such as metal cations are able to bind anion species in aqueous solution via formation of surface complexes. Therefore, the adsorbent materials described in Chapters 2 were studied to evaluate their adsorptive behavior toward an anion form of an organoarsenical using equilibrium and kinetic-based sorption experiments.

Graphical Abstract

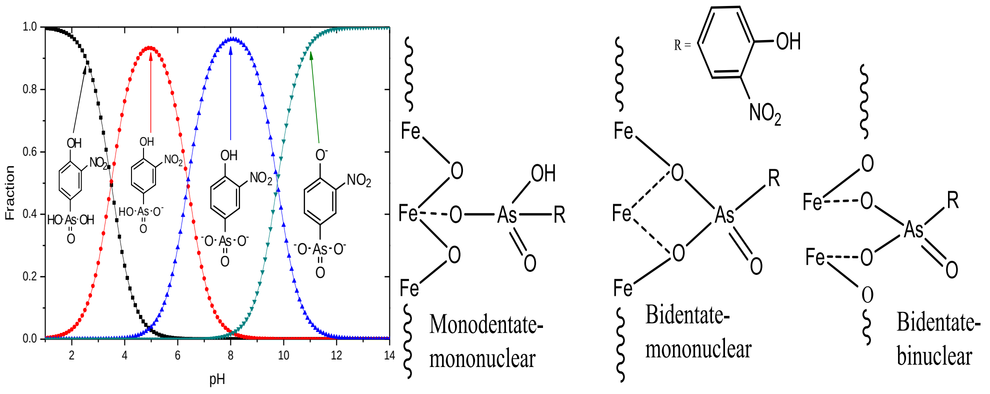

Research Highlights

The equilibrium and kinetic uptake studies for various adsorbents were obtained and the results revealed that NORIT ROX 0.8 provided the most favourable overall adsorption, followed by goethite, magnetite 10%, magnetite 19%, magnetite 32%, magnetite-P, and magnetite-C. The decreasing sorptive uptake paralleled the trend in the decreased activated carbon content of the adsorbent materials. The adsorbed roxarsone species on the surface of the iron oxide/oxyhydrate were inferred as inner-sphere surface complexes of monodentate-mononuclear, bidentate-mononuclear, and bidentate-binuclear depending on the type of ionic speciation of roxarsone.

4. SORPTIVE UPTAKE STUDIES OF ARYLARSENICAL WITH IRON OXIDE COMPOSITES ON AN ACTIVATED CARBON SUPPORT

Jae H. Kwon[1], Lee D. Wilson[1*], R. Sammynaiken[2]

[1]University of Saskatchewan, 110 Science Place, Saskatoon, SK., S7N 5C9 Canada;
[2]Saskatchewan Structural Science Centre, University of Saskatchewan, 110 Science Place, Saskatoon, SK S7N 5C9 Canada

***** Author to whom correspondence should be addressed; E-Mail: lee.wilson@usask.ca;
Tel.: +1-306-966-2961; Fax: +1-306-966-4730

4.1 Abstract

Sorption kinetics and equilibrium studies for the sorptive uptake of 4-hydroxy-3-nitrobenzene arsenic acid (roxarsone) was evaluated with magnetite-P (Prepared), magnetite-C (Commercial), magnetite 10%, 19%, and 32 % composite containing granular activated carbon with (GAC), and goethite at pH 7.00 in aqueous phosphate buffer at 21 °C for 24 h. GAC showed the highest removal efficiency for roxarsone. The relative uptake of roxarsone for each sorbent material is listed in descending order as follows: GAC (471 mg/g) > goethite (418 mg/g) > magnetite 19% (254 mg/g) > magnetite 32 % (227 mg/g) > magnetite-P (132 mg/g) > magnetite-C (29.5 mg/g). The As (V) moiety of roxarsone is adsorbed on the surface of the iron oxide/oxyhydrate are inferred as inner-sphere surface complexes of monodentate-mononuclear, bidentate-mononuclear, and bidentate-binuclear depending on the protolytic speciation of roxarsone. The phenyl ring of roxarsone provides the driving force for the sorptive interaction with the graphene surface of GAC and its composites. Thus, magnetite composites are proposed as multi-purpose adsorbents for the removal of inorganic and organic arsenicals due to the presence of graphene and iron oxide sites.

Keywords: roxarsone; arylarsenical; magnetite; goethite; activated carbon; adsorption

4.2 Introduction

Arsenic species occur naturally in surface water such as rivers, lakes, reservoirs, and ponds by the natural processes of soil erosion, mineral leaching, volcanic deposits, and geochemical weathering processes.[1] Anthropogenic inputs to the atmosphere through mineral smelting operations, fossil-fuel combustion, and consumption of organic arsenicals by poultry contribute to the overall fate and distribution of arsenic: geological and anthropogenic activities (e.g., $(CH_3)_3As$, $As_4O_{6(s)}$, $As_4O_{10(s)}$) → water pollution → soil and sediments → bioaccumulation.[2] Arsenic has variable oxidation states in the environment 3-, 0, 3+, and 5+), particularly in aquatic environments where the speciation depends on the relative redox potential and the pH conditions.[3] Common forms of arsenic are the oxyanions of arsenite (As^{3+}) or arsenate (As^{5+}),[3] where the latter is the most thermodynamically stable form in surface water environments. Arsenite is relatively stable under mild reducing conditions in anoxic ground waters and is considered the more thermodynamically stable form.[3] In most natural waters, arsenic (III) occurs as the non-ionized form of arsenous acid (H_3AsO_3, $pK_a = 9.22$) and may interact weakly with most solid surfaces.[4] Depending on the pH and oxidizing conditions, the efficient isolation of various protolytic forms of arsenic(III) species with traditional treatment methods such as adsorption, precipitation, etc., represents a technological challenge.[4] Roxarsone (4-hydroxy-3-nitrobenzenearsonic acid) and arsanilic acid (4-aminophenylarsonic acid) as shown in Fig. 4.1 are arylarsenicals used as food additives to promote the weight gain of swine and poultry, and to control microbial infections. Roxarsone may contaminate soil and surface water supplies through the uncontrolled use of poultry litter as a fertilizer additive.[5,6] Roxarsone partially degrades *via* metabolic pathways in poultry and in land which may result in the formation of more toxic inorganic forms of arsenic (arsenite and arsenate) in the environment.[7-10]

Figure 4.1. Molecular structure of roxarsone with its pK_a values in aqueous solution

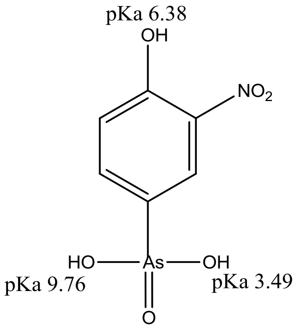

Arsenic contamination of drinking water has been highlighted because of its toxicity and variable occurrence.[11] Several countries such as Bangladesh, New Zealand, USA, Italy, and Malaysia are facing serious water security due to high-arsenic levels in their drinking source water supplies.[12] The World Health Organization (WHO) has established international health standards for arsenic in drinking water as10 ppb to minimize the risks of arsenic exposure.[12] The importance of arsenic in wastewater was recognized in Canada by the establishment of guidelines in the mining industry, as evidenced by the *Metal Mining Effluent Regulations* (MMER).[13] As of 2010, Canadian mining industries are required to adhere to the release limits on various species; arsenic, copper, cyanide, lead, nickel, zinc, radium-226, and total suspended solids. In northern Saskatchewan, reports indicate that metals such as As, Mo, Ni and Se are found in the liquid and solid tailings of various mine sites.[14] Activated carbon is a microporous amorphous material with relatively high surface areas and surface functional groups with heteroatoms such carbonyl (C=O), hydroxyl (-OH), amine ($-NH_2$), and thiol (-SH), depending on the oxidizing conditions.[15] These functional groups may serve as electron donors (Lewis base) and may contribute to form metal-pi interactions with metal cations (Lewis acid) on the surface of granular activated carbon (GAC) and on its basal planes. The pores of GAC offer surface adsorption sites which may also serve as a template site for the growth of magnetite in the case of supported composite materials.[16] Arsenic removal has been applied by various technologies: aeration, chlorination, sedimentation, precipitation/co-precipitation, adsorption, ion exchange, membrane separation including microfiltration, reverse osmosis, electrodialysis, ultrafiltration, and nanofiltration, and biological processes.[12] Among the various methods, adsorption is a versatile method because of its relatively low cost and applicability to a wide range of waterborne contaminants depending on their chemical nature.[12] Recent studies have illustrated the utility of biomaterial-based adsorbents for arsenate anion removal in aqueous solution.[17,18] Similarly, iron oxide-based materials and their composites are versatile adsorbents due to the high affinity of such materials to inorganic arsenicals.[12,19] For example, the removal metal cations and their oxyanions from wastewater employs iron oxides and oxyhydroxides (magnetite, Fe_3O_4; maghemite, γ-Fe_2O_3; hematite, α-Fe_2O_3; goethite, α-FeOOH, etc.), and aluminum oxides/oxyhydroxides (activated alumina, γ-Al_2O_3 and gibbsite, $Al(OH)_3$). Such types of inorganic adsorbents have been used for decades due to their low cost and relatively high affinity[19] toward inorganic arsenicals. One limitation of inorganic adsorbents is the potential leaching of the framework; magnetite-graphene or magnetite-zeolite are examples[19b-c] of magnetite-based nanomaterials because of the release iron species due to the high surface-to-volume ratio of such sorbents. Thus, there is a need to investigate adsorbents with favourable binding affinity toward arsenicals whilst minimizing leaching of the framework during adsorptive processes.

The removal of roxarsone and its inorganic degradation products requires a multi-purpose adsorbent material with dual binding affinity toward inorganic and aryl arsenicals whilst minimizing the aforementioned leaching problems. We hypothesize that composite adsorbents with dual binding affinity toward roxarsone and its degradation products (i.e. inorganic and aryl arsenicals) represent suitable materials for the sorptive removal of such arsenicals from contaminated wastewater and soil environments. Herein, we report an adsorption study of roxarsone in aqueous solution with composite materials containing activated carbon and iron oxide at variable composition. The adsorptive properties of the composites are compared with activated carbon and two types of iron oxides (i.e. magnetite and goethite) toward roxarsone. Although roxarsone undergoes chemical decomposition as a feed additive, it remains largely unchanged (~80%).[7-10] Therefore, this sorptive study is focused on the equilibrium and kinetic uptake properties of various adsorbent materials toward roxarsone in aqueous solution.

4.3 Results and Discussion

4.3.1 *Sorption Isotherms*

Calibration curves of roxarsone were obtained using UV-Visible absorption spectroscopy as shown in Fig. 4.2. The molar absorptivity (ε) of roxarsone at pH 7.00 was 27.3×10^3 $LM^{-1}cm^{-1}$ at $\lambda = 244$ nm, in agreement with an independent estimate for roxarsone ($\varepsilon = 22.9 \times 10^3$ $LM^{-1}cm^{-1}$) at $\lambda = 224$ nm.[20] The spectral bands at 400 nm and 244 nm arise from electronic transitions of $S_o \rightarrow S_1$ (n-π*: first HOMO → first LUMO) and of $S_o \rightarrow S_2$(π-π*: second HOMO → second LUMO), respectively.

The initial experimental conditions employed roxarsone ($C_o = 0.24$ mM, V = 0.020 L) at pH 7.00 in phosphate buffer at 21 °C for 4, 22, 43, 96 h with 200 rpm shaking as shown in Fig. 4.3, where C_o is the initial concentration of roxarsone. The time required to reach sorptive equilibrium for roxarsone with commercial magnetite (Aldrich) exceeded 20 h. According to Fig.

4.3, an equilibration time used herein for the sorption of roxarsone was 24 h for a sample amount of 15 mg of adsorbent at these experimental conditions. The use of higher dosage levels of adsorbent for the isotherm studies minimizes the random errors related to sample weight and residual levels of unbound adsorbate (C_e), as evidenced by the trend in absorbance changes.

Figure 4.2. UV-Visible absorption spectrum of roxarsone (A) and a Beer-Lambert calibration curve (B) at pH 7.00 in phosphate buffer (10 mM) at 244 nm

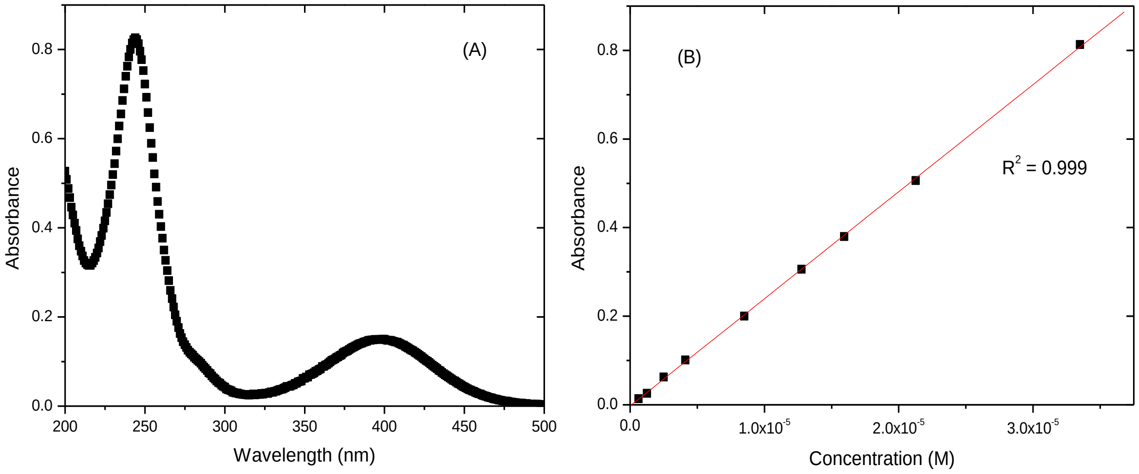

The sorptive uptake results at isotherm conditions for roxarsone with synthetic magnetite (magnetite-P), commercial magnetite (magnetite-C), activated carbon-magnetite composites with variable magnetite (32%, 19%, and 10%; w/w%), and goethite are shown in the Fig. 4.4 and Table 4.1. The maximum monolayer adsorption capacity of roxarsone (Q_m = 1.783 mmol/g) was achieved with activated carbon. Although activated carbon contains a relatively low intrinsic level of Fe content[15] as an impurity during its synthetic preparation, the sorptive removal of roxarsone is attributed to noncovalent interactions such π-π stacking and H-bonding between the phenyl ring of roxarsone and the graphene surface of activated carbon. In the case of composite materials, the Q_m value of roxarsone increased as the content of the activated carbon content increased, as anticipated for adsorptive processes influenced by the hydrophobic effect. By contrast, the iron oxide components such as magnetite, goethite, and the magnetite composites are anticipated to function as π-electron acceptor (Lewis acid) sites due to the presence of iron species on the adsorbent surface, especially for inorganic arsenate.[12,19] As well, favourable Lewis acid-based interactions may contribute to the formation of coordination complexes on the iron oxide surface because complexes between Fe species and the oxygen atoms of the roxarsone anion.[21,22] Adsorption of roxarsone on the heterogeneous surface sites of magnetite (10% and 19%) are supported by the exponent parameter (*n* > 1) from the Sips isotherm modeling. Commercial magnetite showed Langmuir adsorption behaviour (n=1) because it is a relatively uniform and homogeneous surface.

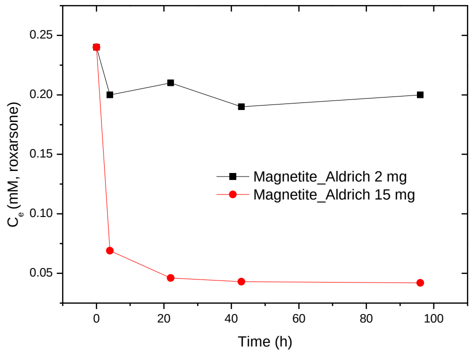

Figure 4.3 The sorptive equilibration of roxarsone (C_o: 0.24 mM, V = 0.020 L) with commercial magnetite (Aldrich) at pH 7.00 in phosphate buffer at 21 °C against time Error of C_e for 2 mg (0.4% at *t* = 0 to 0.004% at *t* = 96 h) and for 15 mg (0.4% at *t* = 0 to 0.0006% at *t* = 96 h)

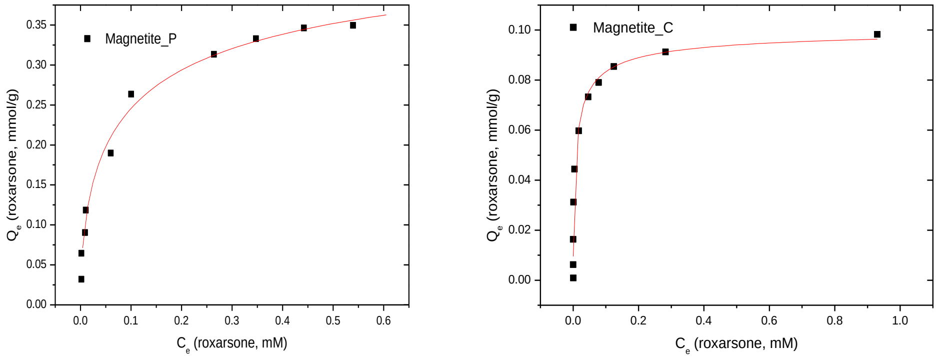

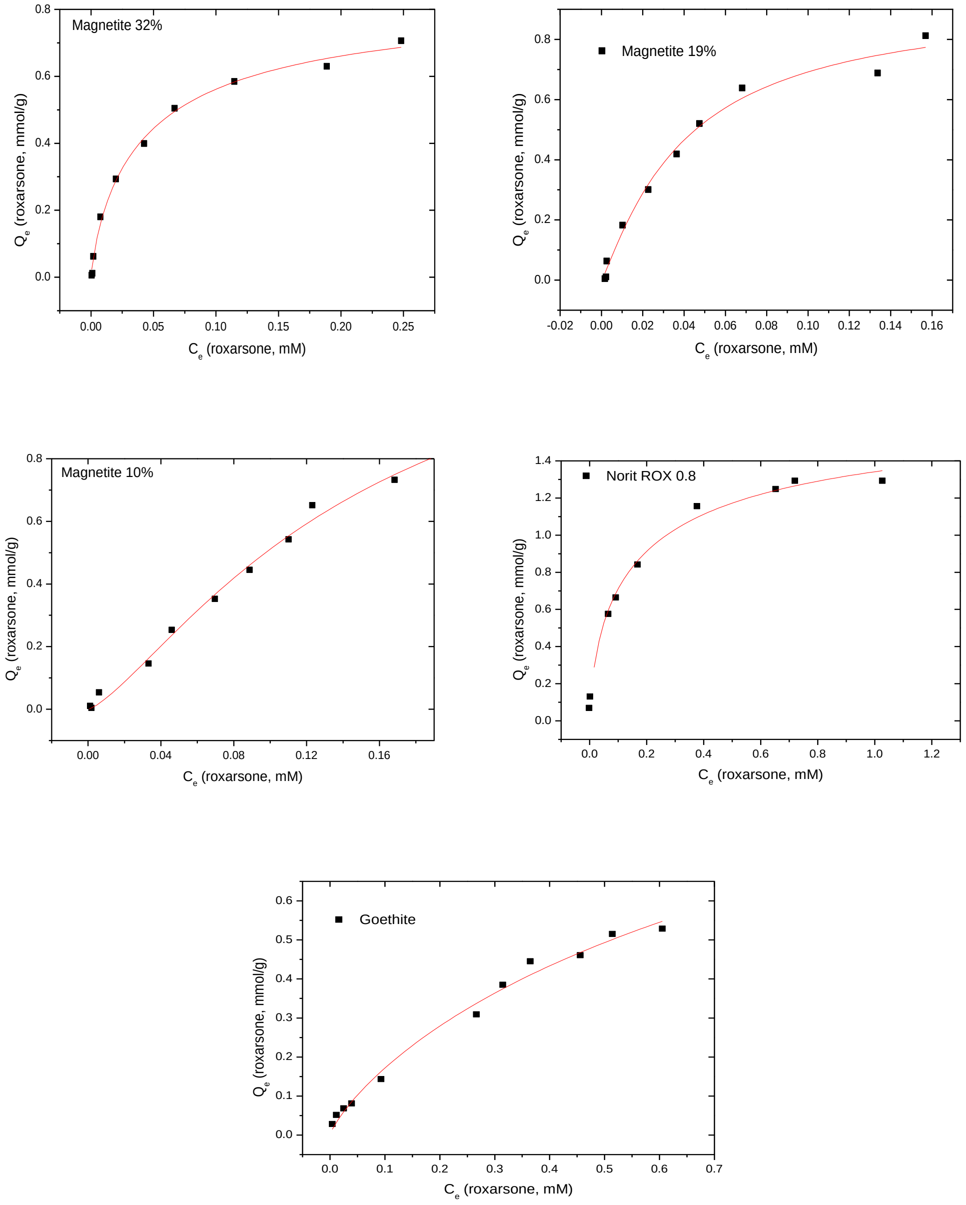

Figure 4.4 The Sips isotherm fitting results for the adsorption of roxarsone with the magnetite-P, magnetite-C, magnetite 32%, magnetite 19%, magnetite 10%, GAC, and goethite at pH 7.00 phosphate buffer at 21 °C for 24 h. (adsorbent dosage: ~ 15 mg; C_o (0.025 ~ 1.0 mM); V = 0.020 L). Errors (Q_e, ± mmol/g) from the low end (C_e) to the high end (C_e): Magnetite-P (1.67×10^{-7} - 1.02×10^{-5}), Magnetite-C (9.55×10^{-6} - 1.12×10^{-5}), Magnetite 32% (1.06×10^{-2}-1.93×10^{-1}), Magnetite 19% (2.31×10^{-7} - 8.43×10^{-6}), Magnetite 10% (1.23×10^{-2} - 2.13×10^{-1}), NORIT ROX 0.8 (3.14×10^{-7} - 1.77×10^{-5}), Goethite (1.77×10^{-7} - 9.43×10^{-6})

Table 4.1 Sips isotherm fitting parameters for roxarsone with adsorbent materials at pH 7.00 in phosphate buffer at 21 °C. (Adsorbent mass: ~ 15 mg; C_o (0.025 ~ 1.0 mM); V = 0.020 L)

Adsorbents	**Q_m (mmol/g)**	**K_s**	***n***	**R^2**	**Chi^2/DoF**
Magnetite-P	0.500±0.089	3.50±2.14	0.559±0.092	0.989	2.30E-04
Magnetite-C	0.102±0.009	19.3±14.3	0.624±0.111	0.972	4.00E-05
Magnetite 32%	0.862±0.070	12.1±5.4	0.813±0.084	0.996	3.90E-04
Magnetite 19%	0.936±0.105	39.7±34.9	1.15±0.20	0.989	1.29E-03
Magnetite 10%	1.39±0.48	12.9±14.5	1.34±0.26	0.992	7.10E-04
NORIT ROX 0.8	1.78±0.35	3.04±2.16	0.661±0.168	0.991	2.88E-03
Goethite	1.59±1.06	0.792±0.837	0.815±0.143	0.991	4.70E-04

Note: Chi^2/DoF is a diagnostic goodness of fit parameter.

The equilibrium uptake (Q_e, mg/g) of an adsorbent toward an adsorbate is calculated using equation (4-1). C_o is the initial concentration (M) of the adsorbate, C_e is the equilibrium concentration (M) of the adsorbate, *V* is the volume (L) of the adsorbate, and *m* (g) is dosage level of the adsorbent employed. The monolayer adsorption capacity of roxarsone (Q_m; mmol/g) was obtained using the Sips model,[23] as shown by equation (4-2), because it accounts for the empirical adsorption results that describe surface heterogeneity or homogeneity, described Freundlich or Langmuir isotherm models.

$$Q_e = \frac{(C_o - C_e) \times V}{m} \tag{4-1}$$

$$Q_e = \frac{Q_m K_S C_e^n}{1 + K_S C_e^n} \tag{4-2}$$

K_s is the Sips equilibrium constant and the exponent term, *n*, describes the sorbent surface heterogeneity that characterize multiple adsorption sites. When *n* is very low, eqn 4-2 reduces to Freundlich equation. The Sips isotherm model provides a general description of various types of monolayer adsorption, both the Freundlich (n> 1) and Langmuir (n=1) models, whilst providing an estimate of Q_m. The Sips model is empirically based and it is valid only up to a certain concentration, while a linear relationship between Q_e and C_e occurs at low concentration,[24] as predicted by eqn 4-2. Heterogeneous adsorption can be observed when n> 1, as evidenced by multi-site adsorption at surface sites on the adsorbent through inner-sphere complexation, outer-sphere complexes, π-π stacking, or H-bonding interactions.

The sorptive uptake results of roxarsone in aqueous solution depend on various factors: pH, buffer system, ionic potential of adsorbate, and pH_{pzc} of adsorbent. The advantage of employing a buffer solution instead of an unbuffered aqueous solution for sorption relates to the ionic strength and constant pH in the case of a buffer. As the concentration of buffer exceeds that of the adsorbate, the activity of the adsorbate approaches unity due to the increased dissolution of the adsorbate by the increased hydronium ion concentration from the buffer resulting in greater dissolution of adsorbate by protolysis.[25] Moreover, controlled speciation of an adsorbate occurs when the pH of the system is maintained. For example, an adsorbate with multiple protonation and oxidation states such as the oxoanions of Se and As (e.g., SeO_3^{2-}, SeO_4^{2-}, AsO_3^{3-}, and AsO_4^{3-}) which may undergo various protolytic equilibria depending on the solution environment during sorption or analysis. In the case of UV-visible absorbance measurements, pH variation occur due to the hydrolysis of CO_2 in air, especially in unbuffered aqueous solution. With increasing ionic strength of the buffer system, electrostatic repulsion between an adsorbent and an adsorbate decrease due to the constriction of the electric double layer of the adsorbent as ionic strength increases. Selection of the buffer is important because an ion with the highest ionic potential in solution will interact first with the adsorbent. Therefore, the ionic potential of the buffer should be lower than that of the adsorbate. The ionic potential (ψ) is the ratio of the adsorbate oxidation state number (z) over the ionic radius (r) of the adsorbate ion ($\psi = z/r$); where r = 0.6 nm (phthalate), 0.6 nm, r = 0.45 nm (selenite), and r = 0.4 nm (phosphate). As the ionic potential of the adsorbate increases, stronger interactions occur between the adsorbate and the adsorbent. Another factor affecting the sorption behaviour is the pH because the net surface charge of the adsorbent is zero when the pH matches the pH_{pzc} of the adsorbent. Thus, the solution pH can be chosen to maximize the electrostatic interaction between adsorbate and adsorbent in solution by accounting for the pK_a of the adsorbate and the pH_{pzc} of the adsorbent. If the pH (solution) < pK_a (adsorbate) and pH_{pzc} (adsorbent), the surface of the adsorbate and the adsorbent are positively charged. The surface of the adsorbent and adsorbate are negatively charged for the opposite case; pH (solution) > pK_a (adsorbate) and pH_{pzc} (adsorbent). At this extreme condition, sorptive uptake will be negligible due to electrostatic repulsion occurs between the adsorbate/adsorbent system. At the following condition: pH_{pzc} (adsorbent) < pH (solution) < pK_a (adsorbate), the surface charge of the adsorbate is positive, the adsorbent is negative, and the maximum sorptive uptake is possible. At the following condition: pK_a (adsorbate) < pH (solution) < pH_{pzc} (adsorbent), the surface charge of the adsorbate is negative, the adsorbent is positive, and maximum sorption uptake is also possible.[26] Roxarsone has three pK_a values in aqueous solution and its speciation against pH is shown in Fig. 4.5.

The pH at the point of zero charge (pH_{pzc}) for magnetite is estimated to be 6.5,[27] while the pK_a values of roxarsone are 3.49, 6.38, and 9.76 and 8.40.[28] The measured pH_{pzc} of GAC (NORIT ROX 0.8) by mass titration is 7.3 and the literature value of pH_{pzc} of goethite is 3.2 for a mineral type and 6.7-9.0 for synthetic form depending on the water content of the product.[27] The use of a buffer at pH 7.00 can produce a net negative surface charge for magnetite, but it may be positive for GAC-iron oxide composites depending on the relative material composition. At pH 7, the ionic charges of roxarsone at this pH condition may be a combination of species; mono-anion (20%) and di-anion (80%), as shown in Fig. 4.5. Therefore, favorable electrostatic interactions are anticipated between magnetite composites, GAC, and goethite with roxarsone at these conditions. H-bonding and van der Waals interactions occur between roxarsone and all adsorbents. By analogy with inorganic arsenate, the roxarsone mono-anion may coordinate in a monodentate-mononuclear fashion with iron species[29] situated in the interstitial void area of the tetrahedral (Fe^{2+} and Fe^{3+}) and octahedral (Fe^{2+}) sites of the magnetite inverse spinel structure[30] to form an inner-sphere complex.[21] Similarly, the roxarsone di-anion may be coordinated as a bidentate-binuclear or a bidentate-mononuclear complex with Fe species. Besides these surface complexes, there may be different configurations of surface bound complexes such as an outer-sphere ion-pair adsorption complex or a solid solution of the roxarsone in the oxide phase.[21] Various types of surface complexes have been reported elsewhere[31] using *Extended X-Ray Absorption* Fine Structure (EXAFS) and Attenuated Total Reflectance Fourier Transform Infrared Spectroscopy (*ATR-FTIR*). The formation of similar surface complexes between magnetite, magnetite composites, NORIT ROX O.8, and goethite with the roxarsone anion are consistent with the foregoing possibilities.

4.3.2 *Sorption Kinetics*

The sorption kinetics and parameters for roxarsone (Q_e, mmol/g) with various sorbent materials are shown in Fig. 4.6 and in Table 4.2. The rate constant, *k* was determined using the pseudo-first-order (PFO) model (equation 3)[32] and the pseudo-second-order (PSO) model (equation 4-3).[33-35] Only goethite showed a higher R^2 value (0.938) for the PSO model, relative to the R^2 value (0.871) for the PFO model. Therefore, the PFO analysis was estimated for all of the adsorbents. The parameter q_t (mg/g) is the adsorbed amount of an adsorbate at time t, q_e (mg/g) is the adsorbed amount of the adsorbate at equilibrium, while k_1 and k_2 are the rate constants (min^{-1}; PFO and $\text{g mg}^{-1}\ \text{min}^{-1}$; PSO). Integration of equations (4-3) and (4-4) at the boundary conditions ($q_t = 0$ at $t = 0$ and $q_t = q_t$ at $t = t$) with rearrangement yields the non-linear PFO equation (4-5) and the non-linear PSO equation (4-6), respectively.

$$\frac{dq_t}{dt} = k_1(q_e - q_t) \tag{4-3}$$

$$\frac{dq_t}{dt} = k_2(q_e - q_t)^2 \tag{4-4}$$

$$q_t = q_e(1 - e^{-k_1 t}) \tag{4-5}$$

$$q_t = \frac{k_2 q_e^2 t}{1 + k_2 q_e t} \tag{4-6}$$

To obtain the rate constant, PFO model was used because root mean square erroe (RMSE) of the PFO model was better than that of PSO model as shown in Table 4.3, with the exception of goethite. Goethite showed better agreement with the PSO model; however, the values of Q_e (mmol/g) were similar for the PFO and PSO models, as shown in Table 4.2 and for providing consistent fitting results, the PFO model was used since it yielde with lower R^2 values.

Figure 4.5. The protolytic speciation expressed as mole fraction against pH in aqueous solution for roxarsone.

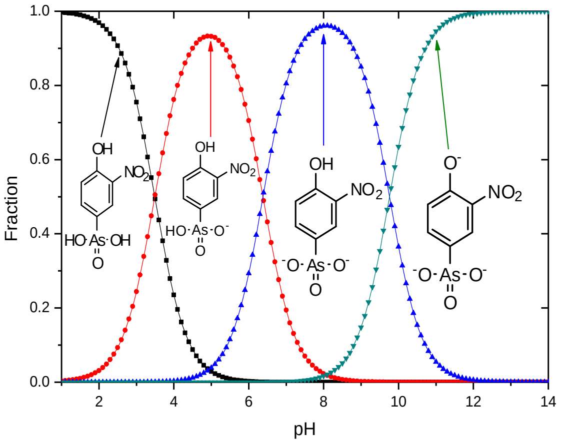

Table 4.2. The kinetic (PFO) sorption parameters for roxarsone (Q_e, mmol/g) with the various sorbent materials (C_o: 0.18 mM, amount of adsorbents: 0.030 g, V= 0.20 L) at 21 °C at pH 7.00 in phosphate buffer for 24 h.

Adsorbents	**q_e** (mmol/g)	***k_{obs}*** (min^{-1})×10^{-3}	**R^2**	**Chi^2/DoF**
Magnetite-P	0.105±0.007	9.86±1.58	0.932	1.20E-04
Magnetite-C	0.081±0.011	4.68±1.86	0.803	2.60E-04
Magnetite 19 %	0.258±0.018	2.18±0.33	0.940	3.60E-04
NORIT ROX 0.8	0.748±0.091	0.580±0.100	0.995	1.10E-04
Goethite	0.244±0.015	41.5±12.3	0.871	1.34E-03
Goethite[1]	0.262±0.013	210.±60.0	0.938	6.50E-04

Note: Magnetite-P is the synthetic material, Magnetite-C is the commercial material.

[1] represents estimate obtained for the PSO model (eqn 3)

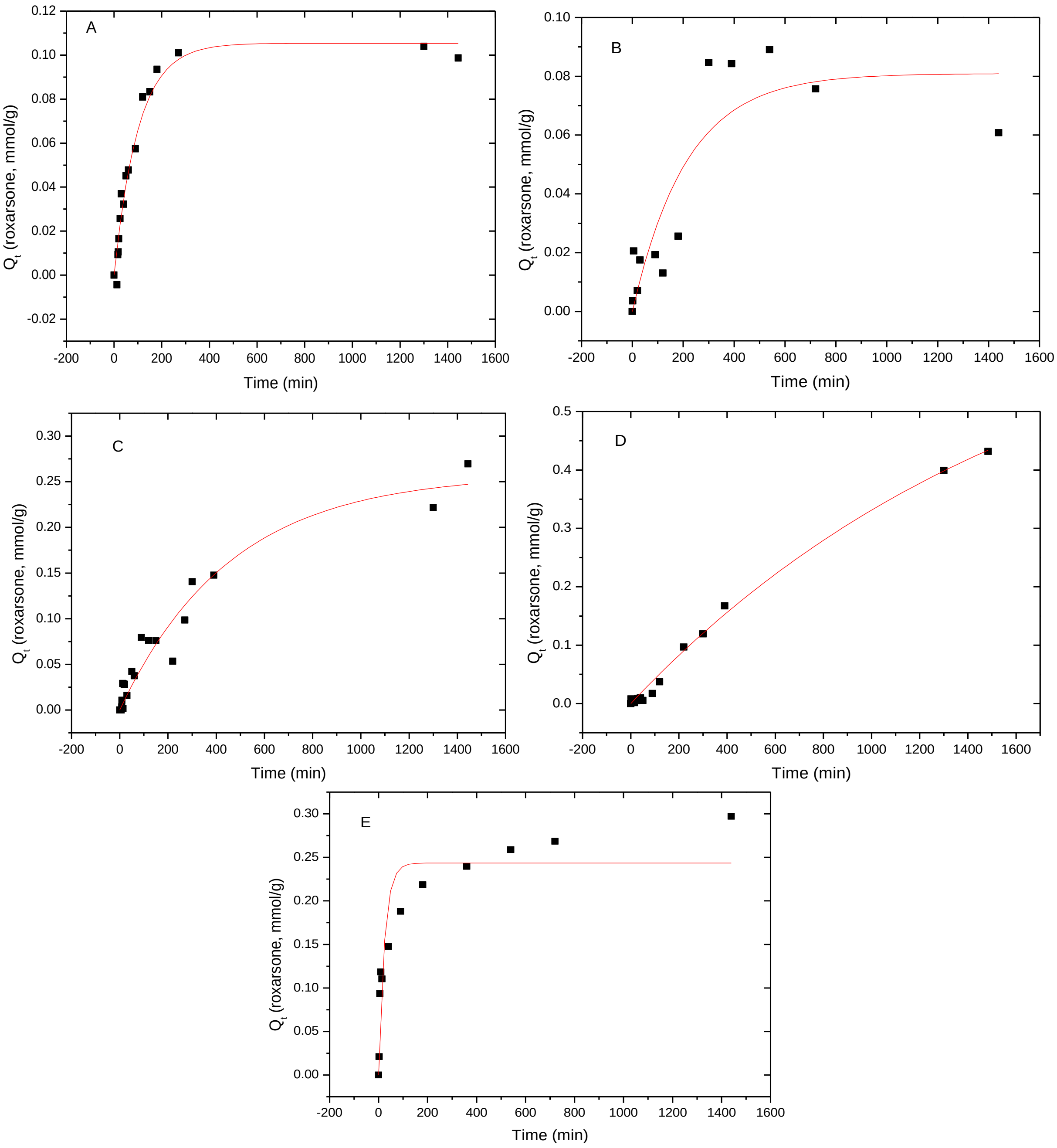

Figure 4.6 The kinetic uptake of roxarsone (Q_t, mmol/g) with various adsorbents (A: magnetite-P, B: magnetite-C, C: magnetite 19 %, D: NORIT ROX 0.8, E: goethite), (C_o: 0.18 mM, amount of adsorbents: 0.030 g, V= 0.20 L) at 21 °C at pH 7.00 phosphate buffer at variable time intervals. Errors (Q_t, ± mmol/g) from *t* = 5 to *t* = 1440 min: Magnetite-P: 0.0114 - 0.0180; Magnetite-C: 0.00109 - 0.00164; Magnetite 19%: 0.0103 - 0.0362; NORIT ROX 0.8:0.0114 - 0.0524; Goethite: 0.0175 - 0.0375

Table 4.3 Comparison of RMSE values of PFO and PSO models for roxarsone adsorption with various adsorbents at 21°C at pH 7.00 phosphate buffer at variable time intervals.

Adsorbents	21 °C	
	PFO	PSO
Magnetite-P	4.76E-03	7.95E-03
Magnetite-C	4.55E-02	4.50E-02
Magnetite 19%	3.97E-01	3.97E-01
NORIT ROX 0.8	9.93E-03	1.01E-02
Goethite	3.50E-02	2.44E-02

As shown in Table 4.2, NORIT ROX 0.8 showed the highest sorptive removal (q_e) of roxarsone in spite of the lowest observed rate constant (k_{obs}). The q_e values for the iron oxide materials and its composites are greater as follows: Magnetite 19% ≈ goethite > Magnetite-P > Magnetite-C. The trends are related to the various intermolecular intereactions between the adsorbate and roxarsone, in addtion to the hydration of each species. GAC has a large graphene surface area (951 m^2/g) and may preferentially adsorb roxarsone due to electron donor-acceptor (EDA, π-π) interactions, H-bonding, and hydrophobic effects. Magnetite 19% has a relatively large surface area (754 m^2/g) and likely adsorbs roxarsone through similar interactions as GAC, as well as inner-sphere surface complexation. The slight attentuation in q_e values may be due to pore blockage of GAC due to iron oxide species and/or the reduced binding affinity of iron oxide sites. Goethite has a reduced surface area (214 m^2/g) relative to Magnetite 19%; however, the presence of hydroxyl groups (Fe-OH) contribute to enhanced binding of roxarsone *via* H-bonding and inner-sphere surface complexation. Magnetite-P (94 m^2/g) and Magnetie-C (41 m^2/g) have reduced surface areas and likely adsorbed roxarsone, similar to that described for Magnetite 19%. The attenuated q_e values may be due to the decrease in surface area and surface reactivity of available Lewis acid species for the commercial magnetite, as described above. The uptake of roxarsone is correlated with the surface area of GAC and its composite materials, and is likely attributed to the favourable interaction of the phenyl ring of the adsorbate with the graphen units of the adsorbent, in accordance with hydrophobic effects. Although the uptake of inorganic arsenate was not measure in this study, it is anticipated that the q_e values correlate with the iron oxide content, according to previous studies reported elsewhere.[12,19] However, the kinetic results in Table 4.2 (k_{obs}) were related to the relative polarity of the adsorbent surface since composites and iron oxide materials display greater values of k_{obs}. The relationship between k_{obs} and hydration phenomena is antcipated due to the polar nature of roxarsone and the relevance of various steps in the adsorptive processes (e.g., film and pore diffusion). The polarity of adsorbents decreased by the order of goethite > magnetite-P > magnetite-C > magnetite 19% > NORIT ROX 0.8. Therefore, goethite could diffuse through the boundary layer fastest and revealed the largest rate constant. As magnetite content decreased, the rate constant also decreased relative to a decreasing polarity of the adsorbent surface. Magnetite-P was more polar than that of Magnetie-C becasue the surface area differed by a factor of two, which probably accomodates more Fe species at the tetrahedral and octahedral sites.

Various adsorbent materials have been used for uptake (mg/g) of arsenic (V) in roxarsone in other independent studies and these results are summarized in Table 4.4.

Table 4.4 Various adsorbents and their sorptive removal of As^{5+} in roxarsone

Adsorbent Material	**Conditions (C_o in [As^{5+}])**	**Uptake (As^{5+}, mg/g)**	**Ref.**
Multi-walled carbon nanotubes (MWCNTs)	pH 2-12; 10 °C; C_o: 50 mL of 5-40 ppm (equilibrium), 10-40 ppm (kinetic); 100 mg adsorbent,	3.65-3.85 (equilibrium) 0.997-2.88 (kinetics)	36
Goethite	pH 5-9; 23 °C; 24 h; C_o: 3.7 ppm; 45 mg adsoebent /L	0.283-0.0883 (kinetics)	37
Magnetite-P	Equilibrium pH 7.0 buffer; 24 h; 21 °C; C_o: 20. mL of 6.56-263 ppm; 15. mg adsorbent Kinetic pH 7.0 buffer; 24 h; 21 °C; C_o: 200. mL of 47.3 ppm; 30. mg adsorbent	37.5 (equilibrium) 8.24 (kinetics)	This study
Magnetite-C		8.39 (equilibrium) 6.07 (kinetics)	
Magnetite 32%		64.6 (equilibrium)	
Magnetite 19%		72.4 (equilibrium) 19.3 (kinetics)	
NORIT ROX 0.8		134. (equilibrium) 56.1 (kinetics)	
Goethite		119. (equilibrium) 18.2 (kinetics)	

In the case of secondary binding between the arsenate anion moiety of roxarsone and the iron oxide sites of the adsorbent, adsorption is thermodynamically favored as a bidentate-binuclear inner-sphere surface complex on the surfaces of magnetite composites[38] and goethite. The monodentate-mononuclear inner-sphere surface complex is regarded as the minor contributor by recalling the anion speciation at the pH conditions employed herein, as illustrated in Fig. 4.5. The adsorption mechanism for the arsenic moiety of roxarsone is proposed in Scheme 4.1, and is anticipated to be more important for inorganic forms of arsenic or its composite materials with increased loading of iron oxide on the graphene surface. In the case of magnetite materials, roxarsone is adsorbed as an outer-sphere surface complex due to the electrostatic repulsion between magnetite and roxarsone. H-bonding may occur between the surface hydroxyl groups of magnetite with the roxarsone anion or coordinating water molecules to offset electrostatic repulsion interactions. In the case of GAC, π-π displaced or T-shaped stacking interactions between the phenyl group of roxarsone and the graphene surface are the dominant interactions (*cf*. Scheme 4.2).[39] Additional H-bonding and inner-sphere surface complexation may occur; however, the pheny ring interactions are considered as the main driving force for the uptake of roxarsone for GAC and its composite materials, in agreement with the hydrophobic effect. Considering the adsorption rate constant values (k_{obs}) in Table 4.2, the bidentate-binuclear inner-sphere surface complex with goethite may occur with a greater degree of ligand exchange; whereas, magnetite composites and GAC may undergo slower ligand exchange through π-π interactions affording greater overall sorptive interactions. Magnetite-P and magnetite-C may be exposed to the slow inner-sphere surface complex formation rate and H-bonding wherein steric effects due to hydration processes attenuate the value of k_{obs}. When the roxarsone anion is adsorbed onto the surface of iron oxide/oxyhydrate, a modified triple-layer model (TLM) may provide an understanding of the secondary importance of such surface complexation processes.[40] In this model, the adsorbed ion may be bound to the α-layer (equivalent to the inner Helmholtz lane), forming an inner-sphere complex, and the β-layer (equivalent to the outer Helmholtz lane), forms an outer-sphere surface complex.[40]

Scheme 4.1. Secondary adsorption of roxarsone onto the surface of an iron oxide/oxyhydrate at pH 7.00 in phosphate buffer (adapted from ref. [12]).

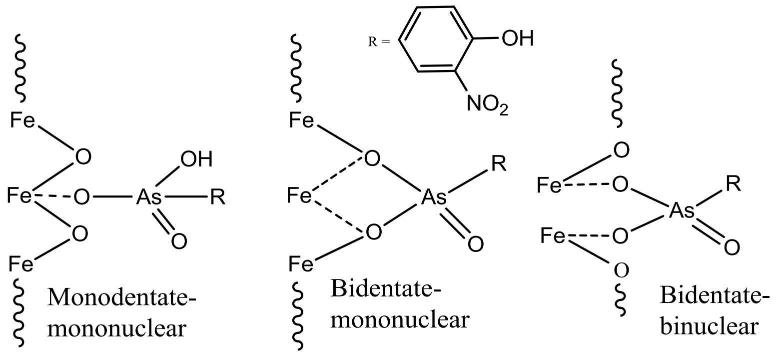

Scheme 4.2. The primary adsorption mechanism of roxarsone onto the graphene surface of NORIT ROX 0.8 *via* a π-π stacking mechanism at pH 7.00 in aqueous phosphate buffer solution (adapted from ref. [39]).

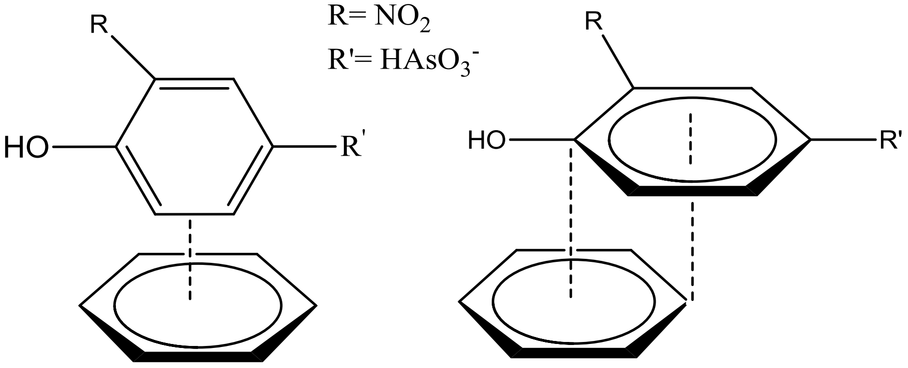

T-shaped or edge-to-face

Displaced or slip stacked

4.4 Experimental Section

4.4.1 *Synthesis and experimental conditions*

Roxarsone was obtained from Haohua Industry Co. Ltd. (Jinan City, China) was purified by recrystallization from water. Briefly, 1 g of roxarsone was dissolved in 25 mL of Millipore water at 65 ºC with stirring and this solution was hot filtered through Whatman No.2 filter paper at ambient conditions. The filtrate solution was allowed to cool slowly before being placed in a refrigerator for 24 h. Aggregates of small orange crystals were collected and isolated through filtration with drying at 50 ºC for 1 h to afford a light tan powder product. Magnetite was prepared by co-precipitation methods, as described elsewhere.[41] Magnetite composites with activated carbon was also prepared by the same method, but the slurry of activated carbon solution (200 mL) containing 1.0 g of activated carbon was prepared before adding Fe^{3+}/Fe^{2+} (2:1 molar ratio). The detailed experimental conditions are given in Table 4.5. Absorbance of the sample solutions were measured with a UV-vis spectrophotometer (Varian Cary 100 SCAN) at $\lambda = 244$ nm with a quartz cuvette. Each adsorbent has a notable magnetic susceptibility except the activated carbon and goethite; thus, kinetic experiments were performed using an aluminum stirring paddle with an overhead mixer with a semi-permeable dialysis tubing (Aldrich, molecular weight cut-off 12,000-14,000 *amu*), as shown in Fig. 4.7. The dialysis tube was cut to a proper size and applied as a cover for an open-ended syringe body with parafilm, as shown in Fig. 4.7.

Table 4.5. The experimental conditions for the uptake studies of roxarsone with various adsorbents at pH 7.00 in phosphate buffer for 24 h.

Sorption	Adsorbents	T (°C)	Amounts (mg)	C_o (mM)	Volume (L)
Equilibrium	Magnetite-P	21	15	0.025-1.0	0.020
	Magnetite-C	21	15	0.025-1.0	0.020
	Magnetite 32 %	21	15	0.025-1.0	0.020
	Magnetite 19 %	21	15	0.025-1.0	0.020
	Magnetite 10 %	21	15	0.025-1.0	0.020
	NORIT ROX 0.8	21	15	0.025-1.0	0.020
	Goethite	21	15	0.025-1.0	0.020
Kinetics	Magnetite-P	21	30	0.18	0.20
	Magnetite-C	21	30	0.18	0.20
	Magnetite 19%	21	30	0.18	0.20
	NORIT ROX 0.8	21	30	0.18	0.20
	Goethite	21	30	0.18	0.20

Figure 4.7. Experimental set-up for *in-situ* kinetic uptake studies

4.4.2 *Equilibrium sorption studies*

A stock solution (1.0 mM) of the purified roxarsone in Millipore water was prepared, which was further diluted to provide working solutions of roxarsone (C_o: 0.026, 0.050, 0.076, 0.10, 0.20, 0.30, 0.50, 0.60, 0.70, 0.80, 0.90, 1.0 mM). 20 mL of the working solution was added into 50 mL centrifuge tubes and shaken rotationally for 24 h at 200 rpm with a SCILOGEX SK-0330-Pro. After reaching equilibrium, the samples were centrifuged with a Beckman Coulter Avanti J-E Centrifuge for 30 min. at 25,000 rpm and 10 mL of the supernatant was carefully transferred to a sample vial for subsequent analysis. UV-Vis was carried out using 1.0 mL of supernatant solution in a quartz cuvette where further dilutions were made using 1.0 mL of 10 mM KH_2PO_4 buffer (pH = 7.00±0.02). The diluted solution was discarded, and prepared twice more to rinse the cuvette, before a final absorbance measurement was recorded.

4.4.3 *Kinetic sorption studies*

200 mL of 0.18 mM roxarsone was added into a 250 mL beaker. The syringe wrapped with the dialysis tubing was introduced in the solution and soaked for 20 min for equilibrium of the solution containing dialysis tubing. After pre-soaking the dialysis tubing, an aliquot (0.30 mL) was sampled at $t = 0$. And 0.030 g of each adsorbent was added into the beaker while the solution was stirring at 510±10 rpm. Aliquots of 0.30 mL were taken at the scheduled time t and absorbance was measured at 244 nm. The aliquots were diluted with 2.70 mL of 10 mM KH_2PO_4 buffer (pH 7.00±0.02).

4. 5 Conclusions

The equilibrium and kinetic uptake studies for various adsorbents were obtained and the results reveal that NORIT ROX 0.8 provided the most favorable overall adsorption, followed by goethite, magnetite 10 %, magnetite 19 %, magnetite 32 %, magnetite-P, and magnetite-C. This result showed that the high surface area activated carbon enable efficient removal of roxarsone *via* favourable π-π interactions between the roxarsone phenyl moiety and the graphene surface (*cf*. Scheme 4.2). The decreasing sorptive uptake parallels a decrease in the content of GAC for the composite materials. Thus, the Lewis acid-base interactions of the arsenate anion with the iron oxide surface sites are considered secondary in nature for roxarsone relative to those in Scheme 2. However, the sorptive removal of roxarsone with goethite was pronounced because of its polar nature due to the surface hydroxyl groups of this mineral surface and the propensity for H-bonding interactions. Secondary surface complexes between the roxarsone anion and the iron oxide/oxyhydrate surface sites may adopt one or more mechanisms: inner-sphere of monodentate-mononuclear, bidentate-mononuclear, and bidentate-binuclear complexes. The secondary interactions (*cf*. Scheme 4.1) described above are anticipated to be more important for inorganic forms of arsenate. The details of these surface adsorption processes is the subject of future studies.

4.6 Acknowledgments

The authors acknowledge the University of Saskatchewan for supporting this research and NORIT America Inc. for the provision of research samples of activated carbon.

4.7 Conflict of Interest

The authors declare no conflict of interest.

4.8 References and Notes

1. Welch, A. H.; Lico, M. S.; Hughes, J. L. Arsenic in groundwater of the Western United States. *Ground Water*, **1988**, *26*, 333-347.
2. Cullen, W. R.; Reimer, K. J. Arsenic Speciation in the Environment. *Chem. Rev.* **1989**, *89*, 713-764.
3. Tallman, D. E.; Shaikh, A. U. Redox stability of inorganic arsenic(III) and arsenic(V) in aqueous solution. *Anal. Chem.*, **1980**, *52*, 196-199.
4. Katsoyiannis, I. A.; Zouboulis, A. I. Application of biological processes for the removal arsenic from groundwaters. *Water Res.*, **2004**, *38*, 17-26.
5. Jackson, B. P.; Seaman, J. C.; Bertsch, P. M., Fate of arsenic compounds in poultry litter upon land application. *Chemosphere*, **2006**, *65*, 2028-2034.
6. Makris, K. C.; Salazar, J.; Quazi, S.; Andra, S. S; Sarkar, D.; Bach, S. B. H.; Datta, R., Controlling the fate of roxarsone and inorganic arsenic in poultry litter. *J. Environ. Qual.*, **2008**, *37*, 963-971.
7. Arai, Y.; Lanzirotti, A.; Sutton, S.; Davis, J. A.; Sparks, D. L., Arsenic speciation and reactivity in poultry litter. *Environ. Sci. Technol.*, **2003**, *37*, 4083-4090.
8. Church, C. D.; Kleinman, P. J. A.; Bryant, R. B.; Saporito, L. S.; Allen, A. L., Occurrence of arsenic and phosphorus in ditch flow from litter-amended soils and barn areas. *J. Environ. Qual.*, **2010**, *39*, 2080-2088.
9. Makris, K. C.; Quazi, M.; Punamiya, P.; Sarkar, D.; Datta, R., Fate of arsenic in swine waste from concentrated animal feeding operations. *J. Environ. Qual.*, **2008**, 37, 1626-1633.
10. Stolz, J. F.; Perera, E.; Kilonzo, B.; Kail, B.; Crable, B.; Fisher, E.; Ranganathan, M.; Wormer, L.; Basu, P., Biotransformation of 3-nitro-4-hydroxybenzene arsenic acid (roxarsone) and release of inorganic arsenic by clostridium species. *Environ. Sci. Technol.*, **2007**, *41*, 818-823.
11. Viet, H. P.; Con, H. T.; Ha, T. C.; Ha, V. H.; Berg, M.; Giger, W.; Schertenleib, R. Investigation of arsenic removal technologies for drinking water in Vietnam. In *Arsenic Exposure and Health Effects V.*; Chappell, W. R., Abernathy, C. O., Calderon, R. L., Thomas, D. J., Eds.; Elsevier B.V.: Amsterdam, the Netherlands , 2003; pp. 459-469.

12. Gallegos-Garcia, M.; Ramírez-Muñiz, K.; Song, S. Arsenic removal from water by adsorption using iron oxide minerals as adsorbents: A Review. *Miner. Process. Extr. M.*, **2012**, *33*, 301-315.
13. http://www.gazette.gc.ca/rp-pr/p2/2012/2012-03-14/html/sor-dors22-eng.html (accessed 14/09/13)
14. Shaw, S.A., Hendry, M.J., Essilfie-Dughan, J., Kotzer, T., Wallschlager, D. Distribution, characterization, and geochemical controls of elements of concern in uranium mine tailings, Key Lake, Saskatchewan, Canada, *Appl. Geochem.,* **2011**, 26, 2044–2056.
15. Kwon, J. H.; Wilson, L. D. Surface modified activated carbon with β-cyclodextrin - Part I. Synthesis and characterization. *J. Environ. Sci. Health., Part A,* **2010,** *45*, 1775-1792.
16. Do, M. H.; Phan, N. H.; Nguyen, T. D.; Pham, T. T. S.; Nguyen, V. K.; Vu, T. T. T.; Nguyen, T. K. P. Activated carbon/Fe_3O_4 nanoparticle composite: Fabrication, methyl orange removal and regeneration by hydrogen peroxide. *Chemosphere,* **2011**, *85*, 1269-1276.
17. Pratt, D. Y.; Wilson, L. D**.**; Kozinski, J. A. Preparation and sorption studies of glutaraldehyde cross-linked chitosan copolymers. *J. Colloid Interface Sci*. **2013**, *395*, 205-211.
18. Wilson, L. D.; Pratt, D. Y.; Kozinski, J. A. Preparation and Sorption Studies of β-Cyclodextrin-Chitosan-Glutaraldehyde Terpolymers. *J. Colloid Interface Sci*. **2013**, *393*, 271-277.
19. a) Vaclavikova, M.; Gallios, G. P.; Hredzak, S.; Jakabsky, S. Removal of arsenic from water streams: an overview of available techniques. *Clean. Techn. Environ. Policy,* **2008**, *10*, 89-95, b) Liu, M.; Chen, C.; Hu, J.; Wu, X.; Wang, X. Synthesis of magnetite/graphene oxide composite and application for cobalt(II) removal. *J. Phys. Chem. C.*, **2011**, *115*, 25234-25240, and c) Salah El-Din, T. A.; Elzatahry, A. A.; Aldhayan, D. M.; Al-Enizi, A. M.; Al-Deyab, S. S. Synthesis and characterization of magnetite zeolite nano composite. *Int. J. Electrochem. Sci.,* **2011**, *6*, 6177-6183.
20. Bayse, G. S.; Jinadu, L . A.; Shaw, K . L.; Wiley, K. L. The *N*-acetylation of arsanilic acid in vitro by mammalian enzymes. *Drug. Metab. Dispos*., **2000**, *28*, 487-492.
21. Hayes, K.F., Roe, A.L., Brown, Jr. G.E., Hodgson, K.O., Lecknie, J.O., Parks, G.A., In situ X-ray absorption study of surface complexes: selenium oxyanions on α-FeOOH. *Science,* **1987**, *238*, 783-786.

22. Stumm, W. Chemistry of the solid-water interface: processes at the mineral-water and particle-water interface in natural systems. John Wiley & Sons: New York, USA, 1992; pp. 21-22.

23. Sips, R. On the structure of a catalyst surface. *J. Chem. Phys.* **1948**, *16*, 490-495.

24. Ruthven, D. M. Principles of adsorption and adsorption processes; John Wiley and Sons: New York, 1984; p 43

25. Hingston, F. J.; Atkinson, R. J.; Posner, A. M.; Quirk, J. P. Specific adsorption of anion on goethite. *Trans. 9th Int. Congr. Soil. Sci*. **1968**, *1*, 669-678.

26. Guo, R.; Wilson, L. D. Synthetically engineered chitosan-based materials and their sorption properties with methylene blue in aqueous solution. *J. Colloid Interface Sci*., **2012,** *388*, 225-234.

27. Parks, G. The isoelectric points of solid oxides, solid hydroxides, and aqueous hydroxo complex systems. *Chem. Rev*., **1965**, *65*, 177-198.

28. Baert, B.; Langendries, S.; Bodé, S.; Cornez, B.; Poppe, L.; Slegers, G.; De Spiegeleer, B. Drug Analysis 2006: Programme and Abstract Book, The Belgian Society of Pharmaceutical Sciences: Brussels, Belgium, 2006; p. 200.

29. Chan, Y. T.; Kuan, W. H.; Chen, T. Y.; Wang, M. K. Adsorption mechanism of selenate and selenite on the binary oxide systems. *Water Res.*, **2009**, *43*, 4412-4420.

30. Bastow, T. J.; Trinchi, A. NMR analysis of ferromagnets: Fe oxides. *Solid State Nucl. Mag.*, **2009**, *35*, 25-31.

31. a) Wincott, P. L.; Vaughan, D. J. Spectroscopic studies of sulfides. *Rev. Mineral. Geochem*., **2006**, *61*, 181-229, and b) Tejedor-Tejedor, M. I.; Anderson, M. A. Protonation of phosphate on the surface of goethite as studied by CIR-FTIR and electrophoretic mobility. *Langmuir*, **1990**, *6*, 602-611.

32. Lagergren, S. About the theory of so-called adsorption of soluble substances. *Kungliga Svenska Vetenskapsakademiens Handlingar*, **1898**, *24*, 1-39.

33. Blanchard, G.; Maunaye, M.; Martin, G. Removal of heavy metals from waters by means of natural zeolites. *Water Res.*, **1984**, *18*, 1501-1507.

34. Ho, Y. S. Adsorption of heavy metals from waste streams by peat. Dissertation for the Doctoral Degree, University of Birmingham, Birmingham, 1995.

35. Azizian, S. Kinetic models of sorption: A theoretical analysis. *J. Colloid Interface Sci*., **2004**, *276*, 47-52.
36. Hu, J.; Tong, Z.; Hu, Z.; Chen, G. W.; Chen, T. H. Adsorption of roxarsone from aqueous solution by multi-walled carbon nanotubes. *J. Colloid Interface. Sci*., 2012, *377,* 355-361.
37. Chen, W. U; Huang, C. H. Surface adsorption of organoarsenic roxarsone and arsanilic acid on iron and aluminum oxides. *J. Hazard. Mater.*, **2012**, *227- 228,* 378- 385.
38. Sherman, D. M.; Randall, S. R. Surface complexation of arsenic(V) to iron(III) (hydr)oxides: Structural mechanism from *ab initio* molecular geometries and EXAFS spectroscopy. *Geochim. Cosmochim. Ac.*, **2003**, *67*, 4223-4230.
39. Kwon, J. H.; Wilson, L. D. Surface modified activated carbon with β-cyclodextrin - Part II.Adsorption properties. *J. Environ. Sci. Health., Part A*, **2010,** *45*, 1793-1803.
40. Zhang, P.; Sparks, D. L. Kinetics of Selenate and Selenite Adsorption/Desorption at the Goethite/Water Interface. *Environ. Sci. Technol.* **1990**, *24,* 1848-1856.
41. Berger, P.; Adelman, N. B.; Beckman, K. J.; Campbell, D. J.; Lisensky, G. C.; Ellis, A. B. Preparation and Properties of an Aqueous Ferrofluid. *J. Chem. Ed*., **1999**, *76,* 943-948.

CHAPTER 5 CONCLUSIONS AND FUTURE WORK

5.1 Conclusions

The objectives of this research were to prepare magnetite composites using activated carbon and to evaluate their sorptive uptake properties of inorganic and aryl anion species containing either Se or As in aqueous solution. The syntheses of magnetite and of goethite were achieved by Fe^{3+}/Fe^{2+} coprecipitation and by employing a high OH^{-}/Fe^{3+} molar ratio (5/1), respectively. The synthesis of magnetite composites was achieved by adding Fe^{3+}/Fe^{2+} species into the activated carbon slurry based on *w* (magnetite) / *w* (activated carbon) content. The characterization of magnetite, magnetite composites, and goethite were achieved by confirming their diagnostic bands of IR (magnetite: 570 cm^{-1} (v_1) for the Fe^{3+}-O stretching mode of the tetrahedral and octahedral sites and 390 cm^{-1} (v_2) for the Fe^{2+}-O stretching mode of the octahedral sites; goethite: 793 cm^{-1} -OH deformation (γ-OH) and 887 cm^{-1} -OH deformation (δ-OH)), Raman (magnetite: 689 cm^{-1} Fe-O symmetric stretching, A_{1g}; goethite: 301 cm^{-1} Fe-O-Fe symmetric stretching and 396 cm^{-1} Fe-OH symmetric stretching), and PXRD ((311) plane at $2\theta = 35.46°$ for magnetite). The surface areas (m^2/g) of magnetite_P, magnetite 32%, magnetite 19%, magnetite 10%, and NPRIT ROX 0.8 were 93.5, 617, 754, 851, and 951, respectively.

Moreover, magnetite composites provided monolayer soprtions of selenium species in solution and two important properties of adsorbents: surface area and surface reactivity. As seen in the Chapter 2, surface area of magnetite composites was adjustable by changing the content of magnetite in activated carbon. By the same reason, surface reactivity was also tunable for removing selenium as seen in Chapter 3 because adsorption evaluation of selenium in the solution at pH 5.26 disclosed that the following trend in sorption parameters was observed with the various types of sorbent materials:

Q_m (Se, μmol/g): Goethite (18.3) > magnetite-C (1.52) > magnetite-P (1.13) > magnetite 19% (0.200)

Q_e (Se, mg/g): Goethite (0.139-0.216) > Magnetite_P (0.0509-0.0556) > Magnetite_C (0.0426-0.0483) > Magnetite 19 % (0.0192-0.0409) > NORIT ROX 0.8 (0.00913-0.0107)

k_{obs} (min^{-1}): Goethite (0.0266-0.0350) > Magnetite_P (0.0217-0.0256) > Magnetite_C (0.0110-0.0199) > Magnetite 19 % (0.00529-0.0178) > NORIT ROX 0.8 (0.00149-0.0530)

E_a (kJ/mol): Magnetite_P(-6.96 ~ -7.16) < Goethite (8.28-8.48) < Magnetite_C (31.2-31.3) < Magnetite 19 % (34.9-35.1) < NORIT ROX 0.8 (101)

$\Delta H^{‡}$ (kJ/mol): Magnetite_P (-9.47) < Goethite (5.89) < Magnetite_C (28.8) < Magnetite 19 % (32.6) < NORIT ROX 0.8 (98.5)

As the surface of the adsorbents had more iron species, hydroxyls groups, and was more polar, **Q_e** and **k_{obs}** increased because more surface complexation, H-bonding, and rapid diffusion occurred. However, **E_a** and **$\Delta H^{‡}$** showed the opposite trend due to the increased activation barriers and the presence of the multiple activated complexes in the sorption.

Magnetite composites, NORIT ROX 0.8, and goethite showed monolayer sorption of arsenic species in solution. Surface reactivity for the removal of arsenic species was tunable as seen in Chapter 4. The following trend of relative uptake (roxarsone, mg/g) for each sorbent material was observed with the various types of sorbent materials at pH 7.00 in aqueous phosphate buffer:

Q_m: NOROT ROX 0.8 (471 mg/g) > goethite (418 mg/g) > magnetite 19% (254 mg/g) > magnetite 32 % (227 mg/g) > magnetite-P (132 mg/g) > magnetite-C (29.5 mg/g)

The high surface area with oleophilicity of NORIT ROX 0.8, surface hydroxyls groups of goethite, and the contents of iron species in the magnetite composites and in goethite made this trend by forming surface complexes and H-bonding on the surface of adsorbents .

The utility of magnetite and activated carbon were excellent adsorbents due to the formation of surface complexes and their relatively high surface area. According to these results, magnetite composites favored inorganic forms of selenium and arsenic and NORIT ROX 0.8 favored adsorption of aryl forms of arsenic in solution sorption. In case of goethite, its removal properties were not affected by the chemical structures of selenium and arsenic because it had iron (III) species and surface hydroxyl groups that bound effectively selenium and arsenic species via surface complexes and the occurrence of H-bonding interactions.

Many researchers have published synthesis of magnetite and its composites using various methods and their applications for removing water purification. However, there are few reported studies of magnetite composites with activated carbon. However, this research was the first reported example for the preparation of a magnetite composite with the activated carbon using Fe(II)/Fe(III) co-precipitation in the basic aqueous media without the need of a subsequent heating-annealing process. The occurrence of Fe leaching in such types of composite magnetite materials has not been previously shown. A comparison of the adsorptive uptake (Se^{4+}, mg/g and As^{5+}, mg/g) was based on a normalization procedure that accounts for the initial concentration of selenium and roxarsone by various adsorbent materials, as shown in Table 5.1. In Table 5.1, the prepared magnetite and its composites showed excellent adsorptive properties relative to previous studies for a wide range of adsorbent materials.

Table 5.1 A comparison of uptake (Se^{4+}, mg/g and As^{5+}, mg/g) by various adsorbents based on this work and literature studies by normalizing the initial concentration of selenium and roxarsone

Adsorbents	Uptake (E) (Se^{4+}, mg/g)	Uptake (K) (Se^{4+}, mg/g)	Ref.	Uptake (E) (As^{5+}, mg/g)	Uptake (K) (As^{5+}, mg/g)	Ref.
Goethite		2.90	1		0.283-0.0883	2
MWCNT				3.65-3.85	0.997-2.88	4
Magnetite	0.220		3			
Fe_3O_4 nano-materials	2.38		5			
Magnetite-P	41.9-80.5	1.00		5.70	1.74-6.97	
Magnetite-C		0.869		1.28	1.28-5.14	
Magnetite 19%	0.712	0.736		11.0	4.07-16.3	
Magnetite 32%				9.83		
NORIT ROX 0.8		0.214		20.4	119-47.4	
Goethite		11.7			1.42	

Note) **E** means sorption equilibrium experiment and **K** means sorption kinetic test.

This study showed the prepared magnetite composites are excellent adsorbents for removing aryl and inorganic forms of Se and As chemical species in aqueous solution. The composite nature of the composite adsorbents suggests their potential as dual function sorbents due to their affinity toward aryl and inorganic anion species. In addition to the aforementioned tunable surface reactivity and surface area, magnetite composites have sufficient magnetic susceptibility so that separation of adsorbents in water treatment processes may be achieved using an electro-magnet.

The prepared magnetite composites may serve as a multi-purpose adsorbent for inorganic and organic adsorbates. As shown in Fig. 5.1, inorganic selenium species circled in yellow and aryl arsenic species circled in red may be bound onto the magnetite composite adsorbent (white material for magnetite and grey porous sheet for activated carbon) *via* surface complexation through π-π stacking and H-bonding. An oxygen atom in inorganic selenium species (Lewis base) can donate its lone pair electrons to an iron atom on the surface of a magnetite composite (Lewis acid, the whitish material) and the aromatic ring of aryl arsenic species is π-electron deficient, depending on the mode of stacking, which enable π-π stacking onto the graphene surface of the magnetite composite. Based on these experimental evaluations, the goethite/AC composite is proposed as a good multi-purpose adsorbent with favorable among the materials studied herein. The removal of oxyanions of selenium and an organo-arsenical at the same time in aqueous solution is feasible due to the high surface area of activated carbon and surface hydroxyl groups and Lewis acid Fe (III) species in goethite. The adsorptive removal of selenite was 100%, 87%, 70%, 65%, 42%, and 7% by goethite, magnetite, magnetite 32%, magnetite 19%, magnetite 10%, and NORIT ROX 0.8, respectively. The adsorptive removal of roxarsone was 36%, 27%, 23%, 8%, and 5% by NORIT ROX 0.8, goethite, magnetite 19%, magnetite-prepared, and magnetite-commercial, respectively.

Figure 5.1 Diagram of inorganic selenium species and aryl arsenic species bound onto the magnetite composite in solution.

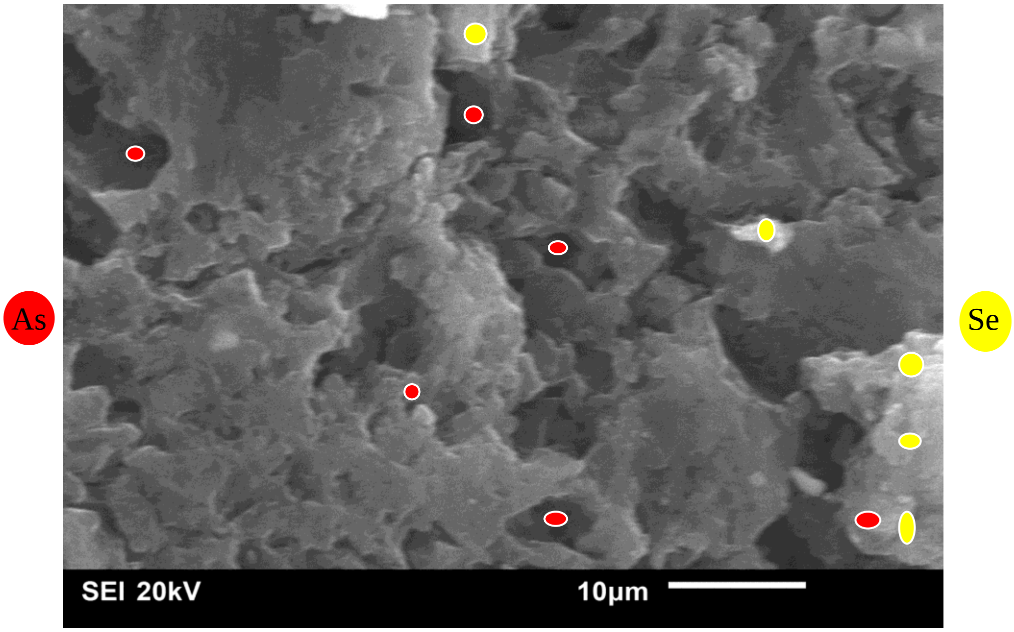

5.2 Future Work

The discussion regarding the surface complexes of the surface of magnetite composites and goethite was based on various intermolecular interactions occurring between the adsorbents and the adsorbates. Although iron oxides and activated carbon were previously studied, there are knowledge gaps concerning the nature of the surface reaction sites and bond lengths between atoms in the surface complexes. To address these knowledge gaps, a more advanced sorption model is required such as Charge Distribution (CD) - MUlti SIte Complexation (MUSIC).

The classical Gouy-Chapman treatment of the diffuse double layer and the modified triple layer are examples of adsorption models that describe a reaction between a homogeneous single surface site and an adsorbate with a point charge. For example, the net charge of PO_4^{3-} is the result of the polyatomic ion distributed over five atomic sites. However, the Charge Distribution (CD) model uses a formal valence bond (*v*) to distribute the net charge of the metal ion over the surrounding bonds. Pauling defined that the formal bond valence (*v*) is the product of the charge (*z*) of a cation divided by its coordination number (*CN*), $v = \frac{z}{CN}$.[6] For example, Fe^{+3} ions (*z* = +3) in the crystal structure of goethite are coordinated to six O(H) ligands and the individual formal valence bond (*v*) per one ligand, considering the symmetric distribution of charge over the surrounding bonds, is $v = \frac{1}{2}$.

In addition, even for relatively simple oxide minerals, many types of surface hydroxyl groups may be present on a single plane of the mineral and their reactivities are likely to differ. Therefore, MUlti SIte Complexation (MUSIC) model considers the surface of the adsorbent as heterogeneous according to the various surface hydroxyl groups.[7,8] Moreover, the degree of protonation and the presence of metal ions, results in variable surface charges. The CD model extended this MUSIC concept by distributing surface charges over the surrounding bonds.

Experimental results to further support the estimates of the CD-MUSIC[9] model may require X-ray Absorption Spectroscopy (XAS; Extended X-ray Absorption Fine Structure (EXAFS) and X-ray Absorption Near Edge Structure (XANES)).[10,11] The spectroscopic results from these studies can provide detailed structural information to support the surface adsorption mechanism.. The combination of the modified triple layer and surface complexation model may also provide a clear picture of the reactive site with molecular structural information at various adsorbent surfaces. Structural information such as vibrational bands to infer various types of intermolecular interactions and spectroscopic signatures to evaluate composition or the location of surface *vs*. pore bound iron oxide sites will complement existing adsorption parameters (Q_m, k, Q_e, and K_{eq}). In addition, this structural information may provide insight regarding the adsorption mechanism process with parameters such as the bond length, surface activity of the adsorbed inner-sphere surface complex in terms of the surface coverage (θ) rather than concentration (mol/L and mol/m^2), and the nature of the surface reaction site. For example, one may recognize there are different types of bidentate inner-sphere complexes based on EXAFS and XANES data to evaluate the reaction sites at the edges, corners, or the surface of the adsorbent. Therefore, application of the CD-MUSIC model with EXAFS and XANES outcomes can identify the active adsorption site(s).[9] Thus, future work on this research area requires broad and multidisciplinary methodologies such as spectroscopy, surface composition, and potential profile and will provide an informative understanding of the relationship between molecular structural binding site and the relationship with kinetic and equilibrium adsorption parameters of adsorbate/ adsorbent systems through systematic adsorption studies.

Another proposed area of future work involves modifying activated carbon would involve acid treated activated carbon with nitric acid because this type of surface modification can provide surface carbonyl, hydroxyl, carboxylic, and lactone groups that can improve H-bonding for increasing sorptive removal and the formation of modified iron oxide composite materials.

5.3 References

1. Mitchell, K.; Couture, R. M.; Johnson, T. M.; Mason, P. R. D.; Van Cappellen. P. Selenium sorption and isotope fractionation: Iron(III) oxides versus iron(II) sulfides. *Chem. Geol.*, **2013**, *342*, 21-28.

2. Chen, W. U; Huang, C. H. Surface adsorption of organoarsenic roxarsone and arsanilic acid on iron and aluminum oxides. *J. Hazard. Mater.*, **2012**, *227- 228*, 378- 385.

3. Martinez, M.; Gimenez, J.; de Pablo, J.; Rovira, M.; Duro, L. Sorption of selenium(IV) and selenium (VI) onto magnetite, *Appl. Surf. Sci.*, **2006**, *252*, 3767-3773.

4. Hu, J.; Tong, Z.; Hu, Z.; Chen, G. W.; Chen, T. H. Adsorption of roxarsone from aqueous solution by multi-walled carbon nanotubes. *J. Colloid Interface. Sci*., 2012, *377*, 355-361.

5. Sharrad, M. O. M.; Liu, H.; Fan, M. Evaluation of FeOOH performance on selenium reduction, *Sep. Purif. Technol.*, **2012**, *84*, 29-34.

6. Pauling, L. The principles determining the structure of complex ionic crystals. *J. Am. Chem. Soc.*, **1929**, *51*, 1010-1026. (1929) .

7. Hiemstra, T.; Van Riemsdjk, W. H.; Bolt, G. H. Multisite proton adsorption modeling at the solid/solution interface of (hydr)oxides: A new approach. I. Model description and evaluation of intrinsic reaction constants. *J. Colloid Interface Sci.*, **1989**, *133*, 91-104.

8. Hiemstra, T.; De Wit, J. C. M.; Van Riemsdijk, W. H. Multisite proton adsorption modeling at the solid/solution interface of (hydr)oxides: A new approach: II. Application to various important (hydr)oxides. *J. Colloid Interface Sci.*, **1989**, *133*, 105-117.

9. Hiemstra, T.; Van Riemsduk, W. H. A surface structural approach to ion adsorption: The charge distribution (CD) model. *J. Colloid Interface Sci.*, **1996**, *179*, 488-508.

10. Peak, D.; Saha, U. K. ; Huang, P. M. Selenite adsorption mechanisms on pure and coated montmorillonite: An EXAFS and XANES spectroscopic study. *Soil Sci. Soc. Am. J.*, **2006**, *70*, 192-203.

11. Arai, Y.; Elzinga, E. J.; Sparks. D. L. X-ray absorption spectroscopic investigation of arsenite and arsenate adsorption at the aluminum oxide-water interface. *J. Colloid Interface Sci.*, **2001**, *235*, 80-88.

APPENDICES

A1. Kinetic Set-up and *in-situ* filtration device for selenium adsorption studies

The *in-situ* filtration device as shown in Fig. A-1 for kinetic sampling was important in that the aliquot should be free of any adsorbate for the measurement with Hydride generation Atomic Absorption Spectroscopy (HG-AAS). Therefore, this *in-situ* filtration device was developed considering for providing the constant stirring rate, height of solution relative to the filter body, and the distance from the overhead stirrer.

- Materials
  - ✓ A syringe, an aluminum stirring, and a filter paper (Whatman filter paper #42)

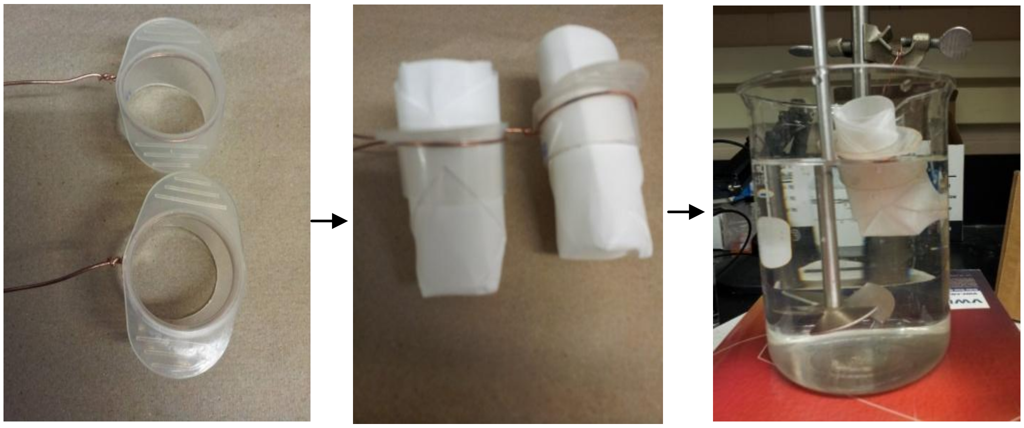

Figure A-1 The process to make the *in-situ* filtration device for selenium kinetic sampling

A2. Kinetic Set-up and in-situ filtration device for roxarsone adsorption studies

The *in-situ* filtration device as shown in Fig. A-2 for kinetic sampling was important in that the aliquot should be free of any adsorbate for the measurement with UV-Vis spectroscopy. Therefore, this *in-situ* filtration device was developed considering for providing the constant stirring rate, height of solution relative to the filter body, and the distance from the overhead stirrer.

- Materials
  - ✓ A syringe, an aluminum stirring paddle, and a dialysis tubing (Aldrich, molecular weight cut-off 12,000-14,000 amu)

Figure A-2 The *in-situ* filtration device for roxarsone kinetic sampling

A3. Standard Operation Procedure (SOP) for Hydride Generation Atomic Absorption Spectroscopy (HGAAS) to determine selenium

- Solutions for Hydride System
    - ✓ 10 ppm Se stock solution: 0.5 mL 1000 ppm Se Stock + 49.5 mL 10% HCl solution (Can be stored up to 4 months)
    - ✓ Dilution Solution (10 % HCl): 100 mL conc. HCl + 900 mL Millipore water
    - ✓ Reducing Agent: 1.5 g NaOH and 5.0 g Sodium Borohydride ($NaBH_4$) made up to 1 liter of solution with Millipore water
    - ✓ 200 ppb Se Stock Solution: 1 ml 10 ppm Se stock + 49 ml 10 % HCl solution (Make new stock for every analysis)
- Standards for Selenium Analysis

Standard Final Concentration (ppb)	200 ppb Se Stock Solution (mL)	Dilution Solution (10 % HCl, mL)	Total Final Vol. (mL)
0.00	0.00	400.	400.
2.00	1.00	99.0	100.
5.00	2.50	97.5	100.
10.0	5.00	95.0	100.
20.0	10.0	90.0	100.

- All samples were diluted 5× with the 10% HCl solution before analysis.
- Instrumental conditions
  - ✓ Se: 6mA, slit 1.2 nm @196 nm
  - ✓ Ar injection flow: 6L/h
  - ✓ Temperature: 960 °C electric furnace
  - ✓ Detection limit (ppb): 0.2 Area
  - ✓ Characteristic Concentration (ppb/1% Abs): 0.03 Area
  - ✓ HCl & $NaBH_4$ injection flow: 3.25 mL/min
  - ✓ Sample injection flow: 9 mL/min
- Hydride generation and atomization

$$NaBH_4 + 3H_2O + HCl \longrightarrow H_3BO_3 + NaCl + 8H\cdot \xrightarrow{Se^{4+}} SeH_2 \xrightarrow{960\text{ deg C}} Se^0 + H_2\text{ (excess)}$$